UNIVERSITY OF Southampton

University of Southampton Research Repository
ePrints Soton

Copyright © and Moral Rights for this thesis are retained by the author and/or other copyright owners. A copy can be downloaded for personal non-commercial research or study, without prior permission or charge. This thesis cannot be reproduced or quoted extensively from without first obtaining permission in writing from the copyright holder/s. The content must not be changed in any way or sold commercially in any format or medium without the formal permission of the copyright holders.

When referring to this work, full bibliographic details including the author, title, awarding institution and date of the thesis must be given e.g.

AUTHOR (year of submission) "Full thesis title", University of Southampton, name of the University School or Department, PhD Thesis, pagination

http://eprints.soton.ac.uk

University of Southampton

Faculty of Engineering and the Environment

Tidal Stream Turbines and Sediment Dynamics: The Effects of Array Installation upon the Morphology of a Headland Associated Linear Sandbank

by

Stephen Geoffrey Haynes

Thesis submitted for the degree of Master of Philosophy

September 2015

UNIVERSITY OF SOUTHAMPTON

ABSTRACT

FACULTY OF ENGINEERING AND THE ENVIRONMENT

Master of Philosophy

TIDAL STREAM TURBINES AND SEDIMENT DYNAMICS: THE EFFECTS OF ARRAY INSTALLATION UPON THE MORPHOLOGY OF A HEADLAND ASSOCIATED LINEAR SANDBANK

by Stephen Geoffrey Haynes

Tidal stream generators extract kinetic energy from tidal flows and convert it to electricity. Such hydrodynamic impacts could have implications for sediment movement and the larger-scale morphology of a site. This study investigates the likely relative impacts of multiple large-scale extraction-scenarios upon a real-world submarine sandbank, the Alderney South Banks.

The first phase of the study is an analysis of the South Banks, rooted in the literature of sandbank morphology, and performed using high-resolution bathymetry and sedimentary data. Cross-sections of large migrating sandwaves superimposed upon the sandbank were interpreted to generate a map of the sediment transport pathways. Unusually large sandwave migration rates of up to 70m across a 50 day period were observed in one part of the Bank.

The second, larger phase of the study involved the development of a 2-D numerical model to simulate the tidal flows in the vicinity of Alderney and across the wider English Channel. The model was elevation-forced using nine tidal constituents at its open boundaries and validated against tidal level and tidal-stream velocity data obtained from port tide-gauges and ADCP deployments. An existing, area-averaged roughness method for parameterising the effects of energy extraction for tidal arrays was incorporated into the model. A numerical sediment model was setup to be coupled and run in parallel with the hydrodynamic computation.

An identical 300MW tidal array parameterisation was applied to the model in 17 different locations to simulate 17 different energy extraction scenarios. The model was run for one-spring neap cycling, lasting 14.8 days. Outputs from each model run were combined with outputs from a non-extraction *baseline* model to assess the hydrodynamic impacts of the modelled extraction scenario in the sandbank vicinity. A set of sedimentary model-runs were also performed for a longer 90-day period with the sediment module activated. A *hard-bottom* method was used to limit potential erosion depths within the sediment model and to ensure realistic sediment supply.

Three *difference metrics* were used to systematically compare the impact of each extraction scenario upon the South Banks. These were the *residual current*, the *residual sediment transport* and the *bed-level evolution*. The difference metrics were used to rank the 17 extraction scenarios in terms of likely impact upon the South Banks from highest to lowest.

The results show that the impact of energy extraction decreases with the distance of array placement from the North-Eastern tip of the South Banks. A propagating eddy shed from the headland is closely related to velocities in this region with energy-extraction decreasing the rotational velocity and life-time of the eddy. The processed modelling outputs are interpreted within the context of the initial morphological analysis to help predict how the sediment transport pathways will be altered. Results suggest that the most favourable locations for maximising power output whilst minimising impacts over the South Banks are two particular regions, T63 or T49.

Contents

List of Figures

List of tables

DECLARATION OF AUTHORSHIP

I, Stephen Geoffrey Haynes

Declare that the thesis entitled:

Tidal Stream Turbines and Sediment Dynamics: The Effects of Array Installation upon the Morphology of a Headland Associated Linear Sandbank

And the work presented in the thesis are both my own, and have been generated by me as the result of my own original research. I confirm that:

- This work was done wholly or mainly while in candidature for a research degree at this University;
- Where any part of this thesis has previously been submitted for a degree or any other qualification at this University or any other institution, this has been clearly stated;
- Where I have consulted the published work of others, this is always clearly attributed;
- Where I have quoted from the work of others, the source is always given. With the exception of such quotations, this thesis is entirely my own work;
- I have acknowledged all main sources of help;
- Where the thesis is based on work done by myself jointly with others, I have made clear exactly what was done by others and what I have contributed myself;
- None of this work has been published before submission

Signed: ……..

Date:…….

1 Introduction

"Warming of the climate system is unequivocal, and since the 1950s, many of the observed changes are unprecedented over decades to millennia. The atmosphere and ocean have warmed, the amounts of snow and ice have diminished, sea level has risen, and the concentrations of greenhouse gases have increased". (pg. 2)

"It is extremely likely that human influence has been the dominant cause of the observed warming since the mid-20th century". (pg. 15)

The Working Group I contribution to the Fifth Assessment Report of the Intergovernmental Panel on Climate Change: Summary for Policymakers

The Inter-governmental Panel on Climate Change's fifth assessment report (IPCC, 2013) collects and presents the accumulated scientific evidence for climate change. Building upon the previous four assessment reports (IPCC; 1990, 1995, 2001, 2007) the panel synthesises data and conclusions from a wide range of studies. Direct measurements of the earth's climate system (temperatures, ocean salinity, atmospheric composition) are combined with climate model simulations and paleoclimate records providing a coherent picture of the history of the climate system and of its possible futures. Central to the IPCC's work is an assessment of the extent to which anthropogenic influences are responsible for warming of the global climate system (i.e. *global warming*).

Global warming is due to the cumulative increase of greenhouse gasses present in the Earth's atmosphere which has occurred since the inception of the Industrial Revolution (~1750s). Most importantly, the burning of fossil fuels to generate

electricity and fuel transportation has significantly increased levels of carbon dioxide within the atmosphere leading to greater global heat retention and an increase in surface temperatures. The need to reduce carbon emissions to negate the worst impacts of anthropogenic climate change is now understood at a governmental level (UK Climate Change Act 2008) although finding practical methods for achieving such large reductions remains challenging, both logistically and politically.

The use of renewable energy technologies to displace generation of electricity from fossil fuels could reduce UK carbon emissions whilst increasing energy security (decreasing reliance upon foreign energy supplies). Particularly relevant to the climate of the UK is the possibility of generating electricity using wind, tidal and wave energies. Each renewable technology presents a different set of engineering challenges. The wind industry is now well established in the UK with on and off-shore wind-farms located at numerous sites around the country. Tidal and wave energy technologies have both reached the full-scale commercial application stage (e.g. SeaGen and Pelamis respectively) although the large-scale, coast-wide application of such technologies is still some way off. Each technology presents a range of engineering and wider contextual problems that need to be addressed and resolved before large scale electricity generation is feasible.

Generation of electricity from the tides can be achieved using one of two methods:

- *Tidal barrage* – Variation in tidal height is exploited by trapping water behind a barrage at high tide and generating electricity using the resultant head difference at low tide
- *Tidal stream generator* – Free-standing or floating generators (often similar to underwater wind-turbines in design) are located in regions of high tidal velocities and extract kinetic energy from the flow.

The generation of electricity using the tidal stream generator approach has received increasing academic, industrial and commercial interest in recent years. An important advantage of tidal energy is the long-term predictability of the tides and, consequently, of resultant energy yields. The possible impacts of this energy-extraction method upon the surrounding submarine environment remain unclear however. In particular it is possible that changes to the hydrodynamic flow regime may alter patterns of sediment movement in the vicinity of a generator. This could have implications for coastal defences, subterranean features such as sandbanks and for the real-world energy yield of the generators.

This study investigates the possible sedimentary impact of installing a large array of tidal stream generators in a specific, real-world location; the Alderney Race, located in the English Channel between Alderney and the Cherbourg Peninsula. Of particular interest is the influence of array installation upon a large submarine sandbank, the Alderney South Banks.

1.1 Aim and Objectives

The primary aim of the study is to investigate the relative impact of various energy-extraction scenarios upon the morphology and sedimentary regime of the Alderney South Banks. The aim will be achieved via the completion of the following 4 objectives:

A. *Analyse and evaluate the morphological and sedimentary regime of the South Banks*

The general morphology of the sandbank will be identified with respect to the literature as a function of the local tidal regime, the coastline and the sandbank footprint. The available high-resolution bathymetry enables a detailed analysis of any bedforms superimposed upon the sandbank which may be used to infer sediment transport pathways.

B. *Develop and validate a coastal-scale numerical model of the Alderney Race*

Multiple bathymetric and coastline datasets will be synthesised and mapped to produce a single bathymetric mesh for the model. A baseline model of the Alderney Race will be validated using tidal elevation data from ports and current data from ADCP deployments. The model results will be used to provide a 'no-extraction' baseline scenario with which to compare the energy-extraction results. A sedimentary model will also be coupled in parallel to this hydrodynamic baseline model with the intention of simulating the impacts of energy extraction upon sediment movement.

C. *Identify and apply a method for parameterising the effects of arrays of tidal stream turbines within the numerical model*

Existing methods for representing tidal stream turbine arrays within numerical models will be summarized and considered. A method for parameterising an array of turbines within the model created through objective B will be implemented to simulate multiple energy-extraction scenarios.

D. *Interpret modelling outputs within the context of the South Banks morphology*

A method for the systematic comparison of energy-extraction outputs with baseline outputs will be developed. Appropriate metrics for the inter-scenario comparison of

different extraction scenarios will be defined and utilised to assess the relative impacts of each hypothetical extraction scheme. Outputs from this comparative analysis phase will then be interpreted within the context of the South Banks morphology as identified under Objective -A above.

1.2 Research hypothesis

Headland associated sandbanks that maintain a dynamic equilibrium within tidal flows are sensitive to the hydrodynamic impacts of large energy extraction schemes.

1.3 Report structure

The main body of this report is divided into the following nine chapters:

Chapter 2 Theory and background relating to tidal energy, computational fluid dynamics, parameterisation of energy extraction, sediment transport and bedforms

Chapter 3 Literature review of existing research relating to sandbank morphology, sediment transport formula and impact of tidal stream turbine arrays upon sediment dynamics.

Chapter 4 Background to the study-site and review of the available datasets.

Chapter 5 Morphological analysis of the Alderney South Banks sandbank.

Chapter 6 Modelling methodology including choice of numerical software, development of the numerical model, energy extraction parameterisation within the model, extraction scenarios and modelling approach.

Chapter 7 Results of the numerical modelling phase including model validation.

Chapter 8 Processing of outputs, comparison of extraction scenarios and discussion.

Chapter 9 Conclusions, ranking of extraction scenarios, unique contribution of the research and recommendations for further work.

2 Theory and Background

2.1 Tidal power

Artificially created tidal reservoirs have been used since at least 600 A.D. to power tidemills for the purposes of flour production. The tidal reservoir is sealed at the high tide, as the external tidal level begins to fall, with the resultant head-difference being used to drive a watermill at low-tide. Archaeological remains of the earliest known tidemills have been discovered on the Irish coast (Squatriti, 2000) with the practice spreading to England, Continental Europe and, eventually, North America. In 1966 the first large-scale modern-era tidal power station was opened in Le Rance, France. Operating upon the same principle as its tidemill predecessors, Le Rance power station consists of a large barrage spanning the Rance River estuary in Brittany, France. The barrage was designed with an installed electricity generating capacity of 240 MW and yields a yearly output of 540GW (Charlier, 1997). Although a number of significantly smaller tidal barrages have been successfully built and operated in China, Russia and Canada, the future of large-scale mega-barrage projects remains unclear. The potential environmental and ecological impacts, significant disruption to shipping and the political issues of funding and instigating such colossal schemes have tempered enthusiasm for tidal barrage schemes.

The considerable difficulties associated with tidal barrages have fuelled interest in and development of an alternative method for generating electricity from the tides. The use of stand-alone tidal energy convertors (TECs) to generate electricity from tidal streams has been seriously considered since the 1970s (Lissaman and Radkey, 1979). Although a variety of designs have been mooted the most prevalent are directly inspired by horizontal-axis wind turbines and are typically known as *tidal stream turbines*.

Tidal turbines typically have much smaller diameters than wind turbines (8-16m compared with 40-80m) due to the fundamental restriction of the water depth. Additionally, the differences in maximum flow velocities encountered (tidal flows < 5m/s; wind flows < 25m/s) and momentum energy per cross-sectional-area produce a different set of design criteria for tidal turbines. The significantly higher density of water compared to air results in much higher stresses upon the turbine blades.

Tidal turbines are much harder to install and maintain than wind turbines for obvious reasons. Installation of turbines in what are inherently high-speed tidal flows is particularly challenging and there are additional issues relating to bio-fouling that have implications for performance and maintenance. From a wider perspective the impacts of tidal turbines upon marine life and local seabed morphology are also important issues that remain insufficiently explored. Despite manifold challenges the generation of power using tidal turbines remains an inviting enterprise due to one factor unique to tidal power: energy forecasting. The unpredictability of energy supplied by most renewable technologies (wind, solar, wave) is a major problem in terms of integrating the electricity supplies into a nationalised grid system. In stark contrast to this the electricity generated from tidal devices is entirely predictable decades into the future and is completely regular with daily maximums delivered throughout the year (i.e. there is little seasonal variability unlike other renewables).

If tidal turbines are to compete with tidal barrages in terms of electricity generating capacity it will be necessary for multiple turbines to be installed in large underwater arrays analogous to a wind farm. The question of how turbines can be arranged within an array to maximise power output is an active research topic of surprising complexity. Optimum solutions are typically dependent upon the specifics of the local bathymetry and tidal flow regime such that site-specific modelling is required. Even so, it is well established that the longitudinal spacing between turbines must be much larger than the lateral spacing due to the stream-wise pattern of velocity deficits observed downstream from turbines (see section 2.4).

2.2 Computational fluid dynamics

The use of computational methods for investigating the behaviour of fluid flows has increased significantly in recent times with the advent of cheap computing power. Computational fluid dynamics (CFD) methods are widely used in many areas of industry and academia to investigate and predict a diverse range of phenomena. The methods for modelling free-surface tidal flows required for this study are well-established and the problems involved well-defined. It is therefore possible to focus narrowly on the pertinent aspects of CFD whilst discarding many irrelevant aspects that do not apply for this application.

The fundamental equations of fluid mechanics, the conservation equations, will first be stated and the possibility of direct solution of the equations discussed. This will be followed with a discussion of CFD methods and approaches for simplifying and solving the equations within the context of our specific application; free-surface flows.

2.2.1 Navier-Stokes equations for incompressible flow

Figure 2.1 illustrates a hypothetical *control volume* of fluid in the shape of a cube with its centre of mass defined in Cartesian co-ordinates as (x,y,z). The fundamental scientific principle of the *conservation of mass* can be stated in this context as follows:

Rate of mass increase in control volume	=	Combined rate of mass-flow into control volume	(2.1)

The combined flow of mass across the six boundaries of the cube must be reflected in the total mass present within the volume i.e. mass must be conserved.

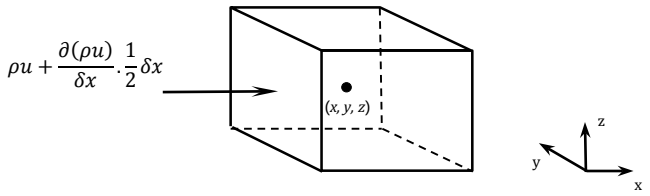

Figure 2.1 Cubic *control volume* of fluid defined using Cartesian co-ordinates (based upon diagram from Versteeg and Malalasekera; 1995). Formulations for the flow of mass across each face are included with the influx of mass *into* the volume given a positive sign relating to an *increase* in mass.

The rate of mass increase due purely to density variations within the control volume can be expressed as:

$$\frac{dm}{dt} = \frac{\partial \rho}{\partial t}\delta x \delta y \delta z \tag{2.2}$$

The mass flow rate across each boundary is equal to the product of three values (e.g. using the left face); the velocity component normal to the face, $u - \frac{\partial u}{\delta x}.\frac{1}{2}\delta x$; the density, ρ; and the cross-sectional area of the boundary, $\delta y \delta z$. The net flow-rate of mass into the volume can be expressed as the sum of the flow-rate across each of the six boundaries:

$$\left(\rho u - \frac{\partial(\rho u)}{\partial x}\frac{1}{2}\delta x\right)\delta y \delta z - \left(\rho u + \frac{\partial(\rho u)}{\partial x}\frac{1}{2}\delta x\right)\delta y \delta z + \left(\rho v - \frac{\partial(\rho v)}{\partial y}\frac{1}{2}\delta y\right)\delta x \delta z -$$
$$\left(\rho v + \frac{\partial(\rho v)}{\partial y}\frac{1}{2}\delta y\right)\delta x \delta z + \left(\rho w - \frac{\partial(\rho w)}{\partial z}\frac{1}{2}\delta z\right)\delta x \delta y - \left(\rho w + \frac{\partial(\rho w)}{\partial z}\frac{1}{2}\delta z\right)\delta x \delta y \tag{2.3}$$

It can be seen that equation (2.2) corresponds to the left hand side of (2.1) and equation (2.3) to the right hand side. Equating (2.2) with (2.3), grouping the terms on the left hand side of the equals and dividing by the control volume $\delta x \delta y \delta z$ gives:

$$\frac{\partial \rho}{\partial t} + \frac{\partial(\rho u)}{\partial x} + \frac{\partial(\rho v)}{\partial y} + \frac{\partial(\rho w)}{\partial z} = 0 \tag{2.4}$$

For hydrodynamic flows $\frac{D\rho}{Dt} \approx 0$ (i.e. liquids can be treated as incompressible) therefore equation (2.4) becomes:

$$\frac{\partial u}{\partial x} + \frac{\partial v}{\partial y} + \frac{\partial w}{\partial z} = 0 \tag{2.5}$$

This is the mass continuity equation for incompressible flows.

Newton's second law states that the rate of change of linear momentum is equal to the sum of all external forces acting upon the control volume:

$$F = \rho \frac{Du}{Dt} \quad \text{in the x-axis direction} \tag{2.6}$$

$$F = \rho \frac{Dv}{Dt} \quad \text{in the y-axis direction} \tag{2.7}$$

$$F = \rho \frac{Dw}{Dt} \quad \text{in the z-axis direction} \tag{2.8}$$

The forces acting on the fluid are typically divided into *body forces* that act at all points within the control volume (gravity, Coriolis force, centrifugal force) and *surface forces* that only act at the surface of the control volume (pressure, surface tension, viscous forces).

To calculate the stress of the fluid within the control volume the pressure and viscous surface forces must be defined and summed in each of the three Cartesian axes. Pressure forces (*p*) act normal to the surfaces of the control volume whereas viscous stresses (τ) act in all planes on each of the 6 boundaries of the cube. A dual suffix notation τ_{ij} is used to reference the viscous stresses with *i* denoting the axis to which the face is normally aligned and *j* specifying the direction of stress at this face (e.g. τ_{xy} specifies a stress in the y-direction acting at either of the two faces normal to the x-axis).

The surface forces are summed for each axis separately resulting in a momentum equation for each spatial axis (i.e. 3 momentum equations). The surface forces acting in the x-axis are shown in Figure 2.2. It can be seen that the pressure forces only act on the two faces normal to the x-axis and that viscous forces from all 6 of the control volume faces need to be included in the summation.

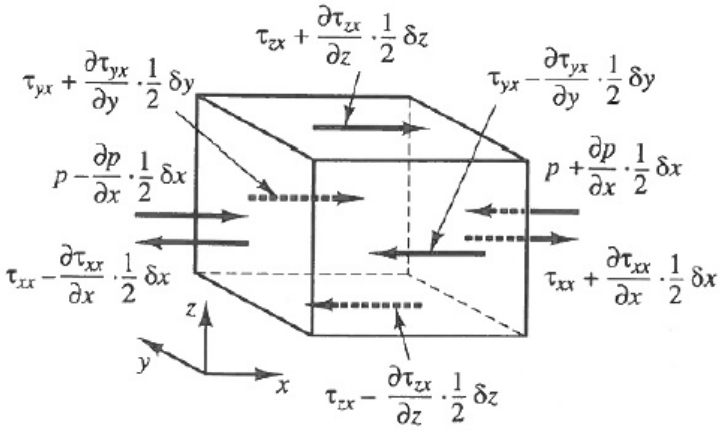

Figure 2.2 Stress components in the x-direction

Summing these stress components together, cancelling terms and dividing by the control volume $\delta x \delta y \delta z$ yields the net force per unit volume due to surface forces acting in the x-axis:

$$-\frac{\partial p}{\partial x}+\frac{\partial \tau_{xx}}{\partial x}+\frac{\partial \tau_{yz}}{\partial y}+\frac{\partial \tau_{zx}}{\partial z} \tag{2.9}$$

Substituting (2.9) into (2.6) and representing the body forces per unit mass with an axis-specific term, B_x, gives the momentum equation in the x-axis:

$$\rho\frac{Du}{Dt}=-\frac{\partial p}{\partial x}+\frac{\partial \tau_{xx}}{\partial x}+\frac{\partial \tau_{yx}}{\partial y}+\frac{\partial \tau_{zx}}{\partial z}+B_x \tag{2.10}$$

Performing the same surface force summation in the y- and z- axes and substituting appropriately into (2.7-2.8) gives two more momentum equations:

$$\rho\frac{Dv}{Dt}=-\frac{\partial p}{\partial y}+\frac{\partial \tau_{xy}}{\partial x}+\frac{\partial \tau_{yy}}{\partial y}+\frac{\partial \tau_{zy}}{\partial z}+B_y \tag{2.11}$$

$$\rho\frac{Dw}{Dt}=-\frac{\partial p}{\partial z}+\frac{\partial \tau_{xz}}{\partial x}+\frac{\partial \tau_{yz}}{\partial y}+\frac{\partial \tau_{zz}}{\partial z}+B_z \tag{2.12}$$

Assuming a Newtonian fluid (stress ∝ strain rate), isothermal flow (constant temperature) and, consequently, constant dynamic and kinematic viscosities, the viscous stress tensor for an incompressible fluid can be presented in Cartesian co-ordinates (Cengal and Cimbala, 2006) as:

$$\tau_{ij}=\begin{pmatrix}\tau_{xx} & \tau_{xy} & \tau_{xz}\\ \tau_{yx} & \tau_{yy} & \tau_{yz}\\ \tau_{zx} & \tau_{zy} & \tau_{zz}\end{pmatrix}=\begin{pmatrix}2\mu\frac{\partial u}{\partial x} & \mu\left(\frac{\partial u}{\partial y}+\frac{\partial v}{\partial x}\right) & \mu\left(\frac{\partial u}{\partial z}+\frac{\partial w}{\partial x}\right)\\ \mu\left(\frac{\partial v}{\partial x}+\frac{\partial u}{\partial y}\right) & 2\mu\frac{\partial v}{\partial y} & \mu\left(\frac{\partial v}{\partial z}+\frac{\partial w}{\partial y}\right)\\ \mu\left(\frac{\partial w}{\partial x}+\frac{\partial u}{\partial z}\right) & \mu\left(\frac{\partial w}{\partial y}+\frac{\partial v}{\partial z}\right) & 2\mu\frac{\partial w}{\partial z}\end{pmatrix} \tag{2.13}$$

Substituting the relevant terms from (2.13) into equation (2.10) for the x-axis we get:

$$\rho\frac{Du}{Dt}=-\frac{\partial p}{\partial x}+2\mu\frac{\partial^2 u}{\partial x^2}+\mu\frac{\partial}{\partial y}\left(\frac{\partial v}{\partial x}+\frac{\partial u}{\partial y}\right)+\mu\frac{\partial}{\partial z}\left(\frac{\partial w}{\partial x}+\frac{\partial u}{\partial z}\right)+B_x \tag{2.14}$$

Rearranging viscous terms and assuming that the velocity components are smooth functions of x, y and z (i.e. the order of differentiation is irrelevant; ibid.) gives:

$$\rho\frac{Du}{Dt}=-\frac{\partial p}{\partial x}+\mu\left[\frac{\partial}{\partial x}\left(\frac{\partial u}{\partial x}+\frac{\partial v}{\partial y}+\frac{\partial w}{\partial z}\right)+\frac{\partial^2 u}{\partial x^2}+\frac{\partial^2 u}{\partial y^2}+\frac{\partial^2 u}{\partial z^2}\right]+B_x \tag{2.15}$$

The terms within the circular brackets are identical to the left hand side of the mass continuity equation for incompressible flows (2.5) and can therefore be equated to zero. Substituting the square of the Laplace operator, ∇, of the velocity component, *u,* for the three second-order differential terms gives the x-component of the momentum equation:

$$\rho \frac{Du}{Dt} = -\frac{\partial p}{\partial x} + \mu \nabla^2 u + B_x \tag{2.16}$$

Repeating the same process (2.13-2.15) for the y- and z- axes gives:

$$\rho \frac{Dv}{Dt} = -\frac{\partial p}{\partial y} + \mu \nabla^2 v + B_y \tag{2.17}$$

$$\rho \frac{Dw}{Dt} = -\frac{\partial p}{\partial z} + \mu \nabla^2 w + B_z \tag{2.18}$$

Taken together, the continuity equation (2.5) and the three momentum equations (2.16-2.18) are the Navier-Stokes equations for incompressible flow. These equations are non-linear, second-order partial-differentials and contain 4 unknown terms (3 velocity components and pressure). Direct solution of the Navier-Stokes equations is only possible for very simple, steady flows at comparatively low Reynolds numbers (i.e. Re <500). Solutions for unsteady, turbulent flows are effectively impossible due to the complex, non-linear nature of turbulence.

2.2.2 Reynolds-averaged Navier-Stokes (RANS) equations

For many CFD tasks a time-averaging process is typically applied to the Navier-Stokes equations to help describe and simulate turbulent flows. The instantaneous velocity components, e.g. *u*, at each point are decomposed into a time-averaged term, $\bar{u}$, and a fluctuating term, u', as follows:

$$\begin{aligned} u &= \bar{u} + u' \\ v &= \bar{v} + v' \\ w &= \bar{w} + w' \end{aligned} \tag{2.19}$$

The time-averaged terms are by definition steady, gradually varying terms and can be used to describe the average properties of incompressible flow fields very

effectively. Conversely, the fluctuating terms consist of turbulent (i.e. chaotic) variations in velocity around the time-averaged mean values. Their inclusion in the Navier-Stokes equations presents significant theoretical and practical challenges in the quest to accurately model unsteady, turbulent flows.

Substituting the decomposed velocity components (2.19) into the Navier-Stokes equations in each spatial axis (2.16-2.18), time-averaging the resultant equations and arranging the fluctuating velocity components on the right hand side gives:

$$\rho \frac{D\bar{u}}{Dt} = -\frac{\partial \bar{p}}{\partial x} + \mu \nabla^2 \bar{u} + B_x + \left[-\frac{\partial \overline{u'^2}}{\partial x} - \frac{\partial \overline{u'v'}}{\partial y} - \frac{\partial \overline{u'w'}}{\partial z} \right] \tag{2.20}$$

$$\rho \frac{D\bar{v}}{Dt} = -\frac{\partial \bar{p}}{\partial y} + \mu \nabla^2 \bar{v} + B_y + \left[-\frac{\partial \overline{u'v'}}{\partial x} - \frac{\partial \overline{v'^2}}{\partial y} - \frac{\partial \overline{v'w'}}{\partial z} \right] \tag{2.21}$$

$$\rho \frac{D\bar{w}}{Dt} = -\frac{\partial \bar{p}}{\partial z} + \mu \nabla^2 \bar{w} + B_z + \left[-\frac{\partial \overline{u'w'}}{\partial x} - \frac{\partial \overline{v'w'}}{\partial y} - \frac{\partial \overline{w'^2}}{\partial z} \right] \tag{2.22}$$

The extra bracketed terms on the right hand side of each momentum equation consist of products of fluctuating velocity components (i.e. turbulent fluctuations) known as the *Reynolds stresses*. Physically these terms represent the flux of momentum in or out of the control volume due to turbulent fluctuations (Davidson, 2004) and their presence means that the RANS equations cannot be *closed* (i.e. solved exactly). The *closure problem of turbulence* is often the most challenging aspect for many CFD applications and a wide range of approximations, or *turbulence models*, have been developed to tackle it.

2.2.3 Solving the RANS equations: discretization in space and time

To model fluid flows computationally a discretization scheme is necessary to divide the continuous real-world spatial domain into a grid of discrete points. The three most common schemes are the Finite Difference method (FD), the Finite Element method (FE) and the Finite Volume method (FV). Essentially each discretization method constitutes a different system for mapping the chosen mathematical scheme with its related variables (i.e. RANS; pressure and three velocity components) onto the grid producing a network of interconnected algebraic equations. A discretization in time is also required to determine the temporal frequency at which the mathematical model

is solved for each point in the grid. The temporal interval between consecutive solutions of the equations is called the *time step*.

A common technique for solving the RANS equations when the finite element method is used is known as the *Method of characteristics.* The RANS equations constitute a set of hyperbolic partial differential equations (PDEs) that are challenging to solve because of the multiple unknown variables. The method of characteristics can be used to convert the RANS equations to a set of ordinary differential equations (ODEs) that have just one unknown variable each and are consequently simpler to solve (Anderson, 1995). The solution of the RANS equations is often employed as an iterative process with multiple successive solutions (i.e. hyperbolic curve fits) performed at each time-step until the required accuracy is attained.

2.2.4 Bottom friction

When fluids flow laterally across a domain a *bottom shear stress* acts upon the fluid in the opposite direction to the fluid velocity (Hervouet, 2007). This stress reduces velocities immediately adjacent to the bottom-boundary (often representing the sea-floor) and removes energy from the flow. The velocity deficit induced at the boundary decreases with distance from the bottom, typically reducing to zero at a certain distance above the bottom boundary. The characteristics of this depth-wise velocity profile are primarily a function of the flow velocity and the 'roughness' of the surface at the boundary, characterised by the *roughness length*, z_0.

The roughness length is determined by the geometry of the sea-bed and describes how elements of the geometry protrude into the flow. In steady uniform turbulent flow a laminar, viscosity-dominated *viscous sub-layer* forms near to the bottom boundary (Middleton and Southard, 1984). If the roughness elements are large enough to protrude through this viscous sub-layer then the friction acting against the flow increases significantly causing additional eddy formation and increased energy loss (ibid.). This is the case for most fast, tidal flows and, as such, the roughness length is a useful metric for characterising the relationship between bottom friction and the geometry of the sea-floor.

The effect of bottom friction can be included in coastal-area CFD models using a non-dimensional friction coefficient, *C,* applied domain-wide. A number of empirically

derived laws have been developed to parameterise the effects of bottom friction upon fluid flows, each with a particular approach to defining the problem and a related friction coefficient.

Chézy's formula describes the resistance to fluid flow through a sloped channel (Graebel, 2001). The mean flow velocity is stated as a function of the channel depth, channel bottom slope, gravity and a friction coefficient, C_f. The equations were based upon experiments conducted on canals and the River Seine in 1769 although they are analytically derived (Massey; 1984). The formulae of both Manning and Strickler develop Chézy's formula using empirical data and are widely used for relating mean flow velocities through channels to bottom friction.

Johann Nikuradse's experiments focussed on fluid flow through prepared pipes with uniform grains of sand glued to the wall (Massey; 1984). The *Nikuradse roughness,* k_s , was proposed as a single metric for defining the effective roughness of a surface across a wide range of Reynolds numbers (The size of the viscous sub-layer is affected by the Reynolds number, *Re*). The focus on manifesting roughness as uniform sand sizes is convenient for coastal modelling and a range of relationships between k_s and the median sediment grain size, d_{50}, have been proposed (i.e. $k_s = 2.5d_{50}$; Soulsby, 1997). The Nikuradse roughness is also easily related to the *roughness length*, z_0, where $k_s = 30z_0$ (Soulsby, 1997). Most importantly, the Nikuradse approach is more 'physical' than the Chézy, Manning and Strickler laws and can be used to match the roughness of the seabed with related logarithmic velocity profiles (and vice versa).

2.3 TELEMAC

The TELEMAC hydro-informatics system is the result of over two decades of research and development by Électricité de France. At its core TELEMAC is a two dimensional numerical model (TELEMAC-2D) that uses the finite-element method to simulate free-surface hydrodynamic flows. Specifically developed for a wide range of applications, TELEMAC has been employed for coastal-area model scale studies, tidal simulations, river-engineering, estuarine studies, ocean energy research and harbour engineering. TELEMAC is now open-source software allowing modifications to be made at the code-level and is well documented with a long history of use in both the private and academic sectors.

2.3.1 Model architecture

TELEMAC is written in the Fortran-90 programming language with model runs controlled and implemented via a collection of interconnected, user-prescribed input files. The 'Steering file' acts as a master-file for each simulation and is used to define the other user-input files. Figure 2.3 illustrates the internal file connectivity within TELEMAC. The model mesh is prescribed in the geometry file and there are also files for defining the boundary conditions and any additional datasets. Simulation outputs are collected in a single results file and a reference file may also be included to compare the model outputs with alternative runs or real-world datasets. A fortran file can be used to interact directly with the model architecture and re-code or create subroutines embedded within the model.

All general parameters relating to each simulation (i.e. time step, run-time, processors used) are specified in the steering file in addition to various physical and numerical parameters (i.e. bottom friction, turbulence schemes, Coriolis, initial conditions, inclusion of tidal flats, solver options). It is possible for TELEMAC-2D to be coupled externally with various modules capable of simulating wave propagation (TOMAWAC), sediment transport (SISYPHE) and changes in bottom level due to dredging (DREDGESIM).

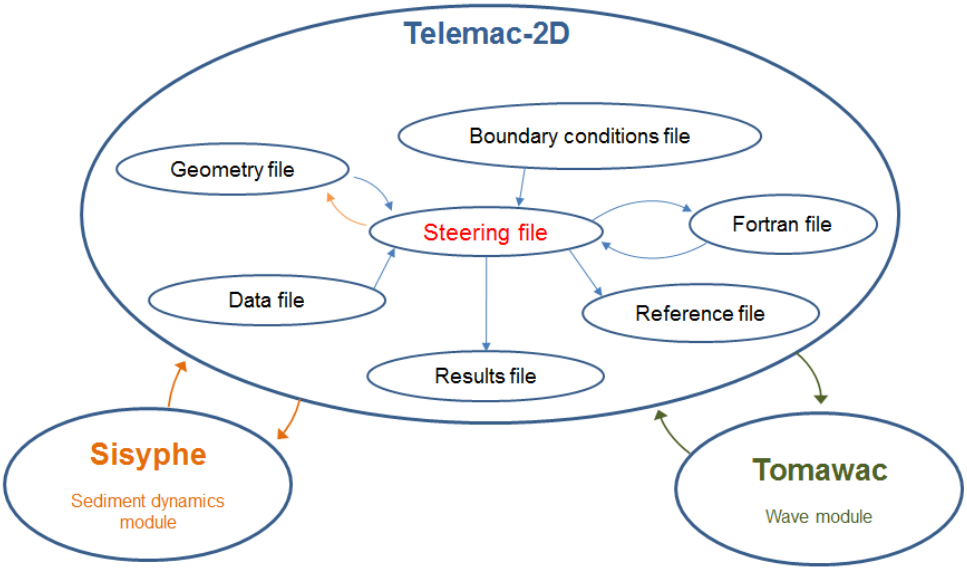

Figure 2.3 Architecture of the TELEMAC hydro-informatics system. Arrows indicate the flow of information between user files within TELEMAC-2D and also when external modules are coupled with the hydrodynamic model.

2.3.2 TELEMAC-2D and unstructured meshes

TELEMAC-2D solves the Saint-Venant free surface flow equations using a finite element approach. The model domain is discretised into an un-structured triangular mesh as shown in Figure 2.4. The bathymetric depth values are then mapped onto this mesh. The Saint-Venant equations are solved at each model time-step resulting in values for depth-averaged velocity and water depth at each node of the mesh.

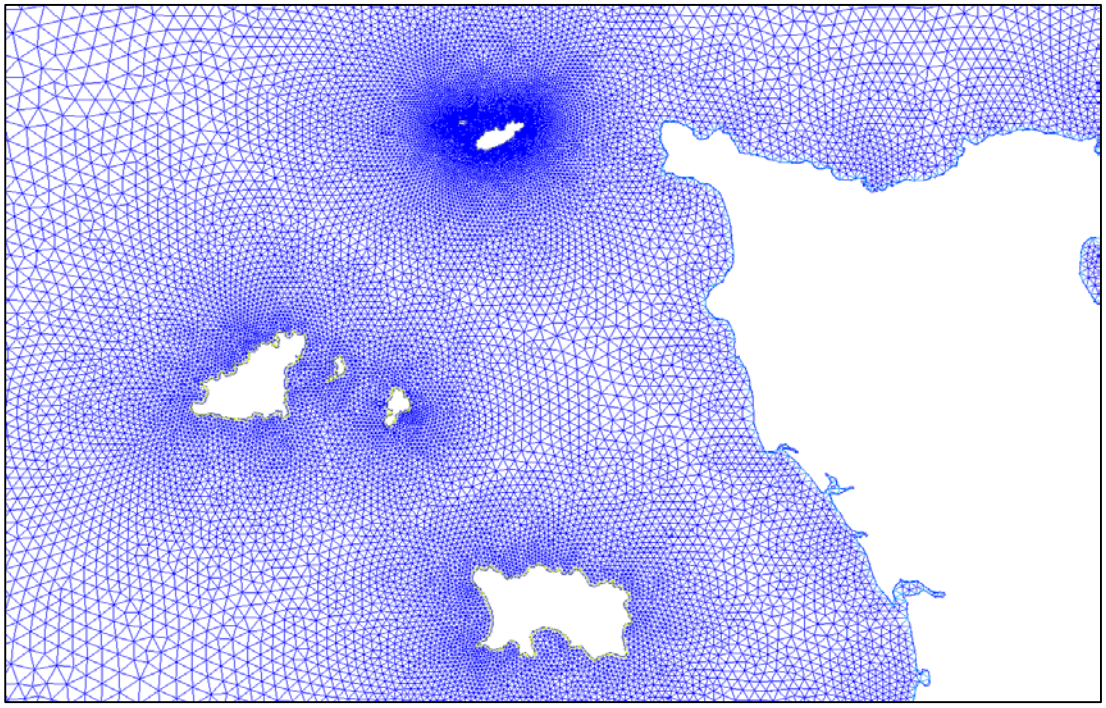

Figure 2.4 Unstructured bathymetric mesh example generated for the study site. Mesh resolution is increased close to the coastlines and reduced in regions far from the coasts.

The use of un-structured meshes is particularly useful for coastal area models where coastlines are often complex and irregular. The ability to vary model resolution across the model domain allows computing power to be focussed on the areas of maximum hydrodynamic complexity allowing better results and shorter runtimes (compared to a regular, finite difference mesh with the same number of nodes). Meshes can be generated using an affiliated software programme called Blue Kenue developed by the National Research Council Canada. Various parameters for mesh density and edge growth ratios can be specified with the programme automatically optimising the resultant mesh using an iterative process.

2.3.3 Boundary conditions

Every boundary point within a mesh must be specified as either a *closed boundary (wall)* or as a particular type of *open boundary*. Open boundaries must be specified by providing at least one of three values at each boundary point: prescribed depth, prescribed velocity or prescribed flowrate. It is also possible to simultaneously prescribe elevation and velocity values. Prescribed values can remain constant throughout the simulation or can be programmed via the fortran file to vary with time. For modelling of coastal scale tidal models the prescription of both depth and velocity values at boundary points would be preferable although velocity information is typically unavailable. Prescription of depth values alone results in an 'under-constrained' model with not enough information being specified at the domain boundary (Telemac user manual, 2010). To solve this problem TELEMAC provides an option for calculating the missing velocity values using the *Thompson boundary conditions* (Thompson; 1987, 1990). The method allows depth values to be prescribed at the boundary nodes whilst also allowing outgoing waves to exit the domain.

2.3.4 Sediment module (SISYPHE)

SISYPHE is a sediment transport and morphological model that can be coupled to, and run in parallel with, TELEMAC-2D. Sediment transport rates at each grid node are calculated as a function of the hydrodynamic outputs from TELEMAC-2D (flow velocity, water depth) and sediment characteristics specified in SISYPHE (median grain size, grain density, settling velocity). Classical sediment transport formulae are used to determine bed-load and suspended-load transport components with the resultant bottom evolutions determined by a solution of the Exner equation (see section 2.6.1). Bed friction is output from the hydrodynamic model and split into *skin friction* and *form-drag* components with various options for 'skin friction correction' (sediment transport rates are calculated as a function of the *skin friction* component only). Bed-level evolutions calculated in SISYPHE can be fed back into the hydrodynamic model allowing the bathymetric grid to be updated thus allowing non-linear feedback behaviour to emerge, as represented in Figure 2.3. The effects of sea-bed inclination upon sediment movement can be incorporated into the transport rates. Also of particular interest for this study, a *rigid bottom* layer can be specified to impose a maximum depth of erosion thereby controlling sediment supply.

2.4 Energy extraction: parameterisation of turbine arrays

Energy extraction using a tidal stream turbine impacts the local hydrodynamic regime in a number of ways. Most fundamentally, momentum energy is removed from the flow causing a reduction in flow velocity immediately downstream from the turbine. The passage of water around the turbine blades and structure also generates turbulence which is advected downstream with the flow. This downstream region of reduced velocities (or *velocity deficit*) and increased turbulence is known as the *wake*. Flows passing around the sides of the turbine progressively mix into the wake laterally and vertically with distance downstream from the turbine. Eventually the wake is mixed back into the general flow and the upstream velocity restored (in the case of uniform flow).

When multiple turbines are present in the flow then the wakes of separate turbines may interact. If turbines are spaced at intervals along the streamline then wakes from upstream turbines can reduce the immediate upstream velocities at turbines downstream (i.e. the wake has not been sufficiently mixed back into the ambient flow). This wake interaction has implications for projected energy yields for large multi-turbine extraction schemes. Multi-wake interactions also create challenges for hydrodynamic modelling of turbine arrays. Simulating the cumulative impact of successive rows of turbines, and also the downstream interaction of laterally spaced turbine wakes, is a complex problem.

2.4.1 Approaches to wake modelling for wind farms

Modelling of tidal arrays has been guided and informed by approaches developed in the comparatively well-established wind-turbine industry. Three methods developed to model wake interaction for wind farms are outlined in a review paper by Crespo et al. (1999) and briefly summarised here:

1. *Area-averaged roughness models* – These models posit a logarithmic velocity profile for the wind with ground roughness included as the key input. Wind turbines are represented as an extra drag force in the flow which is included in the ground roughness term. The velocity deficit downwind from each row has been observed to approach a constant value after ~4 rows as shown in Figure 2.5 (Frandsen et. al; 2006). For ‘large’ wind farms this means that the

combined effect of the turbines can be represented as a homogenous added-drag term applied over the area of the array and combined with the local ground roughness.

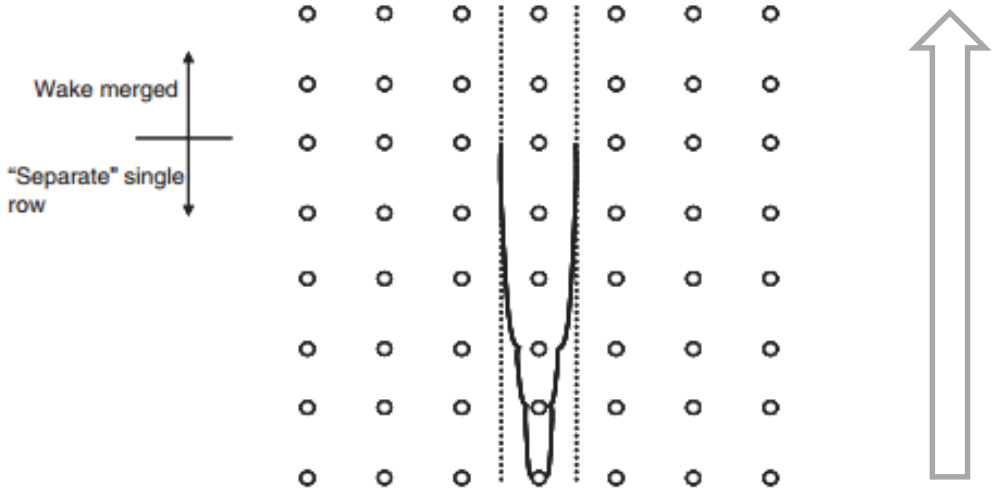

Figure 2.5 Progressive expansion and eventual merging of successive turbine wakes downwind from the front row of a wind farm. Diagram from Frandsen et al (2006).

2. *Individual wakes* – Each individual turbine wake within the farm is simulated, often using a high-resolution model mesh. Numerous individual wake models have been developed varying widely in terms of approach and complexity. The most basic schemes employ simplified regional wake models with a two-step wake scheme (near-wake, transition and far-wake; Crespo et. al, 1999). The most complex models simulate all aspects of the flow-turbine interaction using high-resolution, computationally-intensive, 3-dimensional models.

3. *Wake superposition models* – Models or data-sets relating to single-turbine wakes are applied to all of the turbines in a wind farm. Various superposition schemes are used to superimpose the respective velocity deficits of overlapping wakes. The linear superposition of the squares of velocity deficits used in Katic et al. (1987) provides a good fit with experimental data. Although superposition models have been relatively successful compared to the first two methods mentioned above, the assumptions involved are not physically meaningful and can lead to erroneous results (such as negative velocities due to the superposition of multiple velocity deficits; Crespo et. al, 1999).

2.4.2 Applicability of wind-based approaches within coastal models

Adapting wind farm modelling methods for use with tidal turbine arrays requires consideration of a number of additional factors. The much larger density of water compared to air has implications for turbulent behaviours within the flow, momentum flux, downstream velocity deficits and power output. Significantly, tidal flows possess an additional upper boundary, the free surface, in addition to the ground/seabed layer. The limited depth of the flow also has implications for downstream flow speeds (Blunden, 2009) and the impact of free surface gradients must be considered.

Element sizes in large-scale coastal models are typically too large to resolve individual tidal stream turbines (i.e. 50m-5km). Detailed, high-resolution, 3-dimensional modelling of single tidal stream turbines is an active research topic but the large scale modelling of turbine arrays with such precision is not currently practicable. The computational costs are too high to apply direct simulation methods to large numbers of turbines in coastal regions. This factor prevents the use of individual wake methods and makes the use of wake superposition models unpractical.

Area-averaged bed-roughness models are, conversely, well suited for application to coastal models. The area-averaged nature of the added roughness term means that the mesh does not need to resolve individual turbines. The only requirement is that the array is resolved to a reasonable extent (i.e. multiple mesh nodes are situated within the array area). Also, the added drag term can be summed with the local bed roughness values (i.e. bottom friction) over the extent of the array. This is computationally efficient, logistically simple and easily applicable within existing coastal modelling systems (i.e. TELEMAC, POLCOMS, MIKE).

2.4.3 Area-averaged bed roughness approach to tidal array modelling

Area-averaged roughness methods have been adapted to model tidal turbine arrays situated in channels (Sutherland, 2007) and in accelerated tidal-flows adjacent to a coastal headland (Blunden, 2009). A primary challenge for such area-averaged approaches is the derivation and specification of depth-wise velocity profiles across the area of the turbine array.

Frandsen (1992) developed a method for wind farms where two separate logarithmic velocity profiles (one extending above the turbine hub and one below) are interfaced at the turbine hub height. A single continuous depth-wise velocity profile is produced that incorporates both the characteristics of the bottom boundary layer and the effect of turbine drag upon flow speeds. Blunden (2009) adapted and expanded this hub-height profile-matching approach for tidal stream turbines. Ideas from boundary layer theory, real-world ADCP velocity profiles, CFD model outputs and flume-based laboratory data were combined with Frandsen's methods to originate a new model for characterizing flow in large tidal arrays. Theoretically the model is only valid for infinitely large arrays of turbines. In practice the approach gives good results if arrays have enough rows for velocity deficits to stabilise as illustrated in Figure 2.5. The growth of the wake deficits across the first ~4 rows of the turbines (*edge effects*) are ignored by the area-averaged approach.

This semi-empirical model allows the calculation of an equivalent added drag coefficient which can be easily incorporated into 2D depth-averaged models. The combined hydrodynamic drag of the array turbines is effectively 'spread' across the area of the array producing a single drag term that is combined with the local bed roughness value at each model mesh node. Logistically this involves the specification of a number of parameters relating to turbine spacing within the array, individual turbine parameters (i.e. turbine diameter, rated speed of the device) and the number of turbines within the array.

2.5 Fundamentals of sediment transport

Subaqueous sediment is typically grouped into two categories based upon size and consequent behaviour; *cohesive* and *non-cohesive*. Cohesive sediment particles (referred to as muds, clays or silts) are <63 microns and are attracted to each other due to electrostatic forces. Non-cohesive sediments (sands and gravel) are >63 microns and can be understood as particles influenced individually by traditional mechanics without any significant inter-particle electrostatic attraction.

Cohesive and non-cohesive sediments behave differently, are produced from different sources and are, subsequently, typically found in different locations.

Tidal currents are often the dominant drivers of sediment transport (although wave action can generate currents and increase bed shear stresses - Soulsby, 1997). As the tidally driven currents pass over the seabed, friction is exerted that can be quantified as a *bed shear-stress*. This consists of a force exerted by the flow per unit area of the bed (N/m^2) and is the key physical variable used to calculate/predict sediment transport.

The bed shear stress is often presented in one of three formats that are all related to each other via sediment and water characteristics:-

Format	**Symbol**	**Relationship**	**Useful for**
Bed shear stress	τ_0	Force/unit area (N/m^2)	
Friction velocity	u_*	$u_* = (\tau_0/\rho)^{1/2}$ ρ = water density	Conversion made for mathematical convenience (Soulsby, 1997)
Shields parameter	θ	$\theta = \frac{\tau_0}{g(\rho_s - \rho)d}$ d = diameter of sediment grains ρ_s = Sediment density	Non-dimensional representation of shear-stress

At low velocities sand on the seabed is not affected by the flow. At a particular flow velocity u_{cr} (or equivalent bed shear stress τ_{0cr} or θ_{cr}) grains of sand begin to move. This value is the *critical bed-shear velocity* (or *critical bed shear-stress*) for the onset of sediment transport. This is also referred to as the *threshold of motion*. The threshold of motion is dependent upon sediment size, bed-slope and the way in which the flow interacts with the sea-bed.

Once sand is in motion it travels in one of two modes; as *bedload* or as *suspended sediment*.

Bedload transport occurs at bed shear stresses close to the critical bed-shear stress. The sand particles roll and hop along the seabed but never completely leave the seabed for an extended period of time.

Suspended sediment transport occurs at shear stresses that are significantly larger than the critical bed shear stress. Sand is mixed up into the flow where it is transported at the same speed as the current. This suspended sediment is deposited at such a point where the shear stresses/flow velocity falls below the critical value.

Many empirical relationships have been posited for both bedload and suspended sediment transport that calculate transport as some function of both the critical and the instantaneous bed shear-stress (i.e. τ_{0cr} and τ_0) along with other values relating to sediment and seabed roughness characteristics.

Any *tidal asymmetry* exhibited by tidal flows at a real-world site will have a significant effect upon the long term sediment dynamics of an area. Tidal asymmetry refers to the regular difference in current speeds between the ebb and flood tide. Assuming that the same quantity of water must ebb and flood past the same point then it can be seen that shorter-phases of the tide (i.e. a shorter ebb than flood phase) will result in higher current magnitudes. The shorter phase of the tide that exhibits increased current magnitudes is said to be *dominant*. Tidal asymmetry is particularly important to the movement of sediment because of the non-linear nature of sediment transport and net sediment transport is typically in the direction of the tidal-dominance.

2.6 Sediment transport modelling

The earliest sediment transport models were developed in the 1980's (Mahera and Narsis; 2013) and the field still persists as a particularly challenging research area. Subaqueous sediment movement concerns the complex interaction of hydrodynamic flows and sediment. A diverse range of physical processes (i.e. turbulence, grain settling, thresholds of motion) combine to produce non-linear and essentially stochastic behaviours that are particularly difficult to determine and predict. Numerical modelling of such a complicated dynamic introduces extra difficulties and challenges.

2.6.1 Approaches to sediment transport modelling

Most sediment transport models are designed to be coupled to existing hydrodynamic models. Often the flow of information is one-way with an independent hydrodynamic model providing inputs to the sedimentary model. The spatial resolution of coastal

models is typically too low to resolve the mechanisms that combine to produce sediment movement. It is therefore necessary to parameterise the sub-grid behaviours such that the generalised sediment behaviour may be represented at each mesh node (Amoudry; 2008). For some modelling applications it is necessary to feed outputs from the sediment model (i.e. bed level changes) back into the hydrodynamic model to enable the real-world non-linear relationship between sediment movement and fluid flows to occur.

Sediment models are based upon a conservation of mass relationship called the Exner equation with variations in calculated sediment flux balanced by modifications to the bed elevation (ibid.):

$$\frac{\partial \eta}{\partial t} + A\frac{\partial Q}{\partial x} = 0 \qquad (2.26)$$

Where: η = bed elevation, A = a coefficient, Q = sediment flux and x = position along a 1-dimensional continuum (most sediment models use a 2-dimensional version of the Exner equation).

Instantaneous velocity values output from the hydrodynamic model at each mesh node are converted to sediment transport rates by the sediment model. The transport rates at each time step are input into the Exner equation (equation 2.26) for each mesh node as sediment flux values. Any net sediment flux at each node corresponds to either erosion or deposition of sediment and results in a change in the bed elevation (η). Variations in bed level for the duration of each model run are recorded at each node as a time series providing a complete picture of the cumulative seabed evolution.

The conversion from velocities to sediment transport rates is the most crucial and involved aspect of the sediment modelling process. A wide range of *sediment transport formulas* have been suggested for relating depth-averaged velocity or bed shear stress to the resultant sediment transport rate. Parameters relating to sediment characteristics (sediment density, grain size, settling velocity), hydrodynamic aspects (water depth, kinematic viscosity, water density) and various bed roughness metrics (drag coefficient, Nikuradse friction coefficient) are often required as inputs to the formulas. Most of the formulas provide different relationships for the bed-load and suspended-load components of the mobile sediment. These are then combined to produce a total-load transport rate. Section 3.2 of the literature review includes an

investigation into the origins, development and performance of sediment transport formulas in rivers and also discusses the suitability of using such formulations to predict sediment transport within tidal flows.

2.7 Bedforms

The action of currents and waves upon sand on the sea floor can create *bedforms.* These are regular patterns formed from the sand and can often be seen to migrate in areas of tidal asymmetry where either the flood or the ebb tide is stronger. The shape, height, wavelength and migration speeds of bedforms can be used to infer the quantity and direction of *bedload* transport using various empirically-derived formulae.

2.7.1 Tidally-generated bedforms

Tidally-generated bedforms are either *flow-transverse* (ripples, sand-waves etc.) *or flow-parallel* (sand-ribbons, furrows etc.). *Asymmetrical* flow-transverse features often occur in areas of tidal asymmetry and imply a net sediment transport at right-angles to the bedform crests. Figure 2.6 illustrates two typical flow-transverse bedforms found in coastal waters.

(a) Ripple

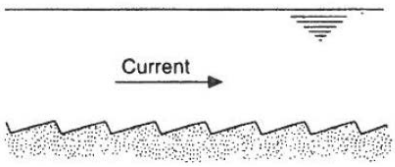

(b) Sandwave

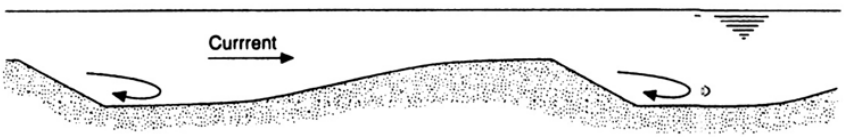

Figure 2.6 Types of bedform (Soulsby, 1997).

The terminology for classifying bedforms is not well defined with definitions and usages for certain classes of bedform varying between different research disciplines.

Here the classification scheme employed by the sediment dynamics research community (Soulsby, 1997) will be adopted. Flow-transverse features are identified as one of three types of bedform of increasing size; *ripples*, *mega-ripples* and *sandwaves*. Bedform height and wavelength are the criteria used for classification.

The three types of bedform exhibit contrasting temporal and migratory behaviours as a consequence of the interaction between a fixed tidal frequency and the varying cross-sectional areas between bedform types. A sand ripple may have a typical trough-to-trough cross-sectional area of $10cm^2$, a mega-ripple of $0.5m^2$ and a sandwave of $200m^2$. It therefore requires the movement of more sand for a larger bedform to migrate the same distance as a smaller bedform (i.e. Migration rate decreases as bedform size increases).

2.7.2 Sandwaves

Sandwaves have wavelengths of 3-20 times the water depth and heights of 0.1-0.3 times the water depth (Van Rijn, 1993) and are usually found in water depths of the order of 30m (Németh et al., 2002). They are considerably larger than ripples and megaripples and typically have wavelengths from tens to hundreds of metres and heights in the region of 3-10m. Tidal asymmetry can lead to asymmetric sand waves caused by a net sediment transport in the direction of the largest velocity (Van Rijn, 1993).

Sandwaves often exhibit migrating mega-ripples superimposed upon them and have been observed migrating at velocities of 0-5m/yr. (Van Rijn, 1993) depending upon their size, sediment characteristics and tidal stream velocities. Storm events can reduce sandwave heights by up to 30% relative to their tidally-generated ‘equilibrium’ heights (Langhorne, 1982).

2.7.3 Quantitative assessment of bedforms

A method for consistently quantifying bedform height, wavelength and asymmetry was proposed by Knaapen (2005). Figure 2.7 shows how simple values are derived from crest and trough positions as portrayed in a 2-dimensional cross-section running perpendicular to the bedform crest. The bedform wavelength is defined as the horizontal distance between the two troughs on opposite sides of the crest. The height

is characterized as the vertical difference between the crest height and a 'baseline' connecting the two troughs:-

$$H = z_c - \frac{z_1 L_2 + z_2 L_1}{L} \tag{2.23}$$

Where: H = bedform height, z_c = crest height, L = horizontal distance between troughs, L_1, L_2 = horizontal distances between troughs and crest, z_1, z_2 = vertical distances between troughs and crest.

The asymmetry is quantified as the difference between the horizontal crest-to-trough distance on either side of the crest scaled by the wavelength (L):-

$$A = \frac{L_2 - L_1}{L} \tag{2.24}$$

Where: A = bedform asymmetry

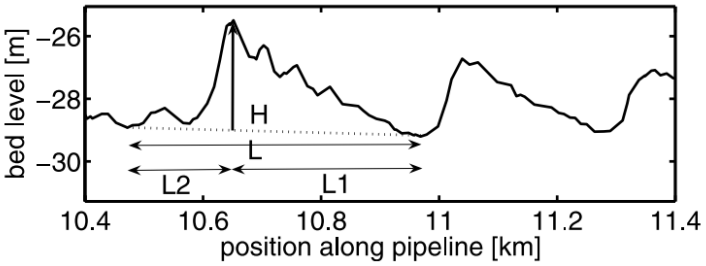

Figure 2.7 Dimensions used to quantify bedform characteristics as rendered in a 2-dimensional cross-section taken perpendicular to the bedform crest (Knaapen, 2005).

2.7.4 Bedform migration rates

Bedform migration rates can be deduced at a site using repeated swath bathymetry or sidescan surveys. These may be performed at short intervals (~1/hr.) across a single tidal cycle to assess the instantaneous response of bedforms to hydrodynamic variations (Bastos et al., 2004). Variations of migration rates across the spring-neap cycle can be balanced by re-surveying at a 14 day period (or any integer multiple) after the initial survey. Repeated measurements of bathymetry can also be taken across much longer time scales (>≈1/yr.) to help infer long-term migration rates (Shaw et al., 2008) and to neutralise the potential effects of seasonality.

The length of time between repeated bathymetry surveys scales with the type of bedform that can be productively investigated. Two bathymetry surveys performed 14 days apart may yield useful information on mega-ripple migration with sufficient crest movement for rates to be observed (i.e. migrations are larger than the measurement error) but not so much movement that individual mega-ripples can't be tracked. The same two surveys may not yield useful information on sandwave migration due to the migration distances being too small (i.e. smaller than the measurement error) across the 14 day period. In the same way, two surveys performed a year apart may yield useful information on sandwave migration rates but no insight into mega-ripple migration (i.e. individual mega-ripples can't be tracked accurately).

Values for bedform migration can be used to calculate bedload transport rates. The volumetric bedload transport rate is related to the bedform height, shape, migration rate and settled sediment porosity by the following equation (Soulsby, 1997):-

$$q_b = a_m \Delta \, V_{mig} \tag{2.25}$$

Where Δ = height of the bedform

V_{mig} = bedform migration rate

a_m = a constant that is the product of:

(1) (1-ε) where ε is the settled sediment porosity

(2) A factor describing the shape of the bedform

$qb =$ bedload volume transported per unit time per unit width [m^2/s]

This relationship assumes that the sand particles roll from the trough of a bedform, over the crest and come to settle in the next trough. In reality sand particles may continue to roll over further crests or be lifted into suspension, leading to bedload transport rate underestimates of up to a factor of 2 (Soulsby, 1997).

3 Literature Review

3.1 Sandbank morphology

3.1.1 Coastal sandbanks

Sandbanks are found on shelf seas and in coastal areas and can be understood as sediment traps that store sand for long periods of time (HR Wallingford, 2001). Sandbank formation requires an abundant sediment supply and sufficiently strong tidal currents to move sediment. Sediment can be supplied by either coastal recession or erosion of the seabed and is transported by both bedload and suspension (Dyer and Huntley, 1999). The fact that sandbanks form in areas where flows are strong enough to move sediment implies that either or both of the following apply during the varying states of tidal flow (HR Wallingford, 2001):-

- That there must be some continual circulation of sand around the sandbank ensuring that it is not more widely dispersed
- That the sandbank is positioned at a point where the flow velocities fall below the critical value for sediment suspension/bedload transport (i.e. The sandbank represents a 'dumping' point where sediment is deposited once the bed shear stresses fall below the critical value).

Sandbanks are often overlaid with bedforms of various types and sizes which can be used to infer the movement of sediment around or along the sandbank. Many sandbanks have become effectively *inactive* (i.e. no mobile sand), as a result of sea-level rise during the postglacial transgression or due to other morphological developments (changes in tidal flows, retreating coastlines etc.). These banks may exhibit bedforms preserved from periods of time when the tidal flows or wave orbitals were sufficiently large to move sand, but are no longer modified or maintained by hydrodynamic processes.

When evaluating a sandbank it is important to determine whether the bank is *active* or *inactive*. This may be obvious from the morphology of the area (i.e. a tidal ebb delta sandbank immediately adjacent to a migrating barrier island inlet is almost certain to be active) and from an assessment of the bathymetry. If further knowledge is required

in ambiguous situations then numerical models can be used to determine whether the bank is likely to be active or not. A hydrodynamic model linked to a sediment dynamics module can be used to assess whether shear stresses at the sandbank surface are sufficient to promote bedload transport or sand suspension.

Many sandbanks appear to be in a semi-stable 'equilibrium' with the local flow regime and recover their prior forms following modification by extreme storm events (HR Wallingford, 2001). It has been estimated that the time scale of sand circulation around sandbanks is of the order of several hundred years (ibid.).

3.1.2 Classification of coastal sandbanks

A classification scheme based upon sandbank origin and development was proposed by Dyer and Huntley (1999) in an attempt to unify the diverging approaches to sandbank behaviour employed by marine geologists and physical oceanographers. An intuitive, generalised framework was presented which can be used to categorise real world sandbanks into a few basic archetypes based upon sandbank size, shape, location and local morphology. The various types and sub-types enable likely behaviours to be predicted and the potential effects of anthropogenic factors upon sandbank morphology/stability to be assessed. Only *type 3* sandbanks, and in particular *type 3A* sandbanks, will be discussed in the main body of this report. A full summary of Dyer and Huntley's classification scheme with descriptions of the various sandbank 'types' can be found in Appendix A.

Type 3 sandbanks are formed at headlands where sediment transported by long shore drift (from one or both sides of the headland) is swept offshore where it accumulates to form a long, linear sandbank. Tidal flows around the headland are a key factor in the formation of type 3 banks. Strong currents are required to move sediment far offshore (along the length of the bank) and to form large eddys in the lee of the headland that play an important role in helping form and maintain the sandbank.

Where a headland erodes very slowly and the sediment is supplied predominantly from one side, type 3A banks, or *banner banks*, may be formed. These extend, protruding from the headland, in a straight line and are typically 5-10km long and 1-2km wide (Berthot and Pattiraratchi, 2005). The formation and maintenance processes are well understood (compared to those relating to other types of

sandbank) allowing numerical models of 3A banks to be validated and enabling the model-based investigation of real world type 3A sandbanks. Banner banks appear to occur more frequently in regions where the water depth increases rapidly away from the coast (HR Wallingford, 2001).

3.1.3 Headland associated linear sandbanks

When propagating tidal flows encounter headlands or islands, velocities increase in magnitude as they pass around what is effectively a 'flow constriction'. If the headland geometry is abrupt enough and the tidal flows are fast enough then *flow separation* will occur downstream from the constriction and *eddys* will be formed in the lee of the headland (Wolanski et al., 1984; Signell and Geyer, 1991). Although these eddys may not be present across all stages of the tide they may be significant enough to significantly affect *residual velocities* (The average velocity across a single tidal cycle at a particular point in the flow).

This dynamic is illustrated in Figure 3.1 which shows the ebb and flood streamlines and the resultant tidal residual at the site of a typical type 3A bank (The Skerries Bank, Start Bay, Southern England). The *ebb* and *flood* phases of the tide relate to the outgoing tide (water levels decreasing) and the incoming tide (water levels increasing) respectively. A tidal phase (flood or ebb) is said to be *dominant* at a particular location if the *residual* velocity is non-zero and has the same direction vector as the tidal-phase. The Skerries Bank is outlined by a dashed line and the point of transition between ebb and flood dominance is shown as a dotted line. It has been consistently observed that, for banner banks, the line of transition from ebb to flood dominance coincides roughly with the lengthwise centre of the bank (Dyer 1986; Bastos, 2004; Berthot and Pattiraratchi, 2005). In the deep channel between the sandbank and the coast the flow is ebb dominant as a result of eddys that recirculate back towards the headland for significant portions of the flood tide. On the seawards side of the bank the flow is strongly flood-dominant due to the increase in flow speed around the headland.

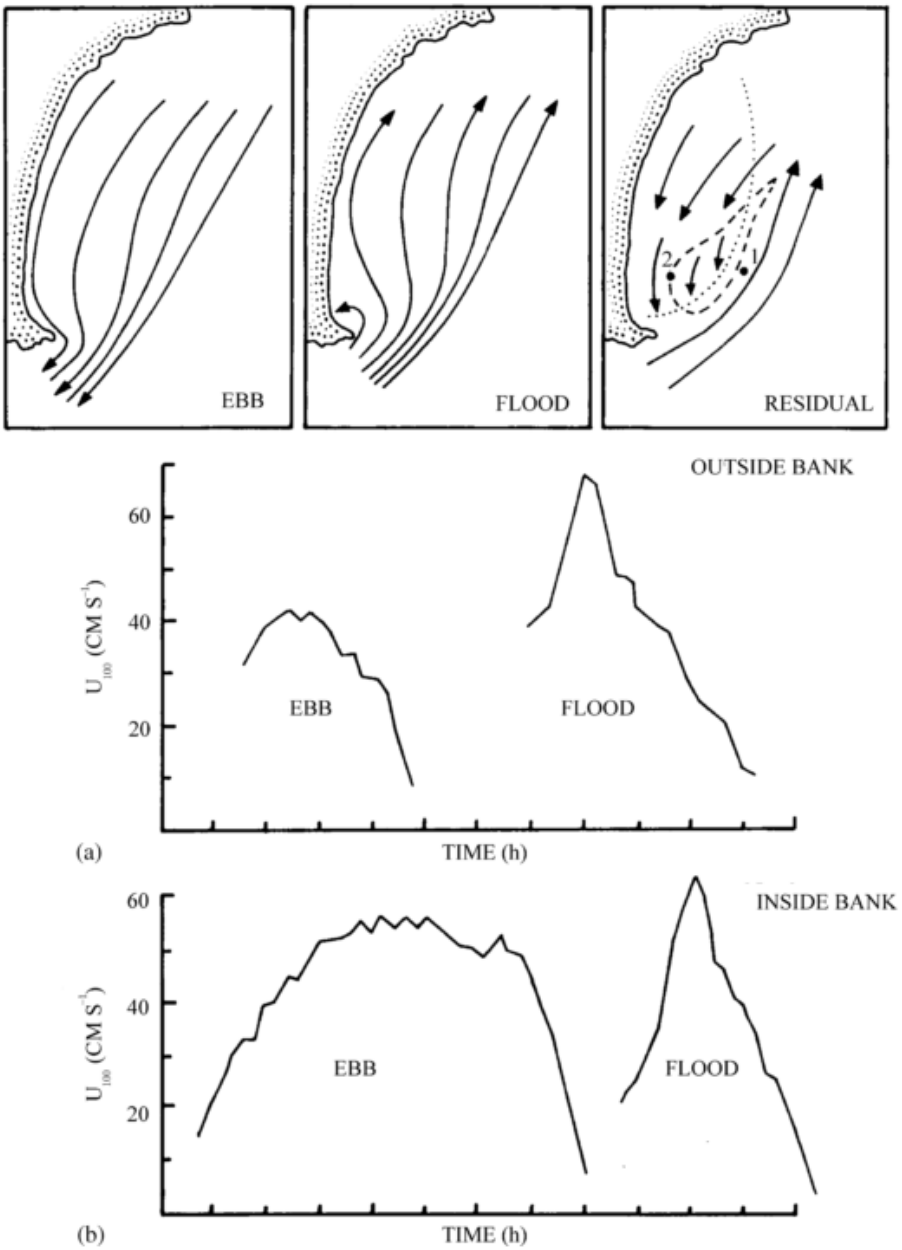

Figure 3.1 The streamlines on flood and ebb tide and the tidal residual around a 3A banner bank (The Skerries Bank, Start Bay, Southern England). The currents measured at positions 1 and 2 outside and inside the bank are included to illustrate how the flow velocities vary across a semi-diurnal tidal cycle (from Dyer, 1986).

The velocity plots for the outside and inside of the bank in Figure 3.1 (a-b) show how the flow magnitudes and directions are different for the two regions. Although the magnitude of the ebb-tide velocities on the inside of the bank do not reach the

maximum values of the flood tide velocities they can be seen to stay at a maximum value for a much larger portion of the tidal cycle than observed on the outside of the bank. It is also significant that the turning of the tide occurs later on the inside of the bank than the outside and that the ebb-tide lasts longer. It can be inferred that the tide is still ebbing on the inside of the bank whilst the outside of the bank has started to flood.

This contrary tidal dominance on either side of a banner bank is the major dynamic responsible for their formation and maintenance. Two sediment transport regimes are typically observed (Bastos, 2002):-

1. An inner zone with net sediment transport towards the headland
2. An outer zone, in which net sediment transport is directed away from the headland and bed shear stresses get smaller with distance from the headland

The line dividing the regions of ebb and flood asymmetry represents a bed shear stress convergence zone (bedload convergence zone) that encourages the accumulation of sand and creation of sandbanks (Bastos, 2002). There are also a number of other flow mechanisms that promote the transport of sediment laterally across the sandbank up to the sand bank crest on both sides (these are discussed in section 3.1.4). Figure 3.2 illustrates a conceptual model of net bedload transport around Portland Bill in the UK. The Shambles Bank is a typical example of the dynamic being discussed; a long, linear sand bank close to a headland with the line denoting transition from ebb to flood dominance running roughly along its centre and away from the headland.

Another typical feature of headland constricted flows is the presence of a *scour zone* close to the headland tip, an example of which is illustrated within the context of Portland Bill in Figure 3.2. Flow velocities and bed shear stresses are at a maximum in this zone and the area is typified by a sediment-free, bedrock seabed that may or may not be actively eroding (depending upon flow velocities and the rock's resistance to erosion).

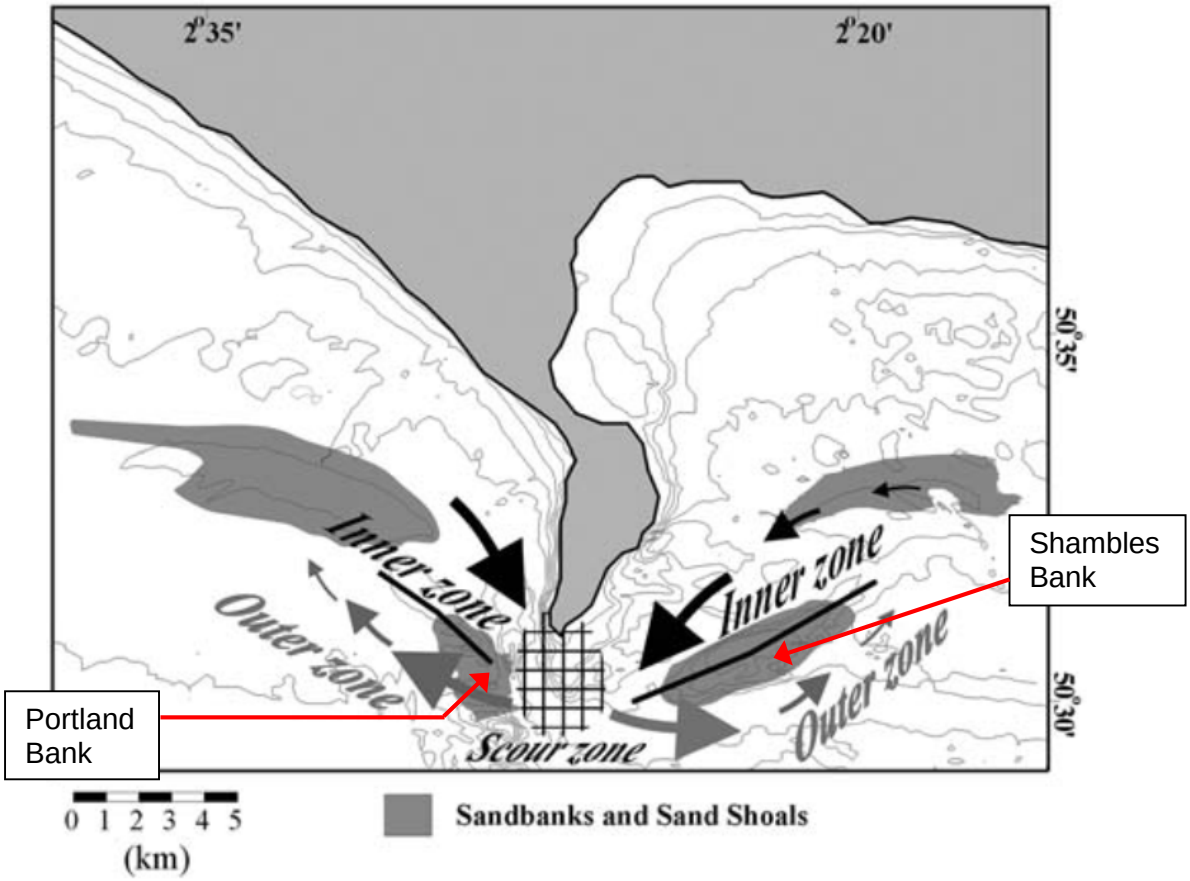

Figure 3.2 Conceptual model of net bedload transport around Portland Bill. Sand transport is characterized by an inner sand mobile zone (black arrows) and an outer sand mobile zone (grey arrows). The scale of the larger arrows represents the direction of increased gradients in bedload transport rates. The boundary between those zones constitutes a *bedload transport convergence zone* (black line). At the tip of the headland, a *scour zone* occurs at the point of maximum erosion (from Bastos, 2003).

3.1.4 Maintenance of type 3A headland associated linear sandbanks

In addition to the contrary flow dominance (and hence contrary sediment transport direction) on either side of a banner bank there are also two other identifiable flow mechanisms that encourage their formation and maintenance. They are, to some extent, related to each other, and are perhaps better described as different conceptual models of the same process that highlight specific elements of the complex and continuous real-world situation. Both promote the movement of sand across and up the bank towards the crest. They are:-

- Pingree's 'tidal stirring' concept
- Helicoidal (secondary) flows

Pingree (1978) drew a parallel between how sand in a cup of water behaves when stirred and how eddys shed by headlands appear to promote formation of sandbanks at the centre of such eddys. When a cup of water with sand in it is stirred the sand moves along the bottom and collects in the middle (due to secondary flows caused by bottom friction). Pingree hypothesised that a similar process may be responsible for the formation and maintenance of many headland associated sand banks due to accumulation of sand at the centre of rotating eddys. Pingree's hypothesis also proposed that the opposite action of Coriolis acceleration on anti-cyclonic and cyclonic eddys shed from protruding headlands results in a variation in resultant sandbank size due to a variation in pressure gradient.

The tidal stirring concept has been subject to a number of modelling based experiments in the past decade (Signell and Harris, 2000; Bastos et al., 2002; Bastos et al. 2004; Neill, 2008). The significance of Coriolis in sandbank size variation has been contested by Signell and Harris (2000) whose results showed little variation in sandbank size between cyclonic and anti-cyclonic eddys. Potential alternatives for the sandbank asymmetry at Portland Bill were proposed including meteorological factors and differences in sediment supply. Neill's (2008) models of tidal flows past idealised headlands and islands suggested that Coriolis could have a significant effect upon sandbank formation, especially when eddys were shed by a headland instead of remaining 'attached'.

Helicoidal cells refer to secondary flows that occur laterally (at right-angles) to the main flow direction as a result of flow curvature (i.e. due to the passage of a tidal flow past a headland or island). Berthot and Pattiraratchi (2005) analysed data collected across a tidal-cycle by a vessel-mounted ADCP making lateral transects across a type 3A banner bank. The data, plotted in Figure 3.3, showed that secondary flows were present during the maximum flood currents with separate rotary cells occurring on both sides of the banner bank. These secondary currents were directed away from the sandbank in the top half of the water column and towards the bank in the bottom region. The secondary currents are small compared to the velocity of the dominant tidal current (typically $U_s < 0.1U_m$; U_s = secondary current and U_m = main current; Engelund, 1974) but the non-linear nature of sediment transport means that small, consistent current increases may contribute significantly to sediment transport.

Any increases in bedload transport due to these rotary flows would promote movement of sand towards the sandbank (due to the bankwards movement close to the seabed) thereby contributing to maintenance. Numerical model runs of the region that both included and inhibited these secondary flows (helicoidal cells) were compared. It was shown that the contribution of the secondary flows to the sediment transport was around 20% of the net sediment transport and that they concentrated sediment towards the sandbank.

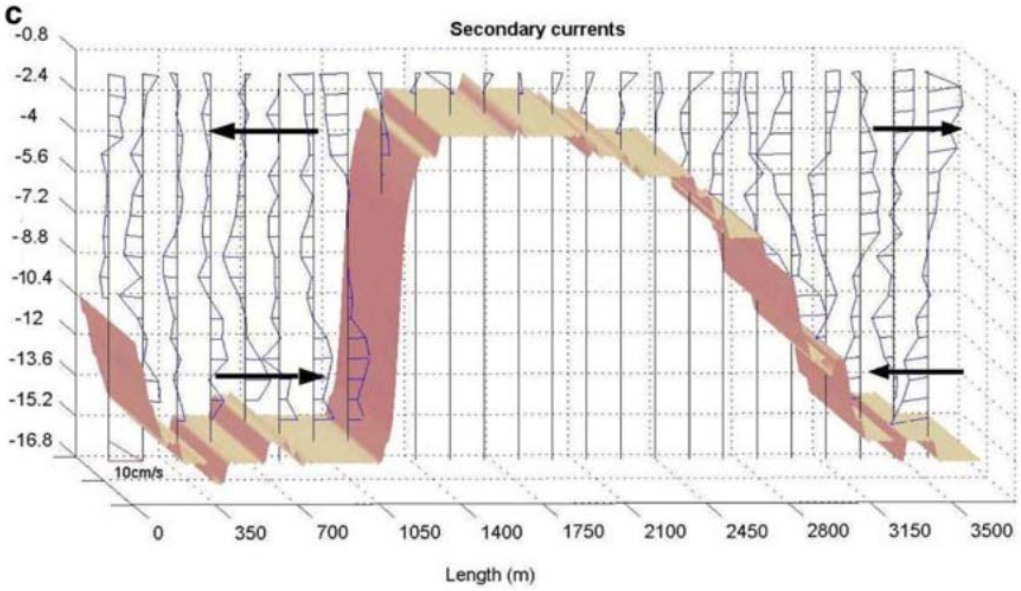

Figure 3.3 Secondary currents measured (ADCP) across the Levillain Shoal, a headland-associated linear sandbank present in the lee of Cape Levillain (Shark Bay, Western Australia). Illustration from Berthot and Pattiraratchi (2005).

3.2 Sediment transport formulas

In this section of the literature review the origin and development of methods for predicting sediment transport rates within rivers are discussed. Multiple comparisons of various sediment transport formulas are then presented and discussed. Difficulties relating to the prediction of transport rates within tidal currents are outlined and the applicability of river-based formulas to coastal waters discussed. Finally the possible criteria and a method for picking sediment transport formula for a particular application are presented.

3.2.1 Prediction of sediment transport rates in rivers

The movement of sediment along rivers and irrigation ditches has been an area of practical interest for millennia with sedimentary problems studied and solved in a number of ancient civilizations (China, Mesopotamia, Egypt; Van Rijn, 1993). The scientific study of sediment movement in the more recent past springs from advances made in hydraulics in 18th Century France. The relationship between fluid flow and sediment movement in France's many large rivers (The Seine, the Rhone, the Loire, etc.) became increasingly relevant for various engineering projects during this period with the impacts of flooding upon banks and piers of particular practical importance (Hager, 2005). The first bed-load type formula was proposed by DuBoys in 1879 which he developed whilst working for the French river service on the river Rhone (ibid.):

$$q_s = \chi\, F(F - F_0) \tag{3.1}$$

Where $F = h\rho i$ and where q_s = volumetric sediment transports rate, h = fluid depth, ρ = density, i = slope, χ = a parameter to be empirically adjusted, and F_o = a limit entrainment force value.

The *entrainment force, F,* is a unit force per square meter of river-bed and DeBoys developed a relationship for calculating the *limit entrainment force, F_o,* as a function of the density and porosity of the sediment in question. This limit entrainment force can be seen to act as a threshold value above which sediment is entrained into the flow. Schoklitsch (1914) developed this idea of a threshold value by deriving an equation for the critical bed-shear stress (i.e. τ_{0cr} ; see section 2.5) for longitudinally sloping beds using a theoretical approach (Van Rijn, 1993). Building on this work Shields (1936) proposed a non-dimensional equivalent of the critical bed-shear stress known as the Shields parameter, θ. When plotted against a *grain Reynolds number*, Re_*, calculated using Yalin's dimensionless grain size, D_* (Yalin, 1972), the shields parameter relationship enables estimation of the threshold of sediment movement to be made for a wide range of grain sizes and flow conditions.

The development of sediment transport formulae in the modern era has been driven by a combination of river-based measurements and flume-based experiments relating to steady, unidirectional flow. Many sediment transport equations have been developed, calibrated and tested using data from both approaches simultaneously.

The difficulties of measuring *actual* sediment transport rates in rivers were gradually overcome using a number of novel technical innovations. In particular a variety of *bed-load samplers* were developed to sample the bed-load transport rates in rivers allowing transport rate comparisons to be made between real-world environments and lab-based experiments where the conditions could be controlled (Van Rijn, 1993).

Progressively, transport formulae were tested and improved with researchers proposing improved forms of the relationships, refining the constants and generating original formulae as data-collection and understanding accumulated. Formulae for calculating suspended sediment transport rates using suspended sediment concentrations (typically represented by a reference concentration C_a at a reference height z_a) were developed a little later than those for bedload (Smith and McLean, 1977; Van Rijn, 1984) due partially to the scarcity of accurate sampling methods. Total-load formulae can be produced by combining bed-load and suspended-load formulations or, alternatively, a single empirical formula derived from flume work or extensive field-studies can be used. Each formula's effective validity range is defined by the range of parameters relating to the data that were used to determine the relationship (i.e. the range of water depths, flow velocities, sediment sizes and water temperatures).

The majority of sediment transport equations are based upon the assumption that transport rates can be related to (i.e. can be predicted by) a dominant variable relating to the fluid flow (Yang, 1996):

$$q_s = A(K - K_c)^B \tag{3.2}$$

Where: q_s = Volumetric sediment transport rate per unit width of channel [m^2/s], K = Dominant variable used to determine transport rate, K_c = Critical value of dominant variable (i.e. sediment threshold of motion), A, B = Parameters relating to sediment and flow characteristics.

DuBoys's approach (Formula 3.1 above; 1879) can be seen to use the water surface slope as the dominant variable. Other choices of dominant variable that have been used to describe and predict sediment transport rates are average flow velocity, water discharge, bed shear stress and stream power.

Yang (1996) uses flume data collected by Guy et. al (1966) to assess the validity of using each of these parameters as the dominant variable in a sediment transport

formula. The possibility for identical values of water discharge or surface slope to relate to different transport rates (Leopold and Maddock, 1953; Yang, 1996) suggests that these are unsuitable predictors for sediment movement. Although both average flow velocity and bed shear stress do correlate well with transport rates the *steepness* of the relationship makes these parameters poor predictors of transport rates as can be seen in Figure 3.4 a-b (Yang, 1996). It is the stream power variable-based approaches that appear to correlate most usefully with sediment transport rate as can be seen in Figure 3.4 c-d with a more linear relationship occurring over a wider range of dominant variable values.

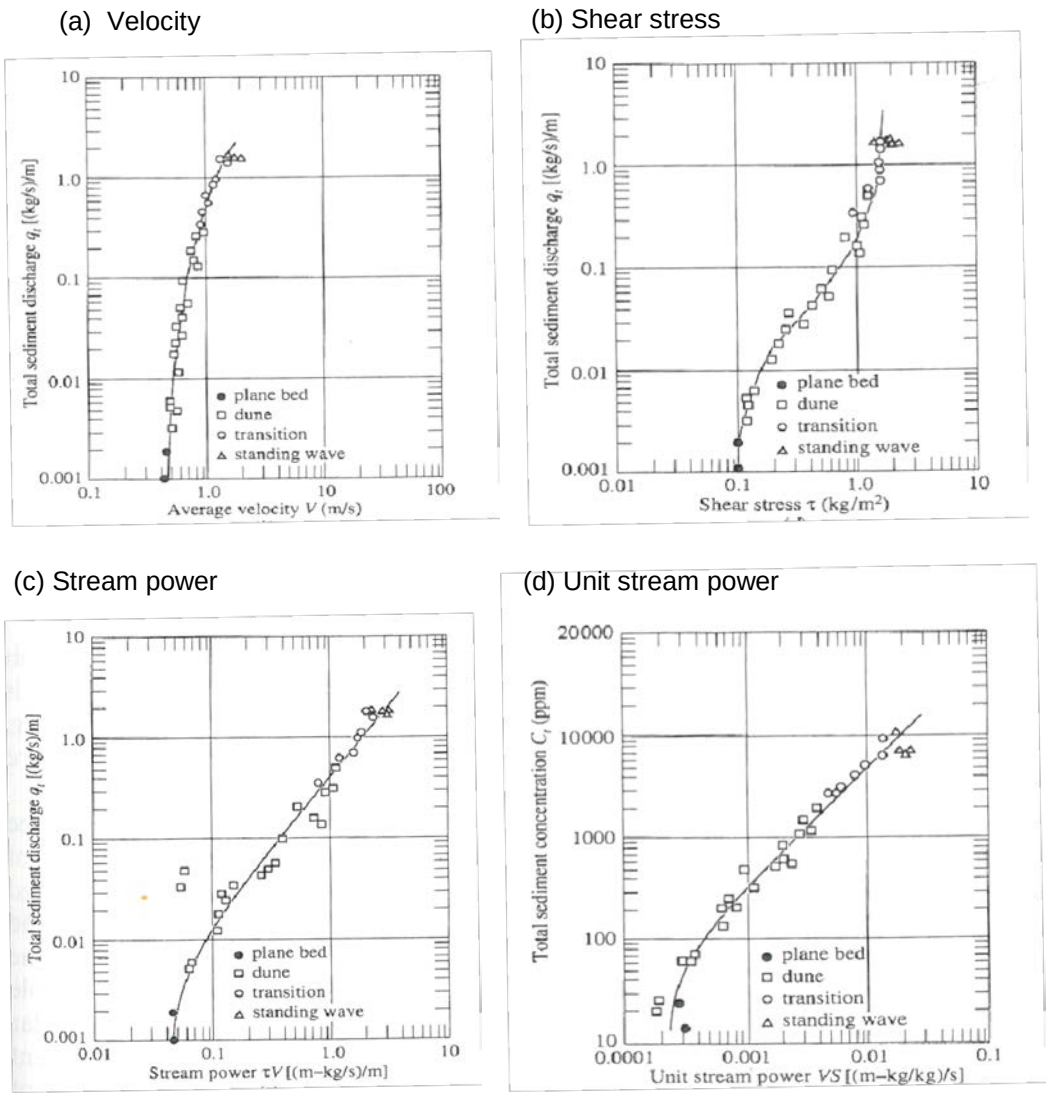

Figure 3.4 Relationship between sediment transport rate and each of 4 dominant variables (Yang, 1996).

Bagnold's original bedload equation (1963) was the first to use a 'stream power' approach to express sediment transport rates. By investigating the relationship between the rate of energy available for transporting sediment (i.e. available power from the flow) and the work done by the flow upon the transported sediment, Bagnold produced the following relationship (Heathershaw, 1981):

$$q_b = \frac{\rho_s}{(\rho_s - \rho)g} \bullet K\omega = \frac{\rho_s}{(\rho_s - \rho)g} \bullet K\rho u_*^3 \qquad (3.3)$$

Where: q_b = volumetric bedload transport, ω = stream power *K* = Constant dependent upon sediment characteristics, u_* = Friction velocity, ρ_s = Sediment density, ρ = Water density.

The stream power, ω, corresponds to the power expended by the flow per unit area of seabed. The equation originally had no threshold of motion criteria but it was shown by Kachel and Sternberg (1971) that the constant *K* is actually dependent upon the excess shear stress above a critical value.

Engelund and Hansen (1972) developed Bagnold's stream power approach to describe total load transport in terms of a friction factor expressed as a drag coefficient (Soulsby, 1997):

$$q_t = \frac{0.04 C_D^{-\frac{3}{2}} \overline{U}^5}{\left[g(s-1)\right]^2 d_{50}} \qquad (3.4)$$

Where: q_t = volumetric total load transport, $\overline{U}$ = Depth-averaged flow speed, d_{50} = median grain size, C_D = drag coefficient, s = Ratio of sediment and water densities.

Like Bagnold's original bedload formula the equation does not have a threshold of motion criteria. The method is informed by the hypothesis that particles move with a speed proportional to the friction velocity, u_* (Sleath, 1984) and was originally derived by considering the energy balance of bedload transport over dunes (Soulsby, 1997).

Ackers and White (1973) also developed a transport formula based upon Bagnold's stream power concept using a non-dimensional approach (Soulsby, 1997):

$$q_t = A\overline{U}d_{35}\left(\frac{\overline{U}}{u_*}\right)^c\left(\frac{F_{AW}-B}{B}\right)^d \tag{3.5}$$

$$F_{AW} = \frac{u_*^c}{\left[g(s-1)d_{35}\right]^{1/2}}\left[\frac{\overline{U}}{2.46\ln(10h/d_{35})}\right]^{(1-c)} \tag{3.6}$$

$$D_* = \left[\frac{g(s-1)}{\nu^2}\right]^{1/3} d_{35} \tag{3.7}$$

Where: $\overline{U}$ = Depth-averaged flow speed, u_* = Friction velocity, d_{35} = grain diameter for which 35% of the grains by mass are finer, *h* = water depth, D_* = Dimensionless grain size, ν = kinematic viscosity of water, *A, B, c, d* = Coefficients calculated as empirically calibrated functions of D_*.

The formulation is based upon an interpolation across non-dimensional grain sizes, D_*, between a fine sediment, bedload transport regime ($D_* \le 1$) and a coarse sediment, suspended load transport regime ($D_* > 60$). This transition regime ($1 < D_* \le 60$) was calibrated using data from 1000 flume experiments predominantly collected in depths of less than 0.4m and for sediment sizes in the range 0.04-4mm (Heathershaw, 1981).

The stream power method was further developed by Yang (1972) who defined the *unit stream power* as the product of the flow velocity and the surface slope. Yang (1996) contrasts Bagnold's emphasis upon available power per unit of river-bed with his own emphasis upon available power per unit weight of fluid (for transportation of sediments). Yang's 1973 formulation developed this relationship between total sediment concentration and unit stream power (Yang, 1996):

$$\log C_t = I + J\log\left(\frac{VS}{w} - \frac{V_{cr}S}{w}\right) \tag{3.8}$$

Where: C_t = sediment concentration, VS = unit stream power (product of flow velocity and surface slope), $V_{cr}S$ = critical unit stream power parameter, *w* = fall velocity of sediment, *I, J* = dimensionless parameters relating to sediment and flow characteristics.

The critical unit stream power parameter, $V_{cr}S$, represents the sedimentary threshold of motion and the coefficients *I* and *J* were determined using a multiple regression analysis for 463 sets of flume data. The resultant transport formula performs very well for these data-sets with a correlation coefficient of 0.971.

Van Rijn (1984) used fundamental physics and empirical results to derive a complete theory of sediment transport in rivers where the total-load is decomposed into bedload and suspended-load components. Each component is determined by a separate formulation using a combination of sediment parameters and the instantaneous difference between the *depth-averaged flow velocity* and the *depth-averaged critical velocity* (Van Rijn, 1984; Soulsby, 1997):

$$q_t = q_b + q_s \tag{3.9}$$

$$q_b = 0.005\ \bar{U}\ h\left\{\frac{\bar{U}-\bar{U}_{cr}}{[(s-1)gd_{50}]^{0.5}}\right\}^{2.4}\left(\frac{d_{50}}{h}\right)^{1.2} \tag{3.10}$$

$$q_s = 0.012\ \bar{U}\ h\left\{\frac{\bar{U}-\bar{U}_{cr}}{[(s-1)gd_{50}]^{0.5}}\right\}^{2.4}\left(\frac{d_{50}}{h}\right)(D_*)^{-0.6} \tag{3.11}$$

Where: q_t, = total load [volumetric transport rate i.e. m^2/s], q_b = bedload, q_s = suspended load, $\bar{U}$, = depth-averaged flow velocity, $\bar{U}_{cr}$ = depth-averaged critical velocity, h = water depth, d_{50} = median grain size, s = the ratio of sediment density to water density, D_* = dimensionless grain size.

The value of the critical velocity, $\overline{U}_{cr}$, is calculated using sediment parameters (d_{50} and d_{90}) and the water depth, *h*. The dimensionless grain size, D_*, needs to be calculated for the suspended load formulation but not for the bedload component. The original, longer method used by Van Rijn (1993) requires calculation of the alluvial friction although the simpler parameterised version presented above does not.

3.2.2 Comparison of sediment transport formulas

Evaluation and inter-comparison of sediment transport formulae typically involves applying the various formulations to large, existing datasets for laboratory flumes and river surveys. The accuracy with which a formulation can predict the measured transport rates in the laboratory and in the field can be ascertained for a range of parameter spaces allowing rankings to be obtained. Many comparisons of sediment transport formulae are available in the literature although the methods of comparison vary and some of the more recently developed formulae are absent from earlier comparisons. The present discussion will outline comparisons performed by White et al. (1975), ASCE (1982), Van Rijn (1984), Voogt et al. (1991) and Yang and Wan (1991) before exploring a number of comparison summaries presented by Yang (1996).

White et al (1975) assessed 8 transport formulas using 1020 laboratory measurements and 260 river measurements. The formulas of Ackers and White (1973) and Engelund-Hansen (1972) performed well with 68% and 63% respectively of predicted values being within a factor of 2 of measured values. The corresponding values for Bagnold (1966) and Einstein (1950) were 22% and 46%.

ASCE (1982) investigated sediment yields in small streams and rated the accuracy of 8 transport formulas of which 5 were total load formulas. These 5 formulas were rated for accuracy in the following order:

1. Yang (1973)
2. Laursen (1958)
3. Ackers and White (1973)
4. Engelund and Hansen (1972)
5. Meyer-Peter and Muller's bed-load formula (1948) combined with Einstein's suspended load formula (1950)

Van Rijn (1984) compared 4 transport formula using 486 sets of river data with sediment sizes within the range 0.1-0.4mm and flow velocities of 0.4-2.4 m/s. Table 3.1 shows the results of the analysis:

Table 3.1 Percentage of predicted values within a factor of 2 of measured values for 4 sediment transport formulas (Van Rijn, 1984).

Transport formula	River data (486 sets)
Van Rijn (1984)	76%
Engelund and Hansen (1972)	64%
Ackers and White (1973)	63%
Yang (1973)	39%

The method of Van Rijn performs particularly well and that of Yang badly with less than 50% predicted values within a factor of 2 of measured values. Van Rijn (1993) concludes that the formula of Yang must have some serious systematic errors for large depths (>1m) as it performs very well when assessed with laboratory and small-depth river data but very badly for larger rivers. The strong results across a range of river depths shown by the other 3 formulas in Table 3.1 suggest that these formulations scale well for predicting sediment transport across a wide range of depths.

The significant variation in the apparent performance of the Yang formula (1973) when compared with the ASCE (1982) and Van Rijn (1984) comparisons can be attributed to the difference in water depths against which the formula were tested. The ASCE data relates to small streams where water depths were predominantly less than 1m. The Van Rijn comparison used river data relating to much larger water depths and to a wider range of depths.

Voogt et al. (1991) carried out extensive flume studies and used the data to compare the transport formulas of Van Rijn (1984), Ackers and White (1973) and Engelund and Hansen (1972). Sediment of 0.2mm and flow speeds of 1-3m/s were used. 120 estuary data were also used to compare the accuracy of transport rates predicted by the formulas in an estuarine setting. Flows of 1-2m/s were observed during data collection and the sediment sizes were between 0.2 and 0.3mm. Table 3.2 displays the results of both the flume and estuary comparisons:

Table 3.2 Percentage of predicted values within a factor of 2 of measured values for 4 sediment transport formulas (Voogt et al., 1991)

Transport formula	Flume data	Estuary data
Van Rijn (1984)	76%	89%
Engelund and Hansen (1972)	68%	33%
Ackers and White (1973)	68%	26%

The Van Rijn formula performs very well for the flume data and exceptionally well for the estuary data (89% of data predicted values within a factor of 2 of measured values). The other two formulas perform well for the flume data but badly for the estuary data.

The ranking of the three formulas in Voogt et al. (1991) matches their corresponding positions in the comparison of Van Rijn (1984). The Van Rijn (ibid.) formula predicts the highest percentage of transport values in each case with the Engelund and Hansen (1972) and Ackers and White (1973) formulas performing roughly as well as each other but with a lower accuracy than Van Rijn. It can also be seen that the flume data comparison from Voogt et al. (1991) produced very similar percentage predictions to the river data from Van Rijn (1984).

Yang and Wan (1991) compared 8 total-load sediment transport formulations for different ranges of sediment concentration (2-50,000 parts per million), Froude number (0.08-4.00) and slope (0.0001-0.0300). Formulas from Einstein (1950), Laursen (1958), Engelund and Hansen (1972), Toffaleti (1968), Colby (1964), Ackers and White (1973) and Yang (1973) were assessed. Two versions of the Ackers and White formula utilising different grain size parameters (d_{35} and d_{50}) were assessed although Yang and Wan (1991) is the only research comparison to include this d_{50} form. All of the other published comparisons presented here refer to the d_{35} formulation of the Ackers-White formula. The comparison used 1,119 sets of laboratory data and 319 sets of river data and employed a basic parameter of comparison termed the *discrepancy ratio*:

$$R = \frac{C_c}{C_m} \tag{3.12}$$

Where: R = discrepancy ratio, C_c = bed-material concentration from a formula, C_m = measured bed-material concentration.

'Bed-material' here refers to the combined bed-load and suspended load with the concentrations given in parts per million by weight. Table 3.3 shows the rankings for the 8 formulations compared in terms of overall accuracy and accuracy when applied to natural rivers:

Table 3.3 Accuracy ranking of 8 sediment transport formula (Yang and Wan, 1991) in terms of overall accuracy and accuracy using only river data.

Ranking	Overall accuracy	Accuracy for natural rivers
1	Yang	Yang
2	Engelund and Hansen	Toffaleti
3	Ackers and White (d_{50})	Einstein
4	Laursen	Ackers and White (d_{50})
5	Ackers and White (d_{35})	Colby
6	Colby	Laursen
7	Einstein	Engelund and Hansen
8	Toffaleti	Ackers and White (d_{35})

Yangs formula performs best in terms of both overall accuracy and accuracy for natural rivers. Interestingly the Toffaleti and Einstein formulas perform badly in terms of overall accuracy (i.e. for flume and river data across all parameter ranges) and well for natural rivers. The Engelund and Hansen formula performs well in terms of overall accuracy but comparatively badly when used to predict concentrations in natural rivers.

The discrepancy between the strong performance of the Yang formula (1973) in the Yang and Wan comparison (1991) and its poor performance in the ASCE (1982) and Van Rijn (1984) comparisons appears to be related to the range of water depths used to evaluate the formulas. Of the 319 sets of river data used by Yang and Wan (1991) 209 relate to water depths of less than 1m and a further 59 sets of data relate to water

depths of 0.33-1.46m. This suggests that the river data used in the Yang and Wan (1991) comparison relates predominantly to water depths of less than 1m and that the Yang formula (1973) therefore performs very well in this range of water depths. It follows that the serious systematic error for larger water depths that Van Rijn (1984) suggests is present in the Yang formula (1973) is not properly tested by the Yang and Wan comparison (1991) due to the range of water depths represented.

Yang (1996) summarises a large number of transport formula comparisons performed between 1955 and 1993. Both direct comparisons of formula using existing data and indirect comparisons via computer simulation are considered. The following two summaries relate to direct comparisons and are the most relevant to this study.

White et al. (1975) and Yang (1976) based their comparisons upon the same ~1250 sets of laboratory and river data. Yang (1996) combines the results from these two sets of research into a single table, reproduced in Table 3.4:

Table 3.4 Percentage of predicted values within a factor of 2 of measured values for 10 sediment transport formula. Percentages are values combined by Yang (1996) using the results of White et al. (1975) and Yang (1976).

Transport formula	Accuracy
Yang (1973)	91%
Shen and Hung (1972)	85%
Ackers and White (1973)	68%
Engelund and Hansen (1972)	63%
Rottner (1959)	56%
Einstein (1950)	46%
Bishop et al. (1965)	39%
Toffaleti	37%
Bagnold	22%
Meyer-Peter and Muller (1948)	10%

The formulas of Yang and Shen-Hung perform particularly well although the Shen-Hung formulation should not be applied to large rivers (Yang, 1996) which suggests it is unsuitable for use in deeper flows. The formulas of Ackers-White and Engelund-

Hansen both perform reasonably well with roughly 2/3 of the measured data predicted within a factor of two.

Yang (1996) also summarises the findings of Alonso (1980) and Alonso et al. (1982) who considered 8 formulas and compared them using 225 flume data and 40 river data that cover a wide range of sediment sizes. Table 3.5 shows the results giving separate accuracy values for river data and two species of flume data:

Table 3.5 Percentage of predicted values within a factor of 2 of measured values for 8 sediment transport formulas from comparisons by Alonso (1980) and Alonso et al. (1982) as presented by Yang (1996).

Transport formula	40 River data	177 Flume data ($D/d \geq 70$)	48 Flume data ($D/d < 70$)
Ackers-White (1973)	88%	73%	90%
Engelund-Hansen (1972)	83%	51%	67%
Laursen (1958)	56%	71%	79%
Meyer-Peter and Muller (1948) combined with Einstein (1950)	59%	42%	67%
Yang (1973)	93%	80%	85%
Bagnold (1966)	32%	21%	46%
Meyer-Peter and Muller (1948)	0%	19%	73%
Yalin (1963)	46%	33%	65%

All of the formulas achieve higher prediction accuracies when flow depths are smaller (i.e. when $D/d < 70$). Taking a typical grain size for medium sand of d_{50} = 0.4mm then D/d = 70 occurs at a flow depth of 2.8cm. When flow depths are larger (i.e. when depths are > 3cm assuming medium sand) the formulas of Yang, Ackers-White and Laursen are still fairly accurate whereas the Bagnold, Meyer-Peter-Muller and Yalin formulas perform very poorly. For the field data the Yang, Ackers-White and Engelund-Hansen formulas all perform very well predicting more than 80% of measured values within a factor of two. The strong performance of the Yang formula (1973) in this comparison relative to the ASCE (1982) and Van Rijn (1984) comparisons appears to be due to the comparatively small flume and river depths in which the data were collected.

3.2.3 Use of sediment transport formulas in tidal currents

Prediction of sediment transport rates to even a moderate degree of accuracy within oscillatory tidal flows is very challenging. No transport formulas have been developed specifically for prediction in tidal currents (Heathershaw, 1981) and it is typical to adapt and apply formulas derived for transport within rivers for use in the sea (Soulsby, 1997). Tidal flows differ significantly in a number of ways to those observed in rivers and modelled in flumes. These differences have implications for the use of river-derived transport formulas within tidal waters and for the wider continental shelf. These differences and their consequences for prediction of transport rates are discussed below.

All river based formulas are based upon steady, uni-directional flow. Tidal flows exhibit oscillatory, bi-directional or even multi-directional flow behaviour including periods of slack water. The slowly changing nature of tidal current magnitudes and flow directions allows them to be modelled as “quasi-steady” within the lower portion of the water column with the exception of periods of slack water (Soulsby, 1997). Consequently the bi-directionality of tidal currents causes only peripheral issues for the adaptation of river-based formulas.

Water depths in estuaries and on the continental shelf are often much larger (i.e. 10-50m) than those observed in all but the largest of rivers. Laboratory-based flume experiments have typically been focussed upon simulating transport for these smaller rivers and the majority of flumes can only simulate flows of <2m. Formulas calibrated and tested against rivers of larger depths have been developed although their effective validity ranges are still small compared to depths typical in coastal waters. An exception is Van Rijn’s formula (1984) that has an effective validity range for depths of 0-20m.

One factor that limits the applicability of river-based transport formulas to the sea is the assumption that water surface slope and bed friction are uniquely related (Soulsby, 1997). Although this principal is axiomatic for modelling constrained channel flows like rivers other methods for calculating bed shear-stresses must be used in the sea.

The influence of surface wave action upon sediment transport can be important in estuarine and coastal settings. Wave orbitals promote increased suspension of

sediment and can produce oscillatory increases in bed shear stresses. In tidal flows heavy wave action may significantly increase transport rates. Many transport formulas have been expanded to include the effects of wave action upon bed shear stresses and resultant transport rates.

There are a number of factors that complicate the measurement of sediment transport rates in coastal waters. Large depths and energetic wave climates make it more difficult to install and retrieve sampling equipment than for river surveys. The bi-directional patterns of sand transport limit the usefulness of bed-load samplers. Measurement of the corresponding hydrodynamic conditions to sediment transport is often problematic in unbounded flows. As a result there are not many large datasets available to test the performance of sediment transport formulas in tidal waters. The comparison by Voogt et al. (1991) using estuarine data is one example of such a comparison (see above) and another is that of Heathershaw (1981).

Heathershaw (1981) used data from a one-year radioactive tracer experiment to assess the performance of 5 sediment transport equations in tidal currents of 5-15m depth. The formulas of Bagnold (1966), Yalin (1963), Einstein (1950), Ackers and White (1973) and Engelund and Hansen (1972) were compared. In shallower water the formulas of Einstein and Engelund-Hansen gave good agreement with measured rates although they both underestimated in deeper water. Bagnold's formula was least sensitive to changes in roughness length and sediment size. The formulas of Ackers-White and Engelund-Hansen were concluded to be the least sensitive to changes in depth.

Soulsby (1997) presents an overview of sediment transport formulas that are most suitable for making transport rate predictions in tidal waters. Ease of application, parameter validity ranges and common practice are all considered. Soulsby concludes that the most widely used and best suited formulas for use in the sea are the formulas of Engelund and Hansen (1972), Ackers and White (1973) and that of Van Rijn (1984).

3.2.4 Criteria for picking sediment transport formula

The question of choosing which sediment transport formula is most suitable for a particular application is discussed by Sleath (1982), Yang (1996) and Soulsby (1997).

The most useful treatment is given by Yang who presents a detailed procedure for picking a formula based upon the relevant flow and sediment parameters. The following points from Yang are the most relevant for this project:

1. If more than one formula can be used, calculate the rate of sediment transport with these viable formulas and compare the results

2. Use Yang's (1973) formula for sand transport in laboratory flumes and natural rivers

3. Use Ackers and White's or Engelund and Hansen's formula for subcritical flow condition in the lower flow regime

4. Select a formula that is most accurate under the given range of flow and sediment conditions

All sediment transport formula involve empirically calibrated coefficients. For any given application the use of a formula calibrated under similar conditions will be most likely to perform well. The many comparisons of transport formula discussed in section 3.2.2 also provide a useful guide for picking the most accurate and suitable formulas for any given application. A final consideration when picking a transport formulation is to consider which formula are most widely used for similar studies in industry and academia.

3.2.5 Summary

The most accurate formulations predict real-world transport rates for rivers within a factor of 2 for ~70% of samples (Soulsby; 1997). In the sea accuracy is reduced to a factor of 5 for ~70% of samples due to the increased complexity of bi-directional tidal currents and numerous other factors such as the inability to measure transport rates accurately. Margins of error are very large when compared to other branches of science and engineering due to the interaction of a large number of processes that are not sufficiently understood and the strongly non-linear, potentially chaotic nature of these processes (ibid.). Accuracy rates can be improved significantly by calibrating the formula to match (i.e. 'tuning' the sediment model using site-specific measurements) although, in practice, this is an involved and logistically complex process.

3.3 Sediment dynamics and tidal stream turbines

Little academic work has been published relating specifically to the impact of TEC array installation upon sediment dynamics. The following two papers share the same lead author and attempt to model how array installation affects tidal stream velocities and, consequently, the movement of sediment.

3.3.1 Existing research

Neill et al. (2009) created a 1D morphological model representing a 155km lengthwise reach of the Bristol Channel with a 3.2km grid-spacing. The model consisted of hydrodynamic, sediment transport and bed level change components and was elevation driven using the M_2, S_2 and M_4 tidal constituents (extracted from an existing 3D model of the Irish Sea). A 250MW TEC array consisting of 168 Seagen-equivalent devices was represented as an energy extraction term proportional to the flow velocity squared (analogous to a bottom- friction-type term). The array covered a 1.2km by 7.6km area which relates to 3 model grid cells. Three sets of model runs were made with the array located at three different locations exhibiting tidal symmetry (both bedload convergent and divergent zones) and tidal asymmetry. The model was run for one lunar month (29.5 days) and bed level changes resulting from the variation in array location were compared with each other and matched against a non-array simulation for the same time-period.

Magnitudes of bed-level change were dampened by the presence of the TEC array at each of the three locations regardless of the tidal regime present (i.e. a general reduction in tidal velocities must lead to a reduction in net sediment transport). It was also shown that energy extracted from regions of strong tidal asymmetry led to a 20% increase in the magnitude of bed-level changes (when averaged over the length of the model) compared to the tidal symmetry cases. The study suggests that TEC arrays located in sites exhibiting a strong tidal asymmetry will have a much larger impact upon the long-term sediment dynamics of a region than those located in areas of tidal symmetry.

Neill et al. (2012) modelled the impact that large-scale TEC array installation would have on the dynamics of headland sandbanks using the 3D POLCOMS model (which

consists of hydrodynamic, total load sediment transport and bed-level change modules).

The effects of TEC operation upon sandbank formation close to an idealised headland were explored in a domain comprising a channel of 60km by 50km, a constant depth of 50m and a symmetrical headland 15km long and 3km wide. The horizontal grid-spacing was 500m and the model was driven at the open boundary with a normal current velocity amplitude of 1m/s and a period equivalent to the M_2 semi-diurnal tidal constituent. A parameterised 288 MW TEC array was included in the model in the region of maximum tidal stream velocities close to the headland tip. The formation of sandbanks from a uniform flat bathymetry (by the large eddys generated by strong tidal flows past the headland) was compared for the non-extraction and energy-extraction cases.

A reduction in the magnitude of deposition at the centre of the sandbanks of around 30% was observed in the energy-extraction case (when compared with the baseline non-extraction case). It was concluded that the maintenance of headland associated sand banks could be significantly impacted by an array located close to the headland tip and that it is important that TEC array developers assess such impacts with caution.

Neill et al. (2012) used the same numerical modelling framework (3D POLCOMS model) to conduct a real-world case study relating to energy extraction in the Alderney Race (a strait of water between mainland France and the island of Alderney). The South Banks are a large headland associated sandbank located on the Alderney side of the strait and their maintenance could be impacted by the large-scale exploitation of the adjacent tidal streams. The bathymetry was digitised from Admiralty Charts and interpolated to a model grid with a spacing of 150m. The model boundary conditions were extracted from a larger model of the European Shelf and the model run lasted for one spring-neap cycle. A parameterised 300MW array was located in two different regions of the strait for two different model runs and the resultant bed-level changes were compared with a baseline non-extraction model run. The Soulsby-Van Rijn total-load sediment transport formulae were used to convert the depth-averaged velocities to sediment transport rates (see sections 2.6 and 6.3).

For the baseline case a deposition of around 0.05m at the centre of the South Banks was observed over a spring-neap cycle. When energy-extraction was applied the

magnitude of velocity averaged across the model run period at the extraction sites was reduced by around 0.05m/s as shown in Figure 3.5. Velocity reductions were also observed up to 10km away from the arrays and there was a region of considerable velocity increase between the array and the headland for the T47 case as can be seen in Figure 3.5(b). Maximum changes in sediment transport (and hence bed-level change) were observed close to the headland tip regardless of the array location although observations of sediment transport must be understood in the context of sediment supply (there is a limited sediment supply in the headland region). The most important observation relates to an approximate 10% difference in the simulated bed-level change in the region of the sediment-rich South Banks when compared with the baseline case. For energy-extraction around 0.002m of erosion was observed over the South Banks when compared with the baseline case with a corresponding region of deposition located approximately 1km to the North-East. This suggests that array installation in the Alderney Race could impact the South Banks maintenance and potentially alter the long-term morphology of the sandbank.

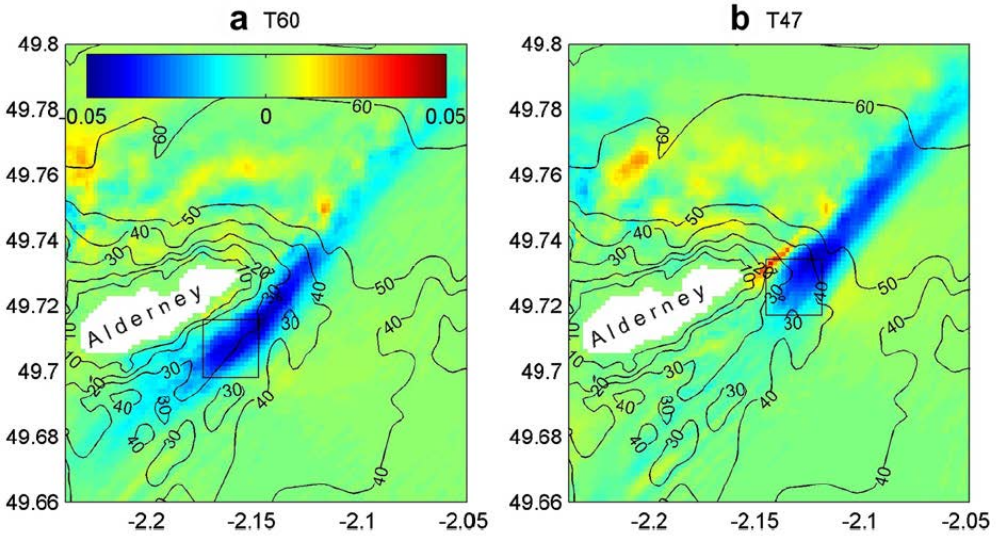

Figure 3.5 Change in velocity magnitude (m/s) due to energy extraction, averaged over a spring-neap cycle. Boxes show the limits of the TEC array for the two locations (T60 and T47). Contours are water depths (m) relative to mean sea level.

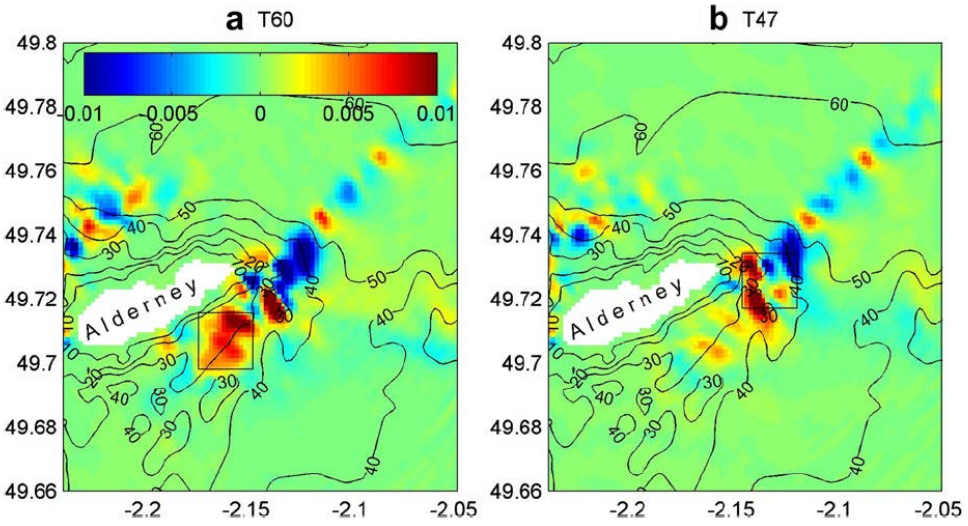

Figure 3.6 Change in bed level (m) due to energy extraction after a spring-neap cycle. Boxes show the limits of the TEC array for the two locations. Contours are water depth (m) relative to mean sea level (Neill et al. 2012).

3.3.2 Evaluation of existing research

The research presented in Neill et al. (2009) and Neill et al. (2012) constitutes the only academic work currently published relating specifically to the effect of TEC array installation upon sediment dynamics. It represents a useful and pragmatic exploration of the topic but is limited by the available data (i.e. bathymetry digitised from Admiralty charts), the relative simplicity of the methods used and the time-scales of the model.

The 1D model of Neill et al. (2009) is unable to capture cross-channel variations in tidal asymmetry, assumes an infinite source of sediment and was driven using a limited number of tidal constituents. Spatial questions relating to flow acceleration around arrays and any related erosion are also not addressed due to the 1-dimensional approach. The suggestion that arrays located in regions of tidal asymmetry will have a much larger impact upon long term sediment dynamics is particularly interesting and potentially very useful. This relationship between asymmetry and sedimentary impact makes intuitive sense and could provide a useful criterion for developers keen to minimise impact if corroborated by further research.

The 3D model used for Neill et al. (2012) did not include components for modelling wind waves and wind-driven currents, was only validated for current magnitudes

against tidal diamonds (no ADCP data was available) and was not setup to include feedback between the hydrodynamic module and a continuously changing bathymetry (which limited the model to runtimes of <30 days). The work described in Neill et al. (2012) was only intended as a 'stepping-stone' for more detailed modelling studies and number of extra model features were suggested that would improve the validity of future studies. The inclusion of wind effects on sediment transport and the continual updating of the bathymetry were both mentioned as significant factors. The authors also specifically emphasised the importance of improved methods for array parameterisation involving techniques such as actuator disc theory or blade element momentum theory.

In the absence of sedimentary data the authors chose a typical sediment size for medium sand (d_{50} = *0.3mm*) for the sediment model. Considering the very high velocities observed over the South banks (> 3m/s) and the measured real-world grains sizes ($d_{50} \approx$ 1.1mm; see section 5.4) the maximum erosions and depositions for the baseline model appear to be very small (<5cm over a spring-neap cycle). Further investigation shows that there is a major error in the calculation of the critical velocity, u_{cr} (see section 2.5). A value of u_{cr} = *1.07 m/s* is quoted whereas the actual u_{cr} for sediment of d_{50} = *0.3mm* in water of 50m depth (calculated using the Soulsby-Van-Rijn formula for critical velocity; section 6.3) is much smaller at u_{cr} = *0.47 m/s.* The accidental use of a natural logarithm (*ln*) instead of a logarithm base 10 (log_{10}) in equation 6.4 (section 6.3) accounts for the error precisely (assuming d_{90} = *0.6mm*). This erroneously high critical velocity means that the sediment transport rates calculated in Neill et al. (2012) must be significant underestimates. Extracting a number of time series over the South banks from the numerical model developed for this study (see chapter 6) and calculating net transport rates with the two values of u_{cr} suggests that a value of u_{cr} = *1.07m/s* leads to cumulative underestimates of net sediment transport by a factor of 2-6.

4 Background to Case Study and Available Data

The island of Alderney is situated 15km West of the North-Western tip of the Cherbourg Peninsula within the larger context of the English Channel (Figure 4.1). Tidal ranges within the vicinity of the Channel Islands are significant (up to 6m) and very large tidal stream velocities are induced by the ebb and flood of the tide. The stretch of water between Alderney and the Cherbourg Peninsula is known as the Alderney Race. Tidal velocities through the Race are particularly large with maximums occurring on the ebb tide as the ebbing water curves around the tip of the peninsula through the Race, as can be seen in Figure 4.1.

4.1 Alderney Race

Currents in the Race of Alderney, adjacent to the South Banks (AWAC in T61: see Figure 7.), flood North-East to East-North-East (45° to 60°) and ebb South-West to West-South-West (225° to 250°). Current magnitudes are larger during the spring tides (~3.0m/s to 3.4m/s) with smaller values observed during neap tides (~1.5m/s to 2.5m/s).

The tide in the Race is ebb-dominant with larger current magnitudes occurring over the shorter ebb-tide. The difference between maximum ebb and flood current velocities is augmented at spring tides (ebb_{max} ≈ 1.0m/s larger than $flood_{max}$) and minimised at neaps (ebb_{max} ≈ 0.25m/s larger than $flood_{max}$).

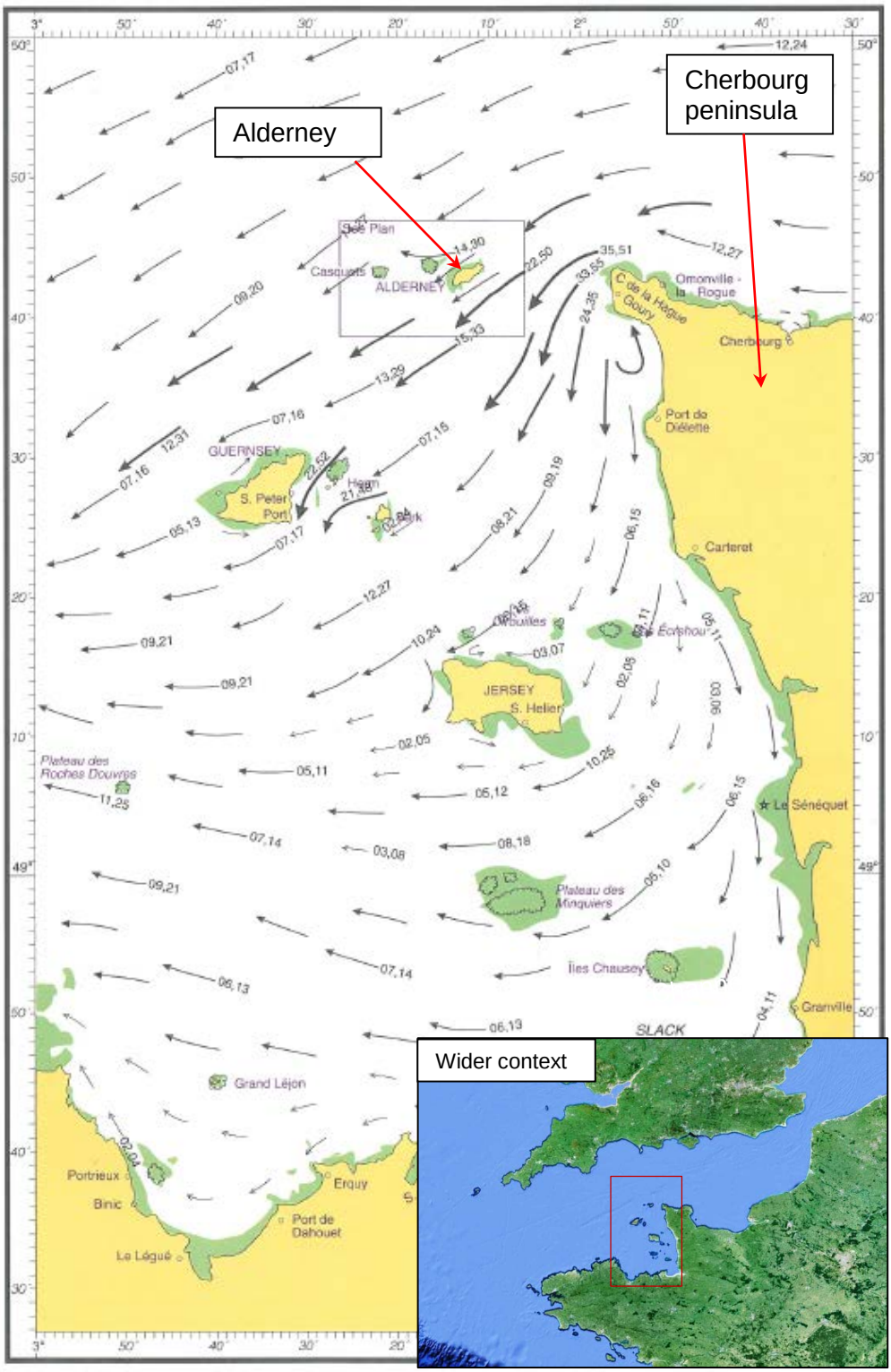

Figure 4.1 Tidal stream atlas for the Channel Islands at 1 hour after High Water at Dover (Admiralty Tidal Stream Atlas). The arrows represent the tidal stream velocities at this point in the tidal cycle and relate to the ebb tide. Larger context shown in inset.

4.2 The South Banks

The South Banks are a ~7.5km long, ~1.5km wide submarine sandbank located to the South of Alderney. Figure 4.2 shows where the South Banks are situated relative to Alderney. The banks extend out from the littoral zone to depths of over 40m and exhibit a maximum height above the surrounding bedrock strata of ~25m.

Significant wave heights adjacent to the sandbank (AWAC in T61) range from 0.25m to 3.7m and possess wave periods of 2.0s to 7.8s that are typical of swell. Mean wave directions are predominantly between 225° and 270° although extreme weather events can modify the average wave direction dramatically and consistently for long periods of time (i.e. storm scale events ~2-5 days).

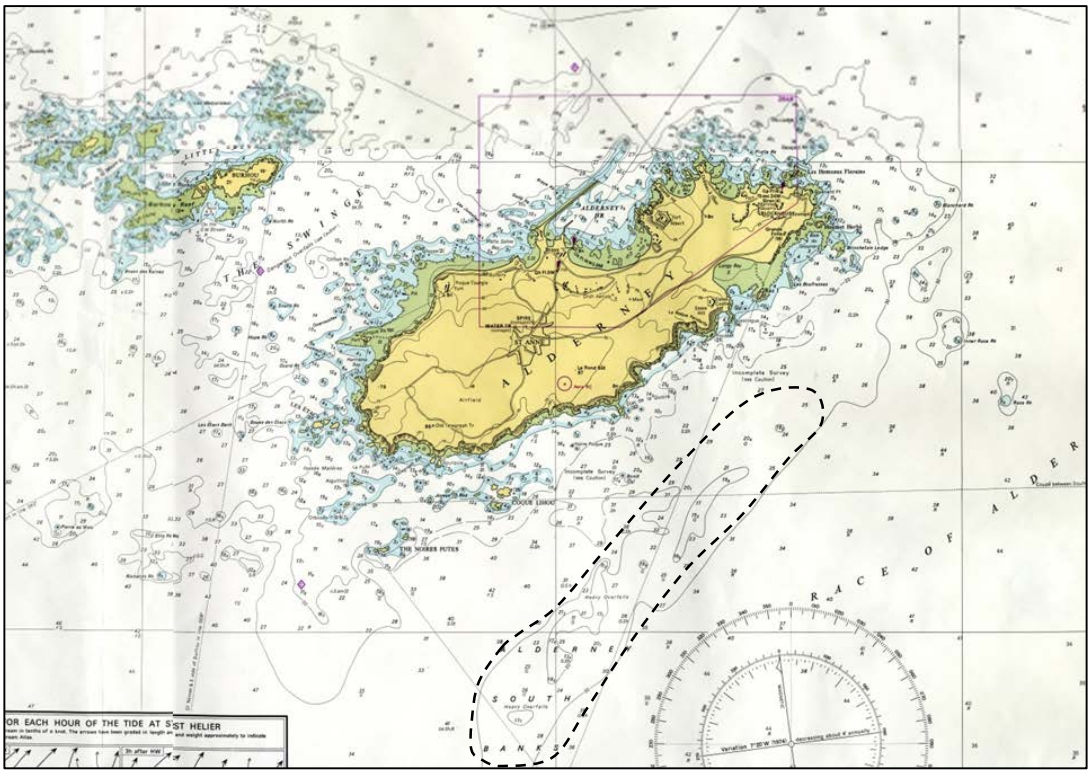

Figure 4.2 Admiralty Chart of Alderney and the Alderney South Banks sandbank (dotted line) located to the South of the island.

4.3 Available data

Table 4.1 shows the data used for this study. Four sets of bathymetry data were obtained to generate meshes for the numerical model. The General Bathymetric Chart of the Oceans (GEBCO) is a publicly available bathymetric grid with a 1-minute resolution. An existing 90-m bathymetric grid covering the extent of the English Channel was obtained privately from Tcarta Marine. High-resolution multi-swath bathymetry data (horizontal resolution = 1m) for the region of the South Banks was obtained from recently performed surveys in the region by Osiris Projects and Seastar Survey. The Alderney Commission for Renewable Energy have divided the region into a number of rectangular development blocks which are referred to as *T-blocks.* This spatial division of the region has informed the data-collection programmes and provides a useful grid system for this research.

Acoustic Current Doppler Profiler (ADCP) datasets collected in the vicinity of the South Banks were obtained from Osiris Projects for the purposes of model calibration and validation. The data consists of current and wave data collected during a one-month deployment at each of 5 locations (see Figure 7). Current data from a tidal diamond in the race (Admiralty tidal diamond: 2669E) were used in addition to the ADCP data for model validation.

Sediment grain size distributions at 11 locations along the South Banks were available from grab samples collected during a sedimentary survey performed by Seastar Survey. These were obtained to inform the morphological study and to determine grain size parameters for the sediment model.

Tidal elevation data relating to 14 ports were obtained from the relevant British and French organisations (NTSLF and REFMAR respectively). Values for tidal elevation are logged periodically (Δ15 minutes in UK and Δ10 minutes in France) and were checked for consistency and completeness.

Table 4.1: Table of available data showing corresponding data sources, spatial coverage, date of collection and intended use.

Data type	Data source	Coverage/location	Date of collection	Purpose
Bathymetry	Osiris Projects	Interconnector routes and T75, T74 & T61 T-blocks	11/04/2009 - 20/05/2009	Model construction
Bathymetry	Seastar Survey	South Banks: full extent	11/12/2010 - 01/02/2011	Morphological study/ model construction
Bathymetry	GEBCO	World bathymetry atlas: low resolution	NA	Model construction
Bathymetry	Tcarta Marine	English Channel	NA	Model construction
ADCP	Osiris Projects	1 ADCP placement: T74	01/05/09 - 04/06/09	Model validation
ADCP	Osiris Projects	4 ADCP placements: 2 in T75 & 2 in T61	17/06/09 - 27/07/09	Model validation
Tidal diamond	Admiralty charts	Tidal diamond 2669E: Alderney Race	NA	Model validation
Sediment grab data	Seastar Survey	11 sediment grabs collected lengthwise along sandbank	11/05/2011	Morphological study/ sediment model
Tidal elevation data	REFMAR	Elevation time series collected at 5 ports	2000 - present day	Model validation
Tidal elevation data	NTSLF	Elevation time series collected at 9 ports	2000 - present day	Model validation

5 Morphological Analysis

5.1 Morphological regime

The Alderney South Banks are a *Type 3A 'banner' sandbank* as determined using the classification system proposed by Dyer and Huntley (1999). Banner banks typically take the form of a straight line protruding from a coastal headland into deep water and are a consequence of the way in which tidal flows behave downstream from the headland. As the ebb tidal flows pass to the South of Alderney large, clockwise eddys are shed by the island tip and propagate along the line of the sandbank. These eddys are strong enough and occur for long enough periods of the tidal cycle for the region between the sandbank and the island to exhibit flood-dominance. A line of transition between zones of opposite tidal dominance lies centrally along the length of the sandbank and it is the interaction between these two contrary zones that helps to form and maintain the bank. On the South-Easterly side of the bank the tidal flows are ebb-dominant and sediment transport is predominantly *away* from the tip of Alderney. On the North-Westerly side flows are flood-dominant and sediment is transported along the length of the bank *towards* Alderney. In this way sand is continually circulated clockwise around the South Banks. The contrary sediment transport regimes converge along the bank crest creating a *bedload transport convergence zone* that promotes sediment deposition and vertical sandbank growth. This accumulation of sand is also encouraged by flow mechanisms that transport sediment laterally *across* the sandbank, depositing it at the crest and leading to cumulative increases in sandbank height.

The South Banks possess a complex and extremely active morphology due to the unusually strong tidal currents (e.g. >2.5m/s) that pass through the Alderney Race. The bank supports an interlocking network of large, migrating sandwaves and sand-ridges with superimposed mega-ripples. Significant volumes of sand are circulated around the sandbank and very high sandwave migration rates of up to 70m in a 50 day period were observed along the ebb-dominant South-Eastern flank of the bank. There is a discernible crest passing along the length of the sandbank although it is obscured and complicated by the complex interactions between sandwaves migrating in opposite directions along opposite sides of the bank.

Analysis of the South banks bathymetry suggests that the sandbank has a volume of ~0.15km^3. This value was estimated by interpolating the surrounding bedrock bathymetry beneath the sandbank and calculating the spatial difference between the bedrock layer and the sandbank bathymetry.

5.2 Sediment transport pathways

Potential sediment transport pathways around the South Banks are shown in Figure 5.1, and were inferred using sandwave asymmetries and orientations. The repeated surveying of areas of the sandbank also allowed sandwave migration rates and directions to be obtained. This information confirmed our sediment transport hypotheses and informs the morphological regime outlined in Figure 5.1.

Sandwave migration rates on the ebb-dominant, South-Easterly flank of the sandbank decrease progressively along the length of the bank. This is related to a consistent increase in sandwave height (and cross-sectional area) but is probably also indicative of a progressive decrease in sediment transport rates with distance from the North-Easterly tip. On the flood-dominant, North-Western flank of the bank a similar dynamic is observed with higher sandwave migration rates observed nearer to the North-Easterly tip. The South Banks appear to be maintained by sand transported along a well-defined mega-ripple field leading from the North-East. Even so, it is not clear from the available data whether there is sediment input to the sandbank from the littoral zone or whether the banks more closely resemble a closed system continually recirculating the same material. It is possible that sand is supplied from an active scour zone at the tip of the island where maximum bed shear stresses occur (Bastos, 2003) or from the wider sea-bed to the North-East of the island. A lack of historical surveys over the bank means that it is unclear whether the sandbanks are currently growing in length, width or height or migrating steadily in a particular direction.

5.3 Sediment transport rates

Where sandwave migration distances can be accurately ascertained (i.e. migration > ~10m) minimum bedload transport rates were calculated. Using the formulation for *volumetric bedload transport rate,* q_b, from Soulsby (1997), and averaging across multiple consecutive sandwaves, values for q_b were obtained for 4 areas along the Southern-Eastern flank of the bank (see Table 7.4 and Figure 7.13 for the 4 migration

areas). Values for q_b were between 0.74-1.15 x10^{-5} m^2/s which corresponds to daily rates of 0.64-0.99 m^2/day with an average of q_b = 0.8 m^2/day (These values are likely to be underestimates by up to a factor of 2 due to grain roll-over: Soulsby; 1997). Although m^2/s is the most commonly used unit of volumetric transport rate, we use the daily rate, m^2/day, for the remainder of this report as the values are more intuitive physically. The total-load transport rate, q_t, is the combination of the bedload transport rate, q_b, and suspended-load transport rate, q_s. Ratios of bedload transport to suspended transport will vary depending upon flow conditions and will also depend upon wave activity over the sandbanks. A guide-value can be inferred from the Soulsby - Van Rijn total load formula (Soulsby; 1997) where the suspended load transport values are larger than the bedload values by a factor of ~2.7 (using values of h=30m, d_{50}=0.0011m, d_{90}=0.0023m and $\upsilon = 1.2 \times 10^{-6}$).

Applying the above relationships to the four q_b values we can propose a rough guideline for total-load transport rates of q_t = 3.23-5.00 m^2/day with an average of q_t = 4.0 m^2/day (where calculated q_b values are underestimates by a factor of 1.5 and $q_s = 2.7q_b$).

5.4 Sediment grain size and spatial variation

A sedimentary survey of the South Banks in May 2011 collected 11 sediment grab samples covering the length of the bank. A particle size analysis yielded d_{50} values (median grain size) of 0.98-2.39mm and corresponding d_{90} values of 1.90-7.00mm. Figure 5.2 shows the spatial variation in grain size across the sandbank. These values are characterised as *Very coarse sand* (1-2mm) with the most South-Westerly reading corresponding to Gravel Granules (2-4mm).

There is a large variation in grain size along the length of the bank with the largest values at the South-Westerly tip. These values decrease gradually along the length of the bank towards the centre and then remain fairly constant up to the North-Eastern end. Lateral-variation of grain size over sandbanks has been investigated in the literature (Roos et al.; 2004) but mechanisms explaining lengthwise variation have not yet been proposed. The variation is likely to occur as a result of a spatial-sorting effect whereby different grain sizes sit in a different spatial equilibrium with the surrounding hydrodynamic regime.

5.5 Sensitivity of the South Banks to hydrodynamic variation

Headland associated linear sandbanks represent a balanced equilibrium between mobile sand and the surrounding high-energy flow regime. At the South Banks the circulation of sand represents a consistent clockwise pathway of the residual sediment transport around the bank as can be seen in Figure 5.1. Increases or decreases to the *magnitudes* of the residual sediment transport may modify the shape of the sandbank with newly created sediment convergence zones and subsequent modifications to the sandbank shape. Although modification of just the residual *magnitudes* could alter the sandbanks equilibrium profile it would seem that a *reversal* in the sediment transport residual *direction* at any point on the bank could have a very significant impact upon the morphology. If the sand circulation was reduced dramatically or even *reversed* at any point along either flank of the bank then the long-term equilibrium of the bank would be compromised.

A total reversal in the residual transport at a particular location would require a large change in the ambient hydrodynamics and is unlikely. Having said this, the important role of the propagating eddy shed by the headland tip is clear from the research (Neill et al. 2008; Bastos; 2003). The strength, propagation direction and life-time of the eddy could be altered significantly by localised changes in the hydrodynamic regime in the region where the eddy forms. In this way localised changes in the flow regime could have a wider impact upon sand movement around the bank.

Within the context of energy extraction it would seem that the potential for asymmetrical modifications to the flow regime, and hence to the sedimentary regime, is high. Areas of flow-deceleration downstream from tidal device arrays will only occur on one phase of the tidal cycle (either flood or ebb). For this study the South Banks will experience relative flow deceleration from the modelled arrays on the ebb-tide predominantly. Flow acceleration *around* arrays may also have an important impact. Although acceleration effects around arrays are typically smaller than deceleration effects downstream of arrays, they may be induced in the region of the South Banks on both the ebb and flood tides thereby increasing the impact of such acceleration effects.

The comparative impacts of these various factors upon the South Banks are explored in the modelling phase of the study, discussed in sections 6-8. In particular, changes

in the development of the eddys that are shed from the headland, and modifications to the sediment transport residual over the South Banks, are considered.

5.6 Summary

The South Banks possess a complex and extremely active morphology. Significant volumes of sand are circulated around the sandbank and very high sandwave migration rates of up to 70m in a 50 day period were observed in one part of the Bank. It is possible that sand is supplied to the Banks from an active scour zone at the tip of the island, or from the wider sea-bed to the North-East of the island. To directly measure long term rates and directions of sediment transport within and around the Banks would require multiple bathymetric surveys over a period of months or years and this data is not presently available. Nevertheless, it is clear from depth soundings on historic charts that the Banks as a whole have been maintained in a quasi-equilibrium state for many decades, if not centuries. While it is not clear whether there is a sediment supply to the Banks, available survey data indicate net clockwise circulation of sediment around the centreline, which acts to maintain the Banks. Therefore changes to this important process caused by changes to the wider flow regime have the potential to affect the long-term stability of the Banks.

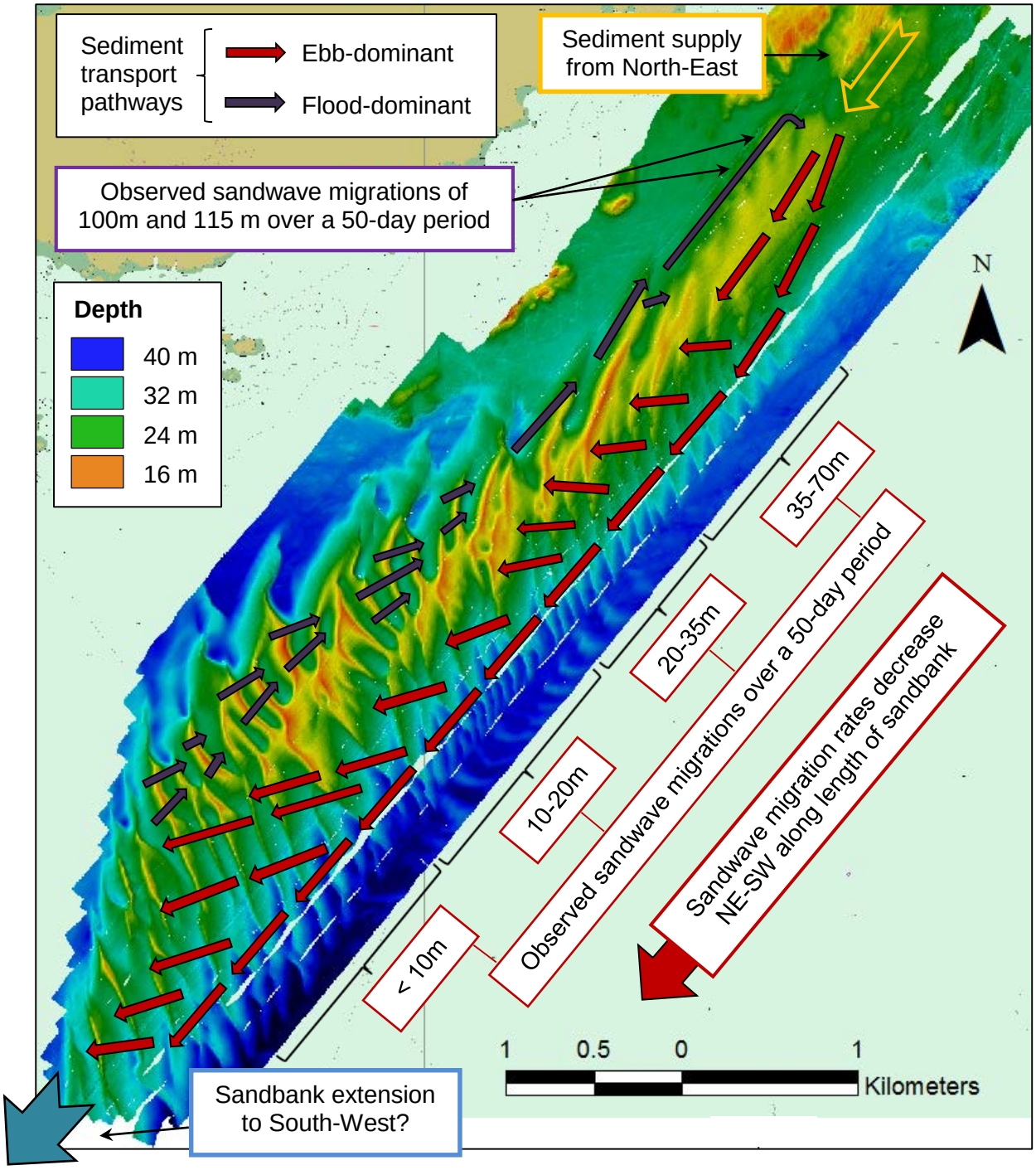

Figure 5.1 Sediment transport pathways around the South Banks as inferred from sandwave asymmetries, orientations and migrations. The transport pathway along which sediment is supplied to the sandbank from the North-East is highlighted. Red arrows relate to the movement of sand along the ebb-dominant outer zone of the sandbank and purple arrows to the directions of sand transport along the flood-dominant inner zone. Arrow size is not related to sediment transport rate.

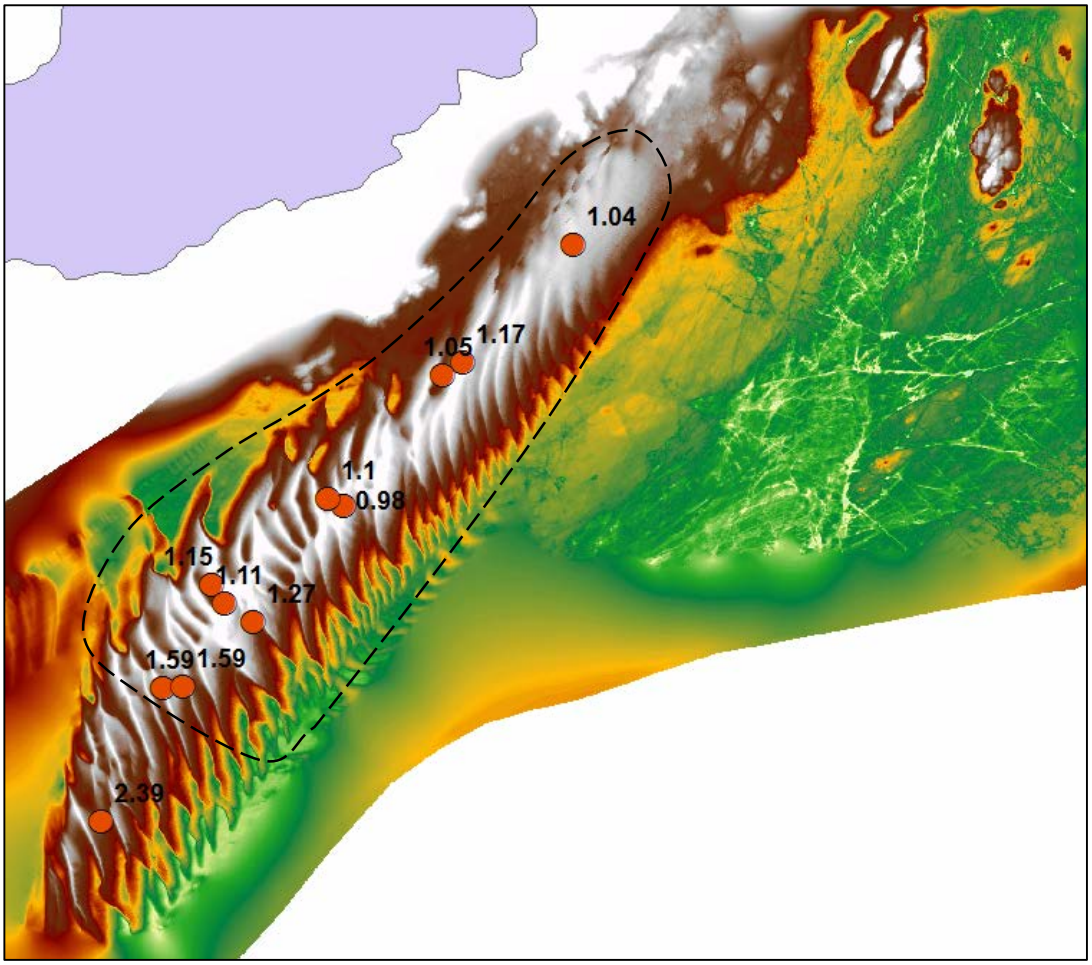

Figure 5.2 Median grain size (d_{50}) variation in mm as determined from grab samples collected at 11 locations along the length of the South Banks. The dotted line indicates the area across which grain size values were averaged for use in the sediment model (section 6.3).

6 Methodology

6.1 Review of suitable numerical modelling software

Functionality and model structure varies significantly between the available coastal modelling software often due to the research intentions of the developers. Software functionality relating to the following factors will be used to determine which modelling software is used for the study:

- *Variable grid spacing* – Computational efficiency and grid resolution must be balanced. It is essential for this study that the model mesh resolution can be varied across the model domain and increased for regions of interest. The ability to contort the grid to match complex coastal geometries and the ability to use large grid spacings at open boundaries will also be beneficial. To enable such un-structured meshes the model must be based upon either the Finite Element (FE) or the Finite Volume (FV) discretization scheme. Although there are methods for warping Finite Difference (FD) meshes to fit irregular boundaries (i.e. boundary fitted curvilinear grids) such an approach would be problematic for large-domain models with islands due to the lack of localised control of mesh resolution. The Finite Difference (FD) method would be by definition unable to accommodate such horizontal variations in grid spacing.

- *Open source source-code (i.e. non-commercial)* - It will be necessary to access and modify the source code of the model to parameterise the effect of energy-extraction and to control the tidal-forcing of the model. Commercial codes do not allow access to their source-codes whereas open-source code models allow full code-access, are typically academic-driven and have the additional advantage of being available for free.

- Code can be run in parallel - Our hydrodynamic model will be computationally expensive. The grid will have 10^5-10^6 nodes and the coupled sediment dynamic module will add to the computing power necessary. It is essential that the model is capable of being run on multiple parallel processors.

- Online forum - An online help forum for users to discuss the intricacies of running the model and to query particular issues with the developers is very useful. Time spent trouble-shooting particularly intricate, technical problems can be significantly reduced when questions can be addressed directly to the model programmers.

Table 6.1 lists the available numerical model software packages that are suitable for coastal-area modelling and that include sediment transport modules.

Table 6.1 Comparison of the available coastal area models based upon functionality and support.

Model	Model type	Mesh	Source-code	Parallel	Forum threads
DELFT3D	3D	FD	OS	Yes	68
ECOMSED	3D	FD	OS	Yes	N/A
MIKE 3	3D	FV	C	Yes*	N/A
POLCOMS	3D	FD	OS	Yes	No
ROMS	3D	FD	OS	Yes	2,265
TELEMAC	2DH/3D	FE	OS	Yes	436

* MIKE 3 can take advantage of multiple cores within a single computer but not large, multi-node super-computers.

The ideal model for our purposes would:

- support unstructured meshes (FV or FE)
- be available non-commercially and open source (OS)
- be able to be run in parallel on multiple cores
- have an active online user and developer forum

The only two models which allow unstructured meshes are TELEMAC and MIKE 3. Of these two software packages only TELEMAC is open-source and MIKE 3 has the further draw-back of not being able to be run in parallel across multi-node super computers. Therefore, the TELEMAC hydro-informatics system (developed by Électricité de France) was chosen to setup and run both the hydrodynamic and sediment model for this study. The TELEMAC suite consists of various modules and

components developed for a wide variety of hydrodynamic applications. For this study we make use of the two-dimensional hydrodynamic model, TELEMAC-2D, and the sediment transport module, SISYPHE.

6.2 Hydrodynamic modelling

TELEMAC-2D was used to develop a 'coastal-area model'-scale hydrodynamic simulation of the Alderney Race located within the larger context of the English Channel (see section 2.3 for an overview of TELEMAC). The modelling system incorporates a variety of phenomena of which the following are of particular interest for this study: The effect of Coriolis acceleration; Bed friction; Wetting and drying of nodes to simulate tidal flats; The inclusion of vertical structures within the flow as an added drag force; Automatic Coriolis variation with latitude via the use of spherical coordinates; Automated coupling with the sediment transport module SISYPHE.

Figure 6.1 is a contour plot of the continuous bathymetric map that was synthesised from multiple sources (OSIRIS Projects, Seastar Survey, TCarta Marine, GEBCO). This was then mapped onto an unstructured mesh with a range of grid spacing from 115-8,000m. Maximum resolution (grid spacing =115m) was focussed around the study site with grid-spacing decreasing with distance from Alderney, as can be seen in Figure 6.2. The final mesh consisted of 100,000 nodes. The sandwaves superimposed upon the South Banks were smoothed out of the bathymetric data using a spatial moving-average approach which preserved the total volume of sand to within 2% of the original value (modelling of sandwave migration is still an active research topic and is not currently applicable for such a complex scenario). Bathymetric contours pre and post smoothing are shown in Figure 6.3.

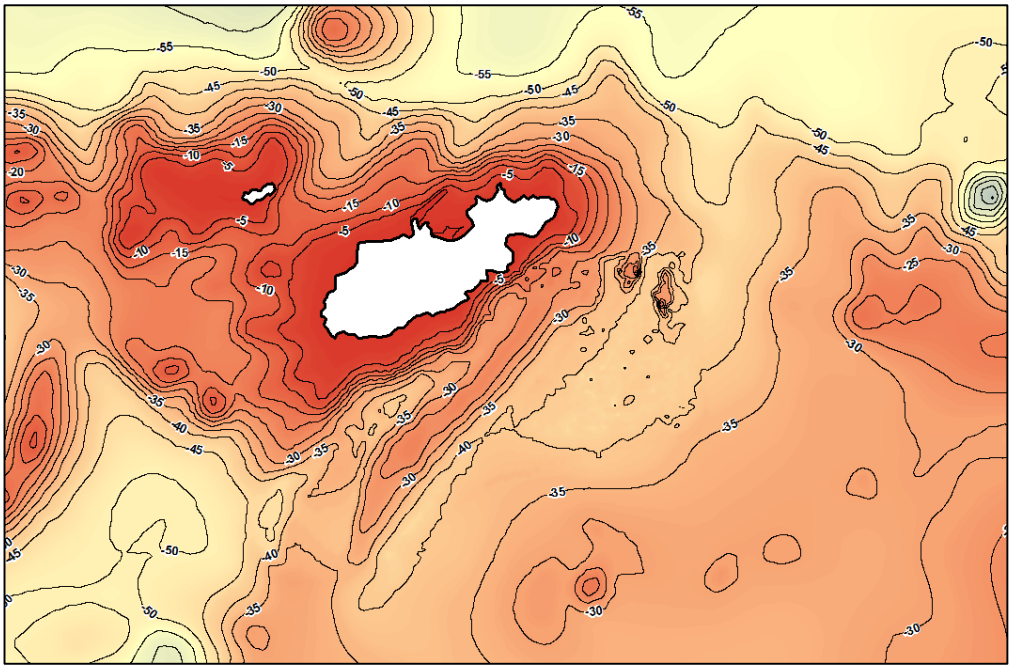

Figure 6.1 Bathymetric map synthesised from multiple data sources (OSIRIS Projects, Seastar Survey, TCarta Marine, GEBCO). The South Banks are well defined to the South of Alderney. Around 3km East of the North-Eastern end of the South Banks can be seen the Race Rocks, located close to the -35m depth contour in the figure. These are two well defined underwater pillars of rock through which the tidal flows are particularly strong.

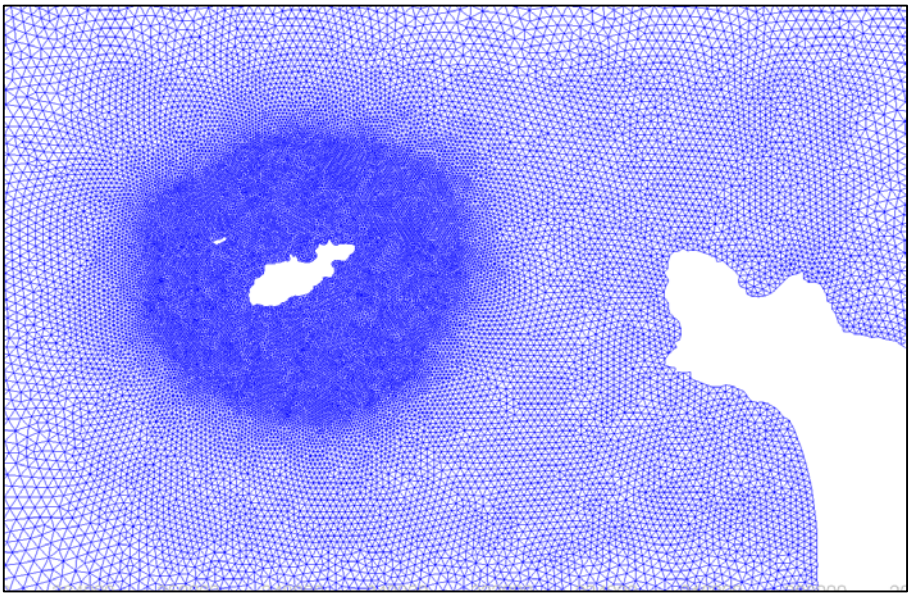

Figure 6.2 Unstructured mesh onto which the bathymetric data was mapped. The mesh resolution increases significantly in the region of Alderney and the South Banks.

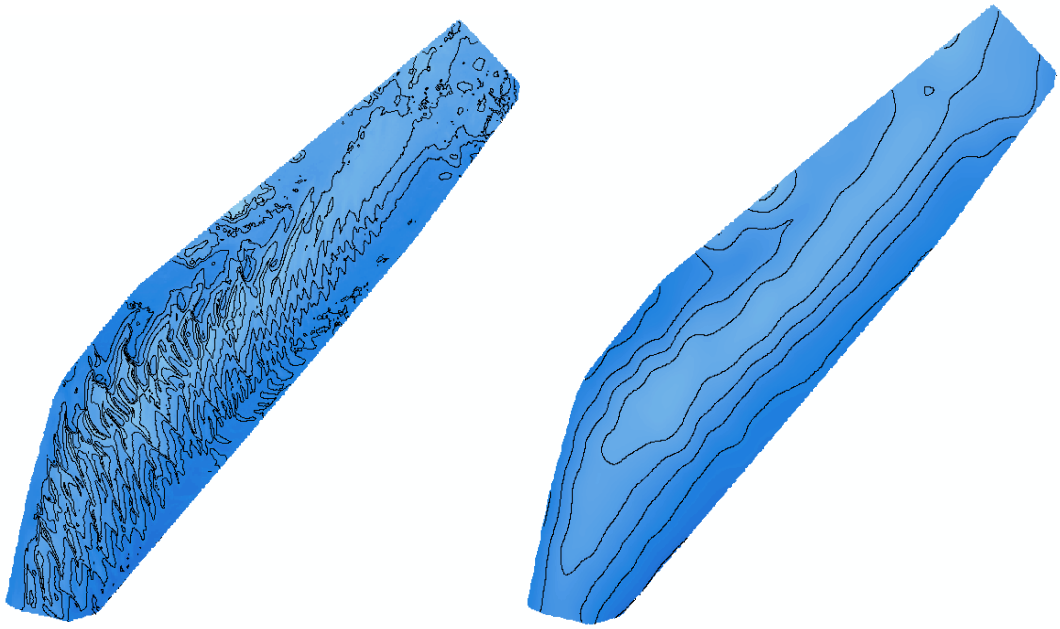

Figure 6.3 South Banks bathymetry contours (a) original dataset (b) after bathymetric smoothing using a spatial moving-average filter

The model was elevation-forced at three liquid boundaries with the principle boundary located over deep water in the Eastern Atlantic Ocean. The tidal signal was constructed using tidal constituent values for amplitude and phase extracted from a global tidal model (OTPS). The other two boundaries were located in the North Sea and the Irish Sea and were forced using constituent values extracted from co-tidal charts (UK Ministry of Energy, 1993). Tidal-forcing signals were constructed using 9 tidal-constituents: M_2, S_2, K_1, O_1, P_1, N_2, K_2, Q_1 and M_4.

Figure 6.4 shows the full-extent of the numerical model domain. A Nikuradse formulation for the bed friction was selected and bed friction was varied across the model domain with 5 distinct regions mapped (Figure 6.4). The 5 regions were selected due to their oceanographic similarity (Deep ocean, Gulf of St. Malo, etc.) and because of their likely utility during the model calibration process. The selection of 5 separate friction regions was considered to be sufficient to adequately tune the model whilst avoiding the risk of relying excessively upon spatial variation and subsequent tuning to match the validation data. Nikuradse friction coefficients (k_s) were manipulated to tune the model during the model validation/calibration phase although the k_s values used were restricted to a range of physically realistic values.

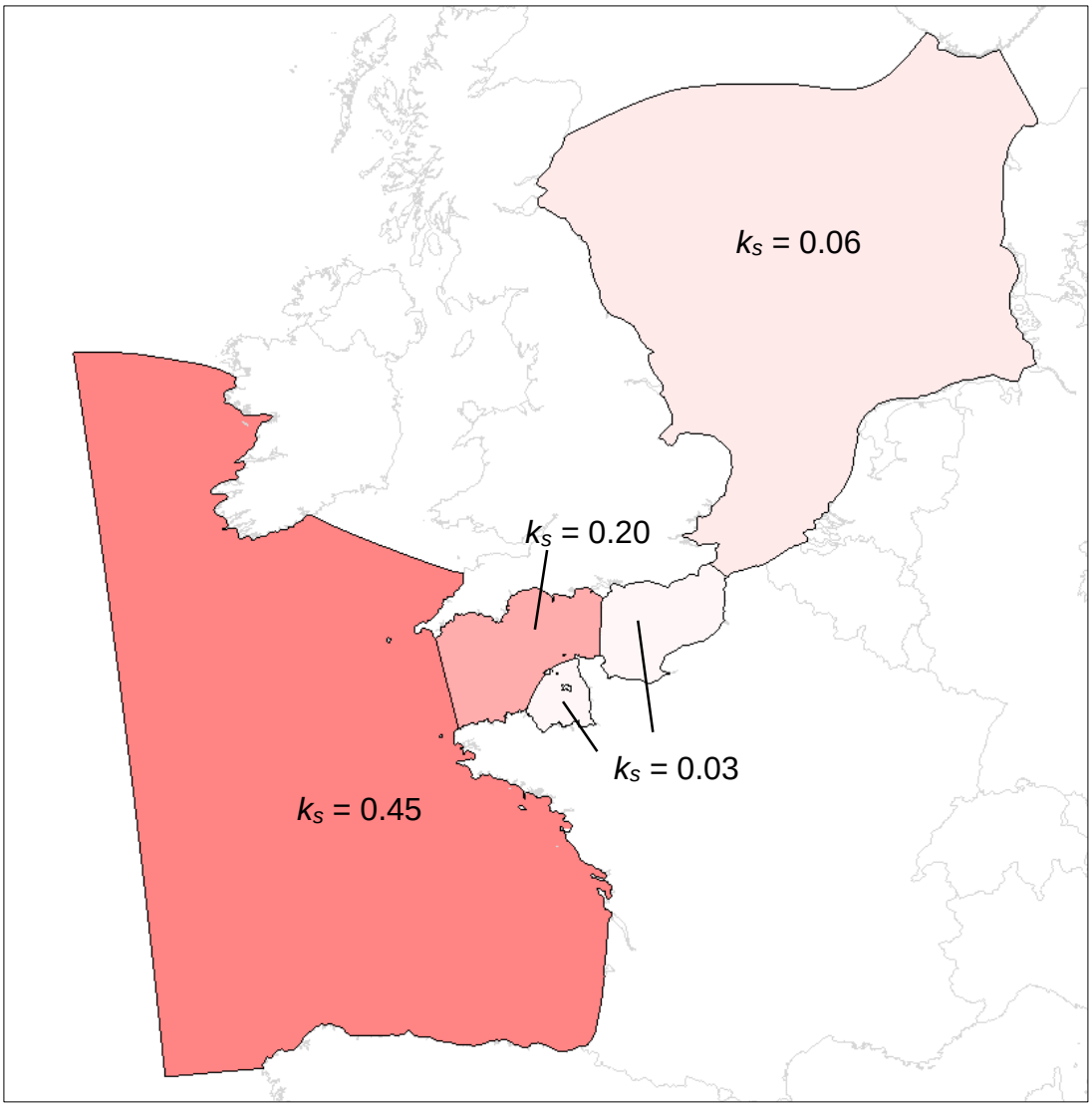

Figure 6.4 Spatial variation of the Nikuradse bed friction coefficient (k_s) across the model domain with five zones of constant bed friction specified.

The model was validated and calibrated using two species of data: tidal elevation data and tidal stream velocity data (see section 7.1). Elevation time-series data were obtained from national tide gauge data archives relating to 14 ports located within the model domain. Port selection was guided by the availability of consistent, long-term elevation datasets and the need to cover as much of the domain as possible. Elevation time series were extracted for the corresponding locations in our model. Harmonic analysis of both the real-world data and our model outputs was performed and the *amplitude* and *phase* values relating to the M2 and S2 tidal constituents compared. A similar approach was used for validation/calibration of the model tidal stream velocities against the measured ADCP data. An identical harmonic analysis of the model and real-world data was performed with the *major-axis amplitude*, *major-*

axis phase and the tidal ellipse *inclination* values compared for both the M2 and the S2 tidal constituents. The model was also validated for tidal stream velocities against Admiralty tidal diamond 2669E which is located in the Alderney Race. The hourly velocity information from the diamond was reconstructed using the standard Admiralty method and then harmonically analysed.

The model was calibrated using a combination of mesh refinement, bed friction coefficient tuning and the systematic investigation of a large number of physical and numerical parameters defined in TELEMAC-2D. Validation of the model against tidal stream data was prioritised over tidal elevation data for obvious reasons. It was the aim of the validation phase to try and reduce discrepancies between the model and the real-world data to less than 10% for amplitudes and 10° for phases and inclinations.

6.3 Sediment modelling

6.3.1 Choice of sediment transport formula

The sediment transport formula section of the literature review was used to assess which formulations are best suited for modelling sediment transport over the South Banks. The formulas of Yang (1973), Van Rijn (1984), Engelund and Hansen (1972) and Ackers and White (1973) perform with most consistency for the multiple formula comparison studies presented in section 3.2.2. In particular the Yang and Van Rijn formulas predict very high percentages of measured values within a factor of two (see Tables 3.2-3.5). The Engelund-Hansen and Ackers-White formulas perform moderately well in many comparisons, achieving lower accuracy rates but still consistently out-performing many of the other available transport formulas (see Table 3.4 and Table 3.5).

The very strong performance of the Van Rijn formula when tested using both river data (Van Rijn, 1984; Table 3.1) and estuary data (Voogt et al., 1991; Table 3.2) suggests that this formulation is the most suitable for predicting transport rates in the coastal environment. The Engelund-Hansen and Ackers-White formulas perform well for the river data in the Van Rijn comparison (Table 3.1) but badly for the river data in the Yang and Wan comparison (1991; Table 3.3). They also fail to predict more than 1/3 of the estuary data within a factor of two of measured values (Table 3.2). Although the formula of Yang (1973) predicts transport rates very well for flumes and small

rivers there appears to be a systematic error in the formulation for large depths (Van Rijn, 1993) with only 39% of measured values predicted within a factor of two (Table 3.1; Van Rijn, 1984). In this same comparison the formulas of Van Rijn, Engelund-Hansen and Ackers-White achieve prediction accuracies of 76%, 64% and 63% respectively. Use of the Yang formula to predict transport rates over the South Banks is therefore unlikely to produce useful results due to the large water depths (15-40m).

The stated depth range for validity of the Van Rijn formula (1-20m) is the largest of the sediment transport formula reviewed. Even so, the depths over the South Banks are mostly beyond this range (15-40m). The use of any sediment transport formulas in such depths is tentative but remains the best available option for making transport rate predictions in inaccessible and often challenging marine climates. A review of the literature relating to academic and industrial practice (HR Wallingford report, 2001; Bastos et al. 2003; Berthot and Pattiaratchi, 2005; Neil et al., 2012) supports the speculative use of the most suitable transport formulas outside their stated depth validity ranges where no other prediction options are available.

The formulas of Van Rijn (1984), Engelund and Hansen (1972) and Ackers and White (1973) were identified as the three most suitable for use in the sediment modelling component of the project. The use of multiple viable transport formulas (as suggested by Yang; 1996) with the intention of comparing the outputs was beyond the scope of the work due to time-constraints. It was therefore decided that only the most suitable transport formulation would be used for the study.

The literature review suggests that the Van Rijn formula is the most likely of the three to perform well with the Engelund-Hansen and Ackers and White performing at lower but similar levels of accuracy (i.e. percentage of predicted values within a factor of two of measured values). Yang's criteria for choosing sediment transport formula (Yang, 1996) supports the use of the Engelund-Hansen and Ackers-White formulas in subcritical flow conditions (i.e. even the fastest tidal flows will have a Froude number of significantly less than one for the large water depths found at the South banks). A review of similar modelling studies present in the literature strongly supports the use of the Van Rijn transport formula for predicting sediment transport in comparatively deep tidal waters (see Signell and Harris, 2000; Berthot and Pattiaratchi, 2005; Neil et al. 2009; Neil et al. 2012). The Van Rijn method was therefore chosen for use in the sedimentary modelling phase of the research due to its excellent performance in estuary and river conditions, it's unusually large depth

validity range and its regular usage in both academic and industrial studies. Owing to the treatment and presentation of Van Rijn's total load formula (1984) by Soulsby (1997) the formula are usually referred to in the modelling literature as the Soulsby-Van Rijn formula. This convention will be used for the remainder of the report.

6.3.2 Soulsby-Van Rijn formula

The Soulsby-Van Rijn was setup within the sediment module SISYPHE to model sediment transport over the South Banks. The formulation outlined in section 3.2.1 is presented here again with the addition of the threshold calculations necessary for specifying the formulas within SISYPHE. The Soulsby-Van Rijn method requires depth-averaged velocity, $\bar{U}$, and water depth, d, as inputs in addition to specification of sediment and water characteristics. It does not require an explicit bed roughness value as the effects of variable roughness are ascertained from the particle characteristics. This non-dependence upon a predicted bed roughness value is one of the reasons that the Soulsby-Van Rijn formula performs so consistently well (Van Rijn, 1993) compared with the Engelund-Hansen and Ackers-White formulas.

$$q_t = q_b + q_s \tag{6.1}$$

$$q_b = 0.005\ \bar{\mathrm{U}}\ h\left\{\frac{\bar{\mathrm{U}}-\bar{\mathrm{U}}_{cr}}{[(s-1)gd_{50}]^{0.5}}\right\}^{2.4}\left(\frac{d_{50}}{h}\right)^{1.2} \tag{6.2}$$

$$q_s = 0.012\ \bar{\mathrm{U}}\ h\left\{\frac{\bar{\mathrm{U}}-\bar{\mathrm{U}}_{cr}}{[(s-1)gd_{50}]^{0.5}}\right\}^{2.4}\left(\frac{d_{50}}{h}\right)(D_*)^{-0.6} \tag{6.3}$$

Where: q_t = total-load, q_b = bedload, q_s = suspended-load, $\bar{U}$ = depth-averaged flow velocity, $\bar{U}_{cr}$ = depth-averaged critical velocity, h = water depth, d_{50} = *median* grain size, g = gravity, s = the ratio of sediment density to water density, D_*=dimensionless grain size.

The *depth-averaged critical velocity,* $\bar{U}_{cr}$, determines the sediment *threshold of motion* and is defined using one of two different formulations relating to sediment size:

$$\bar{\mathrm{U}}_{cr} = 0.19(d_{50})^{0.1}\ log_{10}\left(\frac{4h}{d_{90}}\right) \qquad for \quad 0.1 \le d_{50} \le 0.5\ mm \tag{6.4}$$

$$\bar{\mathrm{U}}_{cr} = 8.5(d_{50})^{0.6}\ log_{10}\left(\frac{4h}{d_{90}}\right) \qquad for \quad 0.5 \le d_{50} \le 2\ mm \tag{6.5}$$

Where d_{90} = *the grain size for which 90% of the grains are finer.* SI units must be used for entry of the grain size values.

6.3.3 Verification of residual transport rates

Calculations of bedload transport rates at the South Banks (derived from sandwave migrations; see section 2.7.4) provide us with a particularly useful method for assessing residual transport rates over the bank. The temporal averaging implicit in the measurement of sandwave migration (i.e. 50 day period, multiple spring-neap cycles) produces a robust value for minimum residual bedload transport rates. This, in turn, enables a tentative extrapolation to residual total-load transport rates to be posited. The proposed value for residual total-load transport (q_t = 4.0 m^2/day on the South-Eastern flank; section 5.3) will constitute a rough guide for verifying our hydrodynamic model outputs and assessing our sediment model outputs for realism.

6.3.4 Sediment grain size inputs

Sediment grain-size parameters of d_{50} = 1.1mm and d_{90} = 2.3mm were derived from the sediment survey grab samples and defined in SISYPHE for the sediment modelling phase. These values are averages relating to the eight most North-Easterly samples collected at the South Banks as shown by the dotted line in Figure 5.2. The significant increase in grain-size towards the South-Westerly end of the bank is not represented by our sediment model therefore transport rates in this region will be overestimates (see equations 6.2, 6.3 and 6.5 above). The three sediment grabs in this region were not incorporated in the averages. It was considered more important to maintain a realistic average for the larger area of the bank across which grain sizes fluctuate less, than to skew grain sizes for the whole bank.

6.3.5 Implementation of an un-erodible rigid bed layer

Morphological/sedimentary models of the coastal-zone typically define their model domains as uniformly erodible with an abundant supply of sediment because there is often a shortage of information relating to the underlying bedrock layer. In areas of high-energy tidal flows this is particularly problematic. Regions in which velocities are consistently high often constitute un-erodible bedrock in the real-world environment. If beds are modelled as uniformly-erodible then these very areas will experience the fastest erosion rates and therefore input unrealistically large volumes of sediment into the morphological model. This dynamic is particularly relevant for sedimentary

models of the Alderney Race where a large, mobile sandbank is located adjacent to an extensive, un-erodible bedrock layer to the East, as can be seen in Figure 5.2.

The ability of SISYPHE to define an un-erodible *rigid bed* layer in the model was employed to specify potential erosion depths across the domain. High resolution swath-bathymetry collected at the South Banks provided sufficient information to interpolate the surrounding bedrock layer beneath the sandbank as shown in Figure 6.5.

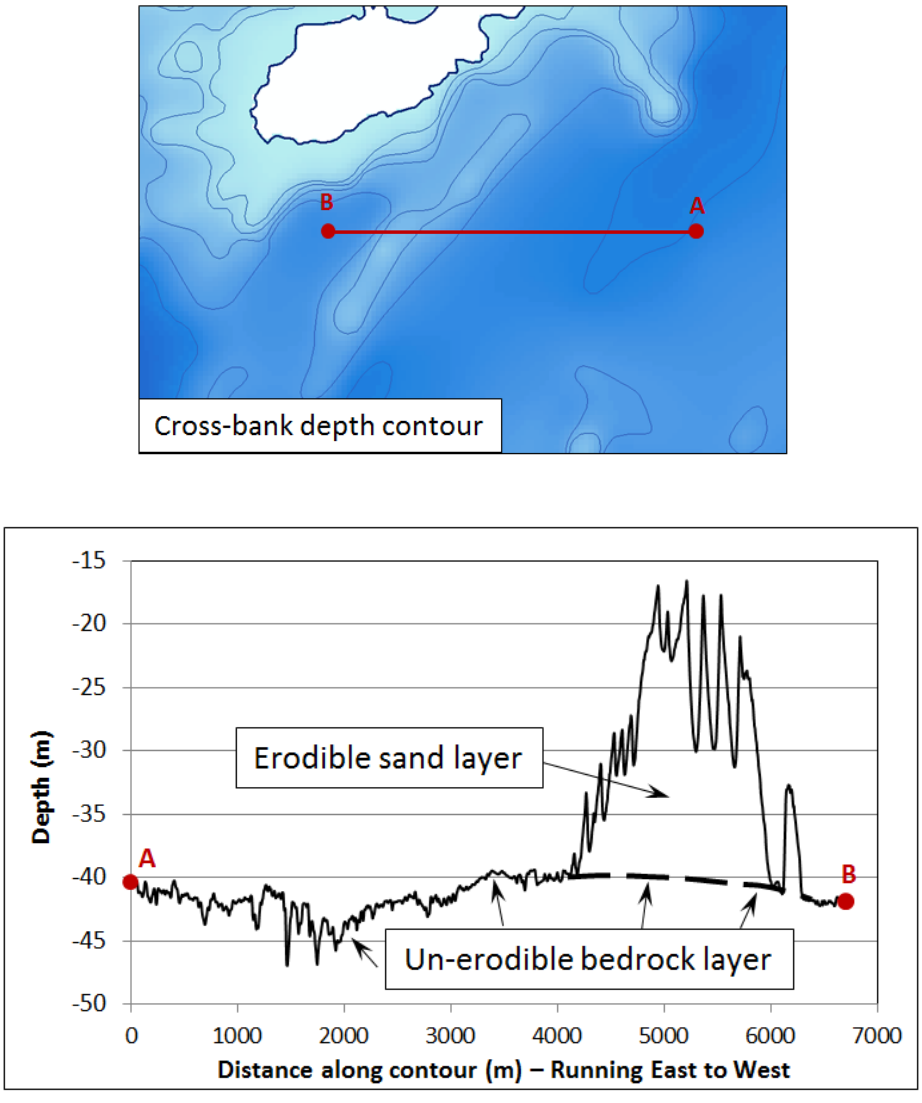

Figure 6.5 Un-erodible *rigid bed* layer defined using a bathymetric interpolation beneath the South Banks.

The South Banks are situated on top of two separate bedrock strata with a marked transition of ~8m between them which is represented by the blue line in Figure 6.6. Separate interpolations beneath the sandbank were made for these two regions and combined to produce a continuous bedrock layer wihin the dotted red line in Figure 6.6. This was then combined with the bathymetry for the wider domain and applied as a model-wide *rigid bed* layer. Only model nodes situated within this dotted red line were able to erode and the sediment supply to the morphological model is therefore limited to sand originating from the sandbank. The question of sediment supply to the South Banks is an important one but there is insufficient bathymetric coverage to adequately extend the available sediment supply towards the headland tip (from where any supply of sediment to the sandbank is likely to be transported). The morphological stage of this study aims to explore how energy extraction will impact upon sand movement around the sandbank and subsequent changes in bed-level. Sediment supply is therefore not considered in the sediment model although potential energy extraction effects upon the hydrodynamics of a hypothetical 'sediment supply pathway' are considered during the zoned analysis in chapter 8.

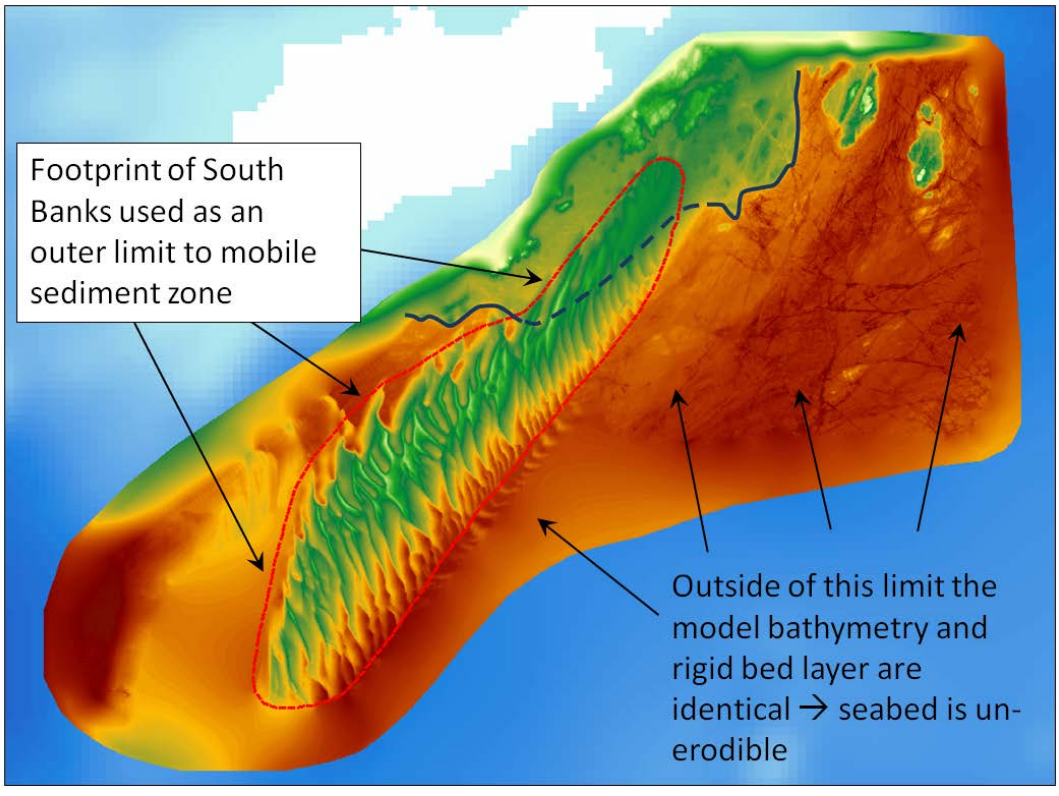

Figure 6.6 Limit of un-erodible *rigid bed* layer employed in the sedimentary model. The seabed within the dotted red line is erodible down to the depth of the rigid bed passing beneath the sandbank.

6.4 Energy extraction

The area-averaged array method developed by Blunden (2009; see section 2.4) was incorporated into the model using a modified version of the subroutine DRAGFO. An equivalent turbine drag coefficient is calculated using the specified turbine and array parameters and the local sea bed friction parameter.

The impacts of installation and operation of a large 300MW tidal array were chosen as the predominant focus of the study. A 16m diameter horizontal axis turbine of 2MW rated power and rated speed of 3.5 m/s was chosen as a suitably representative device and the relevant parameters included in the subroutine. Calculations relating to optimal turbine spacing (for power output) were balanced with considerations relating to likely array coverage to determine the format of the array (i.e. lateral and longitudinal spacing between turbines, total array dimensions). A 1.2km long, 0.8km wide array equivalent to 10 rows deep of 15 turbines per row facing the flow was adopted as the basic 300MW array format for the study (i.e. 10 x 15 = 150 2MW rated turbines = 300MW rated array). The parameters used in the array modelling process are summarised in Table 6.2.

Table 6.2: Parameters used to model arrays. Lateral and longitudinal turbine spacing are given as multiples of turbine diameters.

Parameter	**300 MW array**
N	150
D	16 m
L_x/D	11.3
L_y/D	4.2
U_r	3.5 m/s
c_d	0.9
c_d'	0.57

Where *N = number of devices in array*
D = device diameter
L_x & L_y = longitudinal and lateral spacing respectively
U_r = rated speed of device
c_d = device drag coefficient
c_d' = equivalent turbine drag coefficient (combined seabed and device; Blunden, 2009)

6.5 Array footprints and extraction scenarios

The impact of varying the array location in the Alderney Race was investigated using a systematic approach with multiple energy extraction scenarios modelled. A 300MW rated power array parameterisation was applied to each of seventeen selected T-blocks in the race in turn, the array footprints of which are shown in Figure 6.7. In addition to the varying location the spatial orientation of the arrays was related to the local M_2 tidal-constituent *inclination*. These values were calculated from multiple velocity time-series extracted from the baseline case at the centre of each T-block.

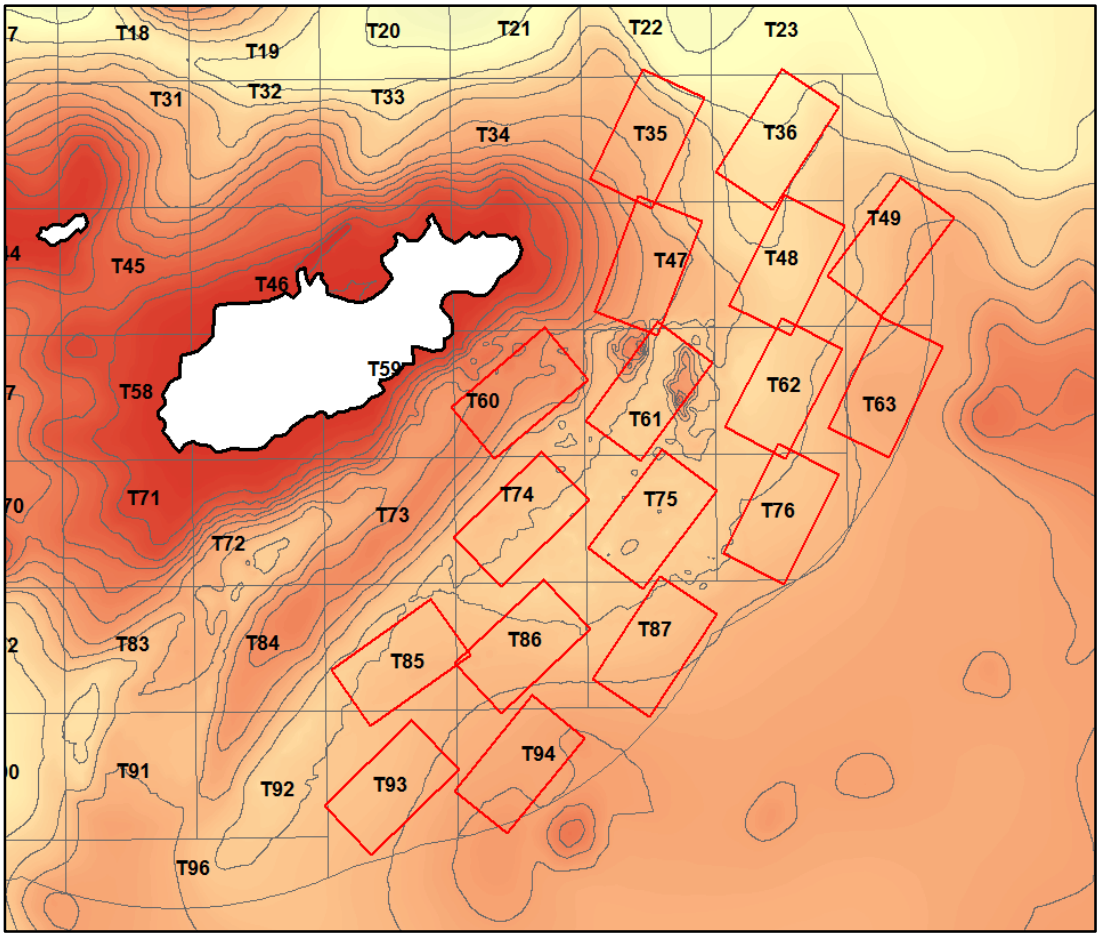

Figure 6.7 Array footprints for seventeen different energy extraction scenarios. Each modelled array is situated within a different development T-block and is orientated relative to the local M_2 tidal-constituent *inclination*.

6.6 Modelling approach

The modelling phase consists of two distinct stages: a hydrodynamics-only model (TELEMAC-2D) and a sedimentary model (TELEMAC-2D coupled with SISYPHE). For both stages a similar approach is used. Outputs from a baseline model run (no energy extraction) are compared with outputs from 17 energy extraction scenarios (see chapters 7-8). Baseline and energy-extraction models are setup identically (i.e. model-run time, tidal boundary forcing, format of results) with the exception of the added drag force representing the arrays. Extraction outputs are then subtracted from the baseline outputs (velocity for the hydrodynamic model, bed-level evolution for the sedimentary model) to quantify the spatial and time-varying impact of each extraction scenario. These 'difference-outputs' are then interpreted, using various mathematical and visualisation methods, to help assess the likely impact of each extraction-scenario upon the South Banks' morphology.

The hydrodynamics-only model was setup to run for one spring-neap cycle (14.8 days). Forcing of the model using multiple tidal-constituents (in addition to M_2 and S_2) means that the modelled period must relate to a real-world period of time as opposed to representing a generic spring-neap cycle. The spring-neap cycle chosen was from Friday 14th August to Friday 28th August 2009 with the spring tide occurring in the middle of the model-runs. This period was chosen because the model was primarily validated using ADCP data collected during 2009 and the cycle is one of the largest cycles of the year. The model is therefore conservative in that it represents the impacts of energy extraction during a period of higher-than-average tidal velocities.

The sediment model was setup to run for a longer time-period than the hydrodynamics-only model to help investigate cumulative impacts on a larger time scale. A model run of 90 days (3 months) was chosen and was situated *symmetrically* in time around the hydrodynamic-only modelling period (i.e. July-September 2009). The model run encompasses ~6 spring-neap cycles with the principal output consisting of bed evolution time-series for each node of the model mesh.

7 Results

The results from the computational fluid dynamics modelling phase fall naturally into 5 sections. The first concerns the validation of the hydrodynamic model by the comparison of model outputs with real-world validation data. The second explores the results and behaviour of this validated 'baseline model' in terms of tidal currents, residual sediment transport and bed-level evolution. The subsequent three sections explore how inclusion of the effects of energy extraction within the model alter these baseline patterns of tidal currents, residual sediment transport and bed-level evolution.

7.1 Validation of hydrodynamic model

Three species of data have been used to test, refine and establish the validity of the baseline model:

- Tidal elevation data collected at multiple ports located within the model domain.
- Tidal stream data captured during static ADCP deployments in the Race of Alderney.
- Tidal diamond velocity information relating to the Race of Alderney.

7.1.1 Model refinement criteria

The refinement of model parameter space to reduce discrepancies with validation data is a complex process. A numerical model is an approximation of the 'real-world' scenario and an 'absolute' validation of the model is impossible: attempts to improve model veracity at one location often lead to deteriorations at another. It is therefore necessary to establish a *hierarchy of importance* with respect to validation at different locations and between differing species of data. The following hierarchy was used to guide the model refinement process (criteria are outlined below):

1. RDI ADCP data from blocks T61 and T75
2. AWAC ADCP data from blocks T61, T75 and T74
3. Tidal elevation at Cherbourg and Jersey
4. Tidal diamond 2669E – Race of Alderney
5. Tidal elevation – remaining ports

The following points were used to arrive at the above hierarchy:

- The ultimate aim of the study relates to tidal velocities within and around the Race of Alderney, particularly in the vicinity of The South Banks. Validation of model tidal stream velocities using ADCP data is therefore the priority.
- There appears to be a discrepancy between data collected by the RDI and AWAC models of ADCP (the deployments were not spatially coincident so we cannot be certain). Refinement of the model to match ADCP amplitudes involves scaling the kinetic energy in the flow by varying energy dissipation elsewhere in the model. Model differences at a specific ADCP location cannot be altered without scaling *all of the ADCP differences* to some extent. We have therefore prioritised validation using the two RDI ADCPs as the data appears to be more consistent and can be simultaneously matched at the same 'energy level'. Tidal stream amplitudes for the AWACs in T61 and T75 can be closely matched at higher and lower model energy levels respectively. The aim of validation must be to achieve the best *overall fit* of our model to the available ADCP data and the RDI data constitutes a suitable mean. It should also be noted that the T74 AWAC lies in the path of the large circulating eddy shed from the North-Eastern tip of Alderney at the beginning of the ebb tide. The complex flow regime observed during the propagation of this eddy makes validation at this location particularly challenging.
- Comparison of tidal elevations is important to ensure that the model is recreating the underlying physics of the 'real-world' domain. The importance of elevation validation diminishes with distance from the study site.
- Bathymetric inaccuracies are particularly prone to cause errors in shallower coastline regions. Tidal diamond 2669E relates to a position in deeper water far from the coastline and in a less complex tidal regime than the ADCP deployments.

7.1.2 Model accuracy and calibration

The aim of the model refinement process was to achieve the following maximum margins of error between our model outputs and the validation data where possible:

- Tidal elevation: M_2 and S_2 amplitudes differences < ±10%
  M_2 and S_2 phases differences < ±10°
- Tidal stream velocities: M_2 and S_2 amplitudes differences < ±10%
  M_2 and S_2 phases differences < ±10°M_2 and S_2 ellipse inclinations < ±10° (spatial axis)

M_2 amplitudes are significantly larger than the S_2 amplitudes in the English Channel and are consequently far more important for us to recreate accurately.

The model was calibrated using a systematic approach to varying both physical and numerical model parameters in the TELEMAC steering file. The overall accuracy of each corresponding model run relative to the validation data was assessed within the context of the model refinement criteria discussed in section 7.1.1. Variation of many of the physical and numerical parameters produced a negligible effect upon the accuracy of the model (e.g. TURBULENCE MODEL, SOLVER, MASS-LUMPING ON H). The most critical physical model variables appeared to be FRICTION COEFFICIENT and CORIOLIS. The most critical numerical variables were OPTION FOR LIQUID BOUNDARIES and TYPE OF ADVECTION. This exploration of the effect of parameters upon model accuracy yielded an optimum combination of physical and numerical parameters which were subsequently used for the baseline model (see Appendix B for specific parameter choices).

7.1.3 Tidal elevation

The baseline model was validated for tidal elevation at 14 ports located within the model domain. Figure 7.1 shows the port locations. Port selection was guided by the availability of consistent, long-term elevation datasets and the need to cover as much of the domain as possible.

Figure 7.1 The 14 ports used to validate the baseline model for tidal elevation.

Harmonic analysis of both the model and real-world elevation data produces an *amplitude* and a *phase* value for each of the two tidal constituents used for validation (M_2 and S_2). The differences between the amplitude values are calculated in metres and as the percentage difference of the model value relative to the real-world value. These difference values are collected in Table 7.1. The phase differences are quoted in degrees. Figure 7.2(a) illustrates *absolute* M_2 and S_2 amplitudes for the model and the validation data. The 14 ports are arranged in terms of position (ports are ordered anti-clockwise around the English Channel from Concarneau to Newlyn with the final three ports running south to North along the West coast of the North Sea). Figure 7.2 (b)-(c) illustrate percentage amplitude differences and phase differences in degrees between the model and the validation data. The limits of the desired maximum error are denoted by dotted lines.

Amplitude/phase differences of < ±10% / 10° between the model and validation data have been achieved for 10 of the 14 ports (Table 7.1). Figure 7.2(a) shows that the

variation in real-world amplitudes across the domain is well-reproduced by the model for both tidal constituents. The large M_2 amplitude percentage differences at Bournemouth and Weymouth correspond to comparatively small *absolute* differences between the model and the real-world data as can be seen by comparing Figure 7.2(a) with Figure 7.2(b). A degenerate M_2 amphidrome (point of zero tidal amplitude that is degenerate because it is shifted inland by friction) is located North of Bournemouth; the region proves challenging to model accurately explaining the large M_2 phase error at Bournemouth.

Table 7.1: Amplitude and phase differences between modelled and real-world elevation datasets for two constituents (M_2 and S_2) at 14 ports. Differences less than 10% for amplitudes and 10° for phases are highlighted in red.

	M_2			**S_2**		
Ports	Amp (m)	(%)	Phase (degree)	Amp (m)	(%)	Phase (degree)
Concarneau	0.03	1.7	-6.3	0.04	7.3	-7.0
Saint-Malo	0.33	8.9	4.0	0.07	4.8	6.4
Jersey	0.19	5.7	4.3	0.01	0.4	5.5
Cherbourg	-0.13	-7.0	-1.8	-0.05	-7.3	-1.9
Le Havre	-0.18	-6.9	5.5	-0.08	-8.6	5.0
Dunkirk	-0.29	-13.4	-0.1	-0.11	-16.3	1.1
Dover	-0.06	-2.8	4.9	-0.04	-5.8	6.4
Newhaven	-0.12	-5.3	6.3	-0.06	-8.6	5.9
Bournemouth	-0.13	-32.4	-23.1	-0.01	-5.3	-18.6
Weymouth	0.15	25.0	-8.1	0.04	14.6	-5.0
Newlyn	-0.10	-6.1	0.4	-0.02	-4.3	-1.0
Cromer	-0.01	-0.8	-4.2	-0.05	-9.4	-5.0
Whitby	0.03	2.0	-8.7	0.01	1.6	-11.0
North Shields	-0.01	-0.9	-6.9	0.00	0.7	-9.1

Amplitudes at Dunkirk are particularly sensitive to the relative progression of high-water South along the West of the North-Sea and the high-water time in the North-Eastern portion of the English Channel. Interestingly the phase differences are very small (-0.1° and 1.1°) whilst the model amplitudes undershoot the real-world data by 13.4% (M_2) and 16.3% (S_2).

Validation at the two ports closest to the study site (Cherbourg and Jersey) reveals favourable phase differences with Cherbourg performing particularly well. The model

amplitudes undershoot and overshoot the real-world data at Jersey and Cherbourg by -7.0% and 5.7% respectively.

(a) Tidal constituent amplitudes (M_2 and S_2) at 14 ports for modelled and real-world elevations.

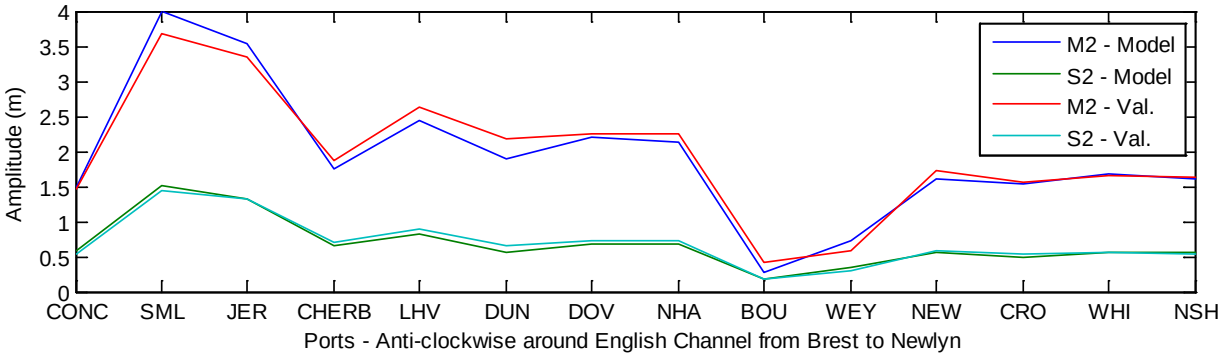

(b) Percentage differences between modelled and real-world tidal constituent amplitudes (M_2 and S_2) for 14 ports. Dotted lines represent ±10%.

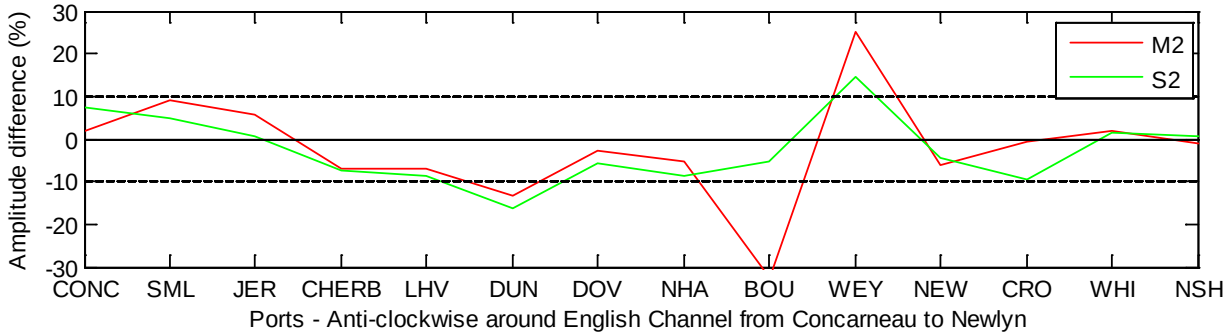

(c) Differences in degrees between modelled and real-world tidal constituent phases (M_2 and S_2) for 14 ports. Dotted lines represent ±10°.

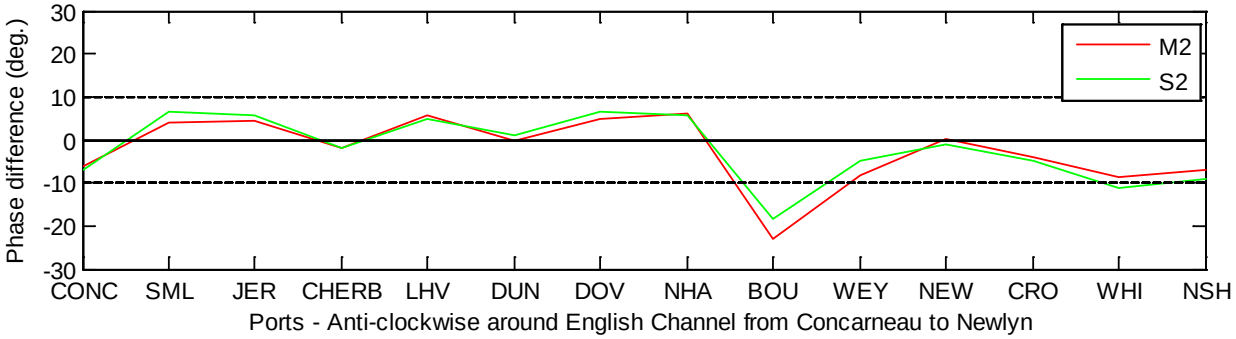

Figure 7.2 Tidal constituent amplitudes at 14 ports for modelled and real-world elevations. Percentage differences illustrate the accuracy of the model constituents relative to the measured real-world constituents.

7.1.4 Tidal stream – ADCP (Acoustic Doppler Current Profiler)

Data collected during five ADCP deployments (conducted by Osiris in summer 2009) were used to validate the model for tidal stream velocities. Figure 7.3 shows the ADCP locations. Each deployment covers a one month period and relates to a different gridded area in a region to the East of the Alderney South Banks. Two different models of ADCP were deployed; AWACs and RDIs. An AWAC ADCP deployed in area T74 captured data from 1st May to 4th June 2009. The AWAC ADCPs relating to areas T61 and T75 were initially deployed on 1st May but, due to technical problems, were redeployed from 17th June to the 27th July and yielded complete datasets for these periods. Two RDI ADCPs were also deployed in T61 and T75 alongside the AWACs from the 17th June to the 27th July.

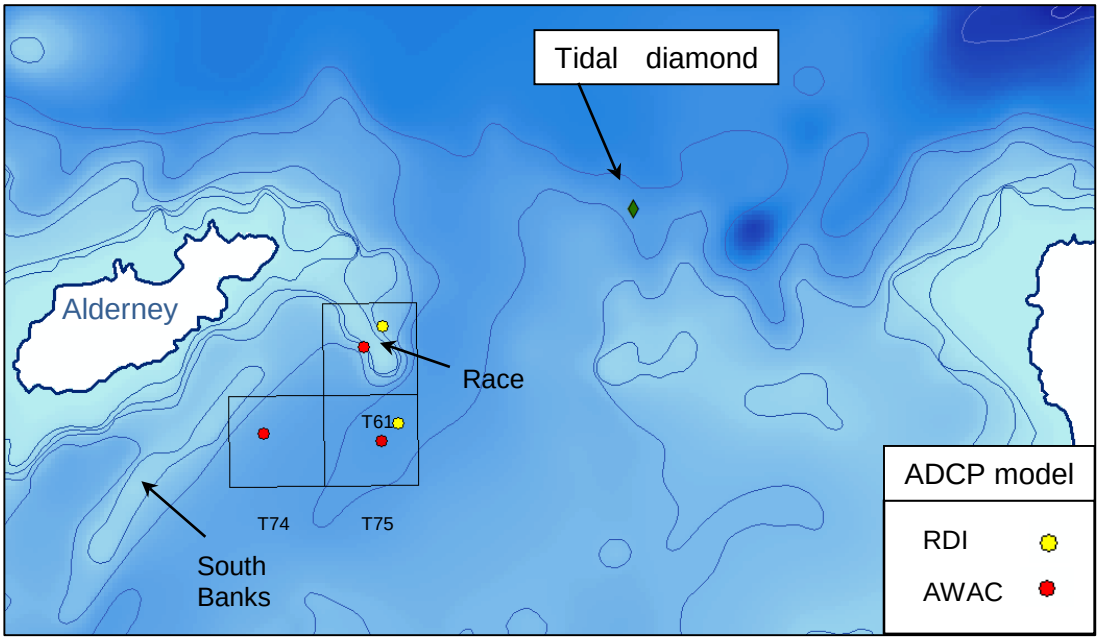

Figure 7.3 ADCP and tidal diamond locations for tidal stream validation of the baseline model.

Harmonic analysis of a tidal stream time series produces 4 values for each constituent analysed:

- The *major axis* of velocity (m/s)
- The *minor axis* of velocity (m/s)
- The *inclination* (degrees) that relates to the spatial orientation of the major axis
- A *phase* value (degrees) that is equivalent to that produced by the harmonic analysis of elevation data

The first three of these values can be represented graphically as a *tidal stream ellipse*. Tidal ellipses provide an intuitive and useful method for displaying such data although they do not easily allow the display of phase values. Figure 7.4 defines the tidal stream ellipse for a general tidal constituent *k*. The tidal stream magnitude at time, *t*, is represented by $C_k(t)$. The inclination, θ_k, defines the orientation of the major axis.

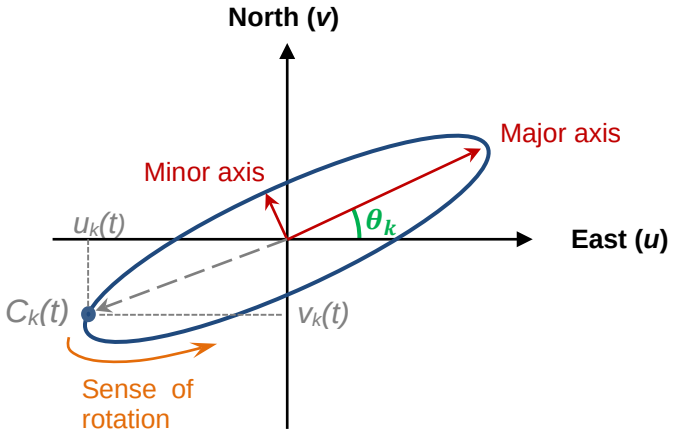

Figure 7.4 Definition of tidal stream ellipse parameters for constituent *k (*reproduced from Blunden et al.; 2008).

The major axis and minor axis of velocity can be understood as a vector equivalent of the scalar amplitude value yielded by analysis of tidal elevation data. In the validation plots presented below it is the major axis values, rather than the minor axis values, that are used to validate the model. The major axis value relates most directly to the maximum tidal currents found at any particular location and it is typically much larger than the corresponding minor axis value. At any particular time, *t*, the tidal stream velocity for the relevant constituent, *k*, relates to a particular point on the ellipse.

Table 7.2 displays tidal stream velocity differences between the model output and the ADCP data for the most significant parameters: *major axis* (absolute and percentage differences), phase (degrees) and inclination (degrees). The corresponding tidal stream ellipse comparisons are plotted for each ADCP in Figures 7.5-7.9.

The RDI comparisons at T61 and T75 are very low with all M_2 parameters achieving errors under 5%/5°. The AWAC comparisons in T61 and T75 result in M_2 major axis and phase differences of < ±10%/10° and inclination differences of < ±15%/15°. The single AWAC comparison in T74 results in M_2 parameter differences of < ±10%/10°.

Table 7.2: Major axis, phase and inclination differences between modelled and real-world tidal stream velocity datasets for two constituents (M_2 and S_2) at 5 ADCP locations. Differences less than 10% for major axis and 10° for phase and inclination are highlighted in red.

	M_2				**S_2**			
ADCP	Major axis (m/s)		Phase (degrees)	Inclination (degrees)	Major axis (m/s)		Phase (degrees)	Inclination (degrees)
T61 - RDI	0.08	2.9	3.9	-0.9	0.58	138.1	0.5	2.0
T61 - AWAC	-0.06	-2.3	0.2	-7.36	0.47	97.9	-3.2	-9.5
T75 - RDI	0.06	2.7	2.9	-0.3	0.40	94.6	5.3	-1.4
T75 - AWAC	0.14	6.4	2.9	13.05	0.41	100.0	0.3	13.1
T74 - AWAC	-0.11	-6.7	-0.1	3.7	-0.13	21.2	29.0	2.6

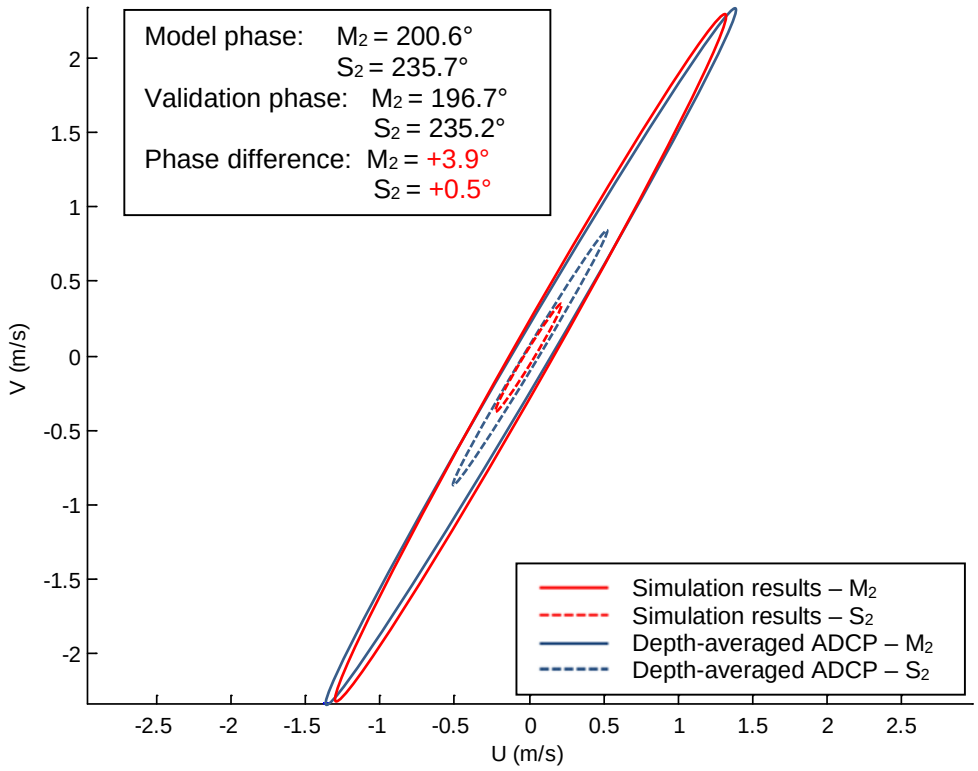

Figure 7.5 Tidal stream ellipses relating to the RDI ADCP deployment in area T61 (validation data) and the model output at the same location.

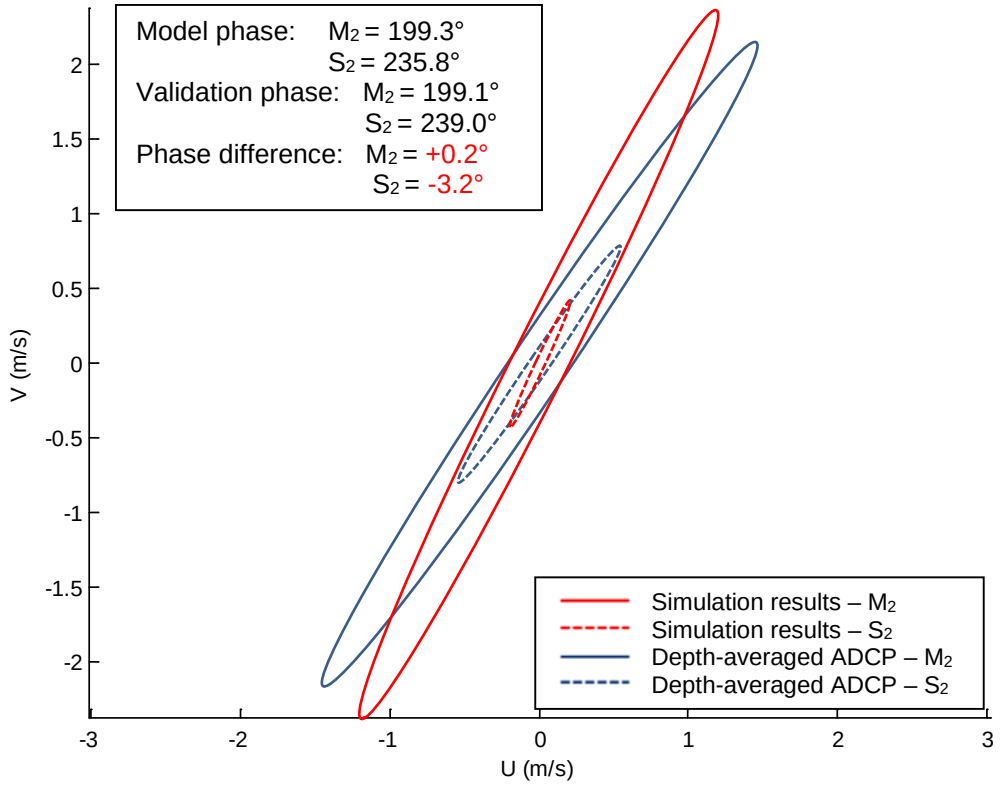

Figure 7.6 Tidal stream ellipses relating to the AWAC ADCP deployment in area T61 (validation data) and the model output at the same location.

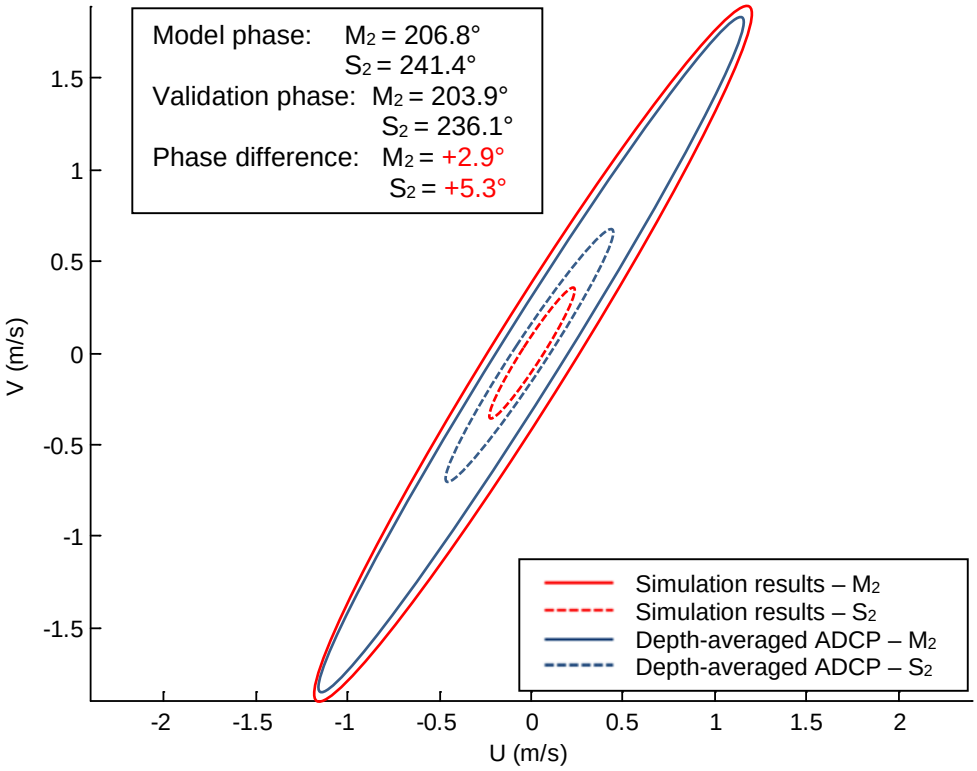

Figure 7.7 Tidal stream ellipses relating to the RDI ADCP deployment in area T75 (validation data) and the model output at the same location.

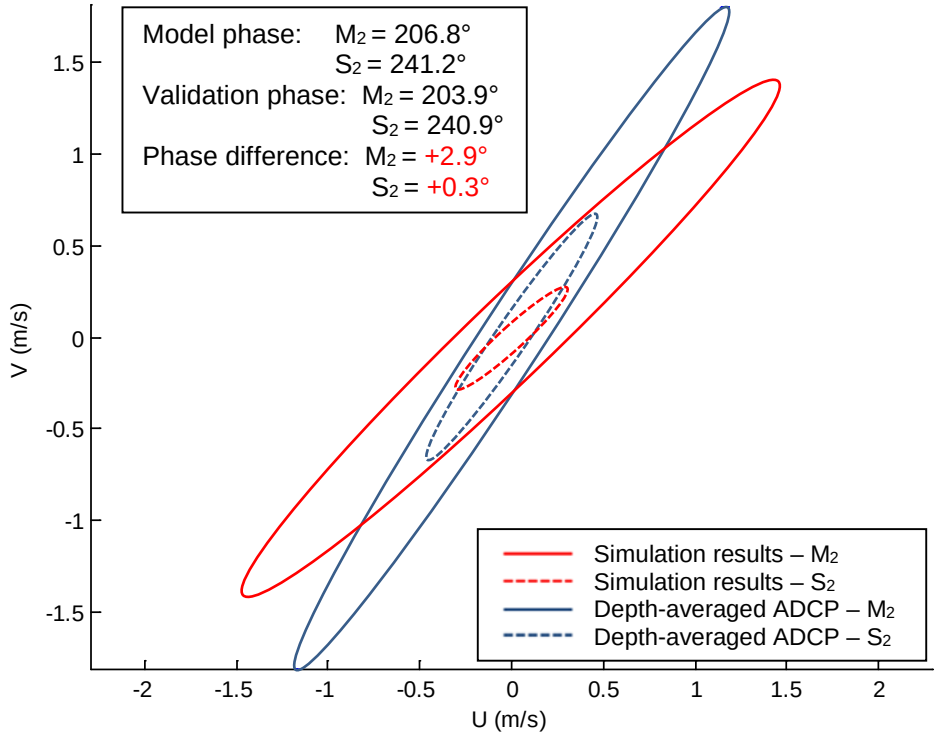

Figure 7.8 Tidal stream ellipses relating to the AWAC ADCP deployment in area T75 (validation data) and the model output at the same location.

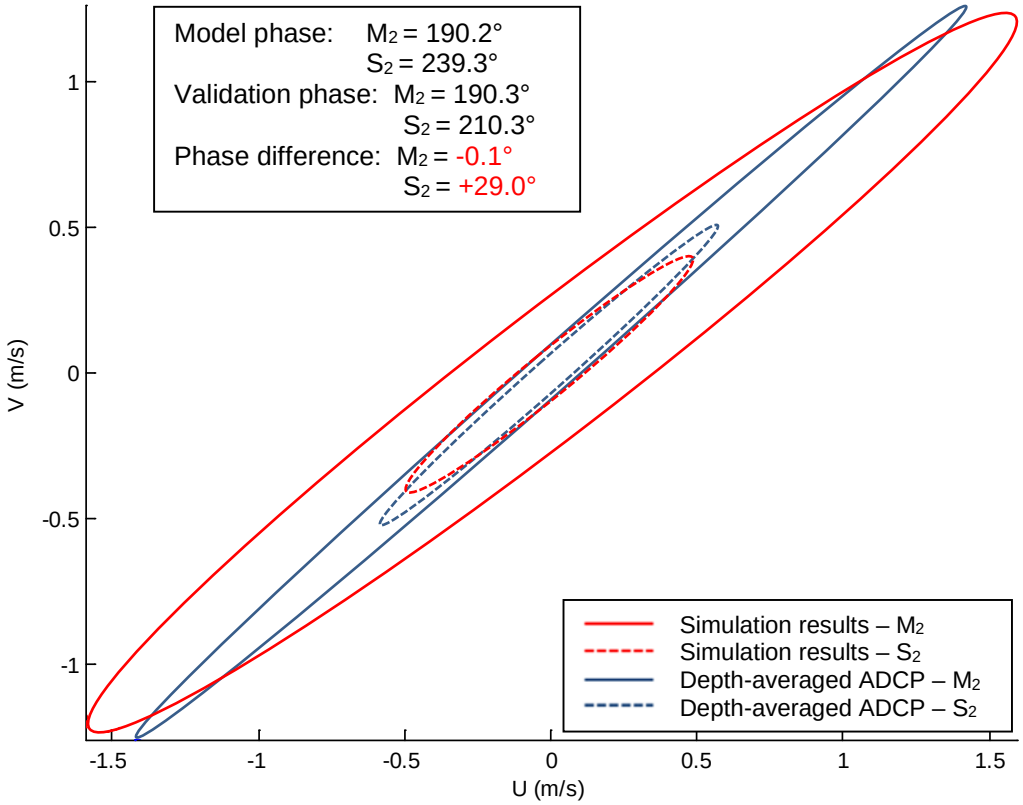

Figure 7.9 Tidal stream ellipses relating to the AWAC ADCP deployment in area T74 (validation data) and the model output at the same location.

Tidal stream – tidal diamond

Hourly velocity information for the Admiralty tidal stream diamond 2669E located in the Race of Alderney was reconstructed using the standard Admiralty method and then harmonically analysed (see Figure 7.3 for diamond location). Table 7.3 displays the key parameter differences between the model outputs and validation data. Tidal stream ellipses relating to both the reconstructed tidal diamond information and baseline model outputs are plotted in Figure 7.10.

Table 7.3: Major axis, phase and inclination differences between modelled and real-world tidal stream velocity datasets for M_2 and S_2 at Admiralty tidal diamond 2669E.

	M_2				**S_2**			
Tidal diamond	Major axis (m/s)	(%)	Phase (degrees)	Inclination (degrees)	Major axis (m/s)	(%)	Phase (degrees)	Inclination (degrees)
2669E	0.11	5.9	9.9	-5.0	-0.09	-13.4	3.7	-6.2

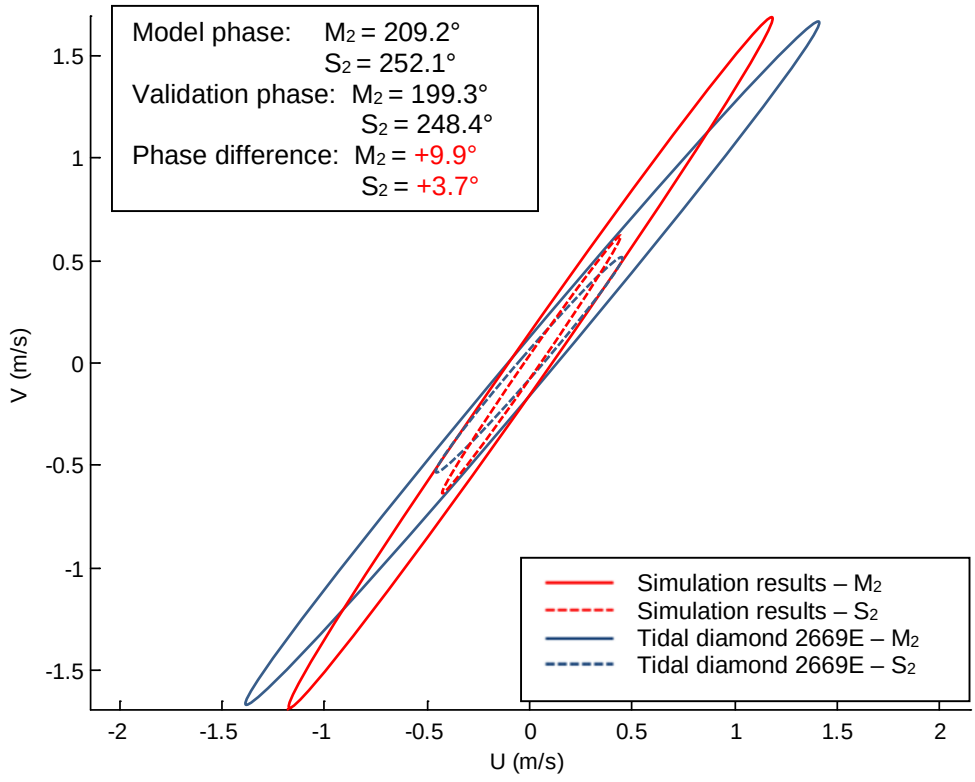

Figure 7.10 Tidal stream ellipses for Admiralty tidal diamond 2669E (validation data) and the model output at the same location.

The model performs well across all ellipse parameters with all differences < ±10%/10° with the exception of the S2 *major axis* which undershoots the model by 13.4%.

7.1.5 Summary

The following *differences* between the model and the validation data have been achieved:

- RDI ADCPs in T61 and T75: All parameters < ±5% / 5°
  (with the exception of S_2 *major axis* values)
- AWAC ADCPs in T61 and T75: All parameters < ±10% / 10°
  (with the exception of S_2 *major axis values and the T75 inclination*)
- AWAC ADCP in T74: All parameters < ±10% / 10°
  (with the exception of S_2 *major axis* values)
- Tidal elevation at Cherbourg and Jersey: All parameters < ±10% / 10°
- Tidal diamond 2669E: All parameters < ±10% / 10°
  (with the exception of S_2 *major axis* values)
- Tidal elevation at 8 ports: All parameters < ±10% / 10°
  (Concarneau, Saint-Malo, Le Havre, Dover, Newhaven, Newlyn, Cromer and North Shields)
- Tidal elevation at 2 ports: All parameters < ± 20% / 20°
  (Dunkirk and Whitby)
- Tidal elevation at 2 ports: All parameters < ± 35% / 35°
  (Bournemouth and Weymouth)

7.2 Baseline model

Mean and maximum velocity magnitudes from the baseline model are displayed in Figure 7.11 (a-b). A zone of high mean velocity can be seen to stretch across the Alderney Race from North-West-West to South-East-East. On the Alderney side the highest mean values occur in the vicinity of the two Race Rocks (Figure 6.1) with a maximum mean value of 2.27 m/s. Maximum velocity values follow a similar trend (Figure 7.11 (b)) with a peak value of 4.36 m/s in the same region. It is well established that the highest velocity values in this region occur during the much stronger ebb-tide when the tidal currents curve South into the Alderney Race from above the Cherbourg Peninsula (see Admiralty Tidal Stream Atlas NP 264). This is verified in Figure 7.11 (b) by the well-defined maximum-velocity deficits shed to the South-West of the two Race Rocks. Particularly clear is a 'jet' of high maximum values that are caused by flow acceleration between the rocks. The same feature can be observed in the mean values although it less well-defined.

The cube-root-mean-cube speed is a useful metric for characterising the energy capture potential at a site (Blunden and Bahaj, 2006). Periods of flow speed close to zero (i.e. zero power generation) are incorporated due to the averaging process. The method quantifies power density and is a more realistic guide for potential power output than maximum current speed.

Figure 7.12 plots the cube-root-mean-cube speeds for the baseline model run and includes array footprints for context. A high power density region is apparent on the Alderney side of the race where $\sqrt[3]{\langle \bar{U}^3 \rangle} > 1.25$ m/s .The array footprints in T47-49 and T61-63 are coincident with this region with the power density decreasing to the South-West (for the arrays adjacent to the South Banks).

(a) Mean velocity magnitudes

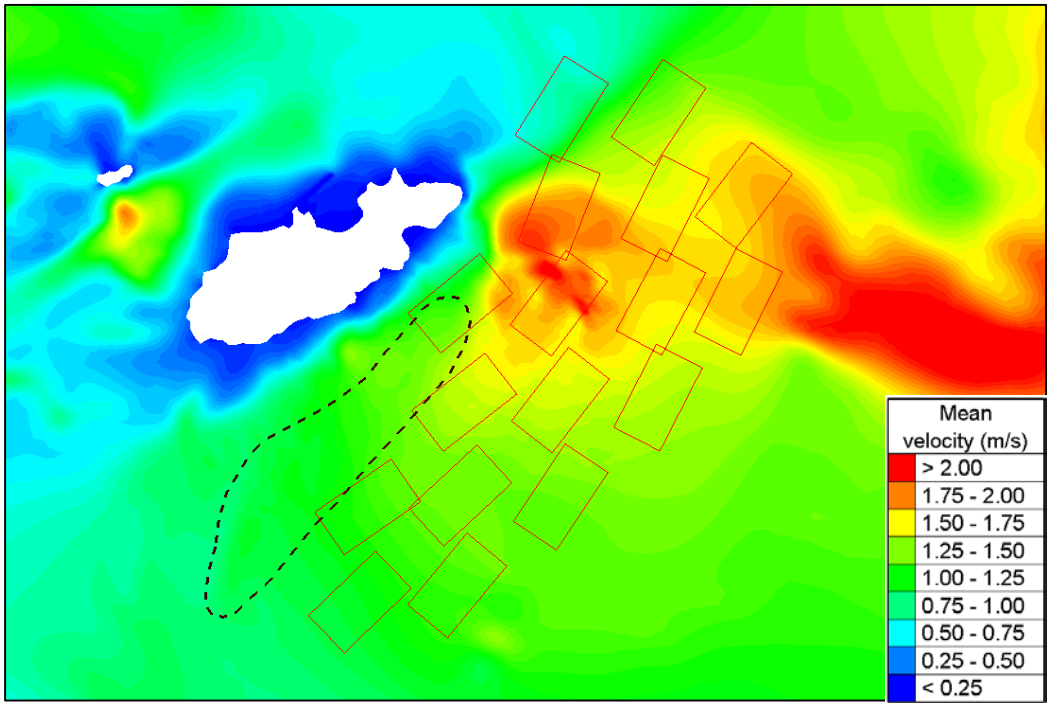

(b) Maximum velocity magnitudes

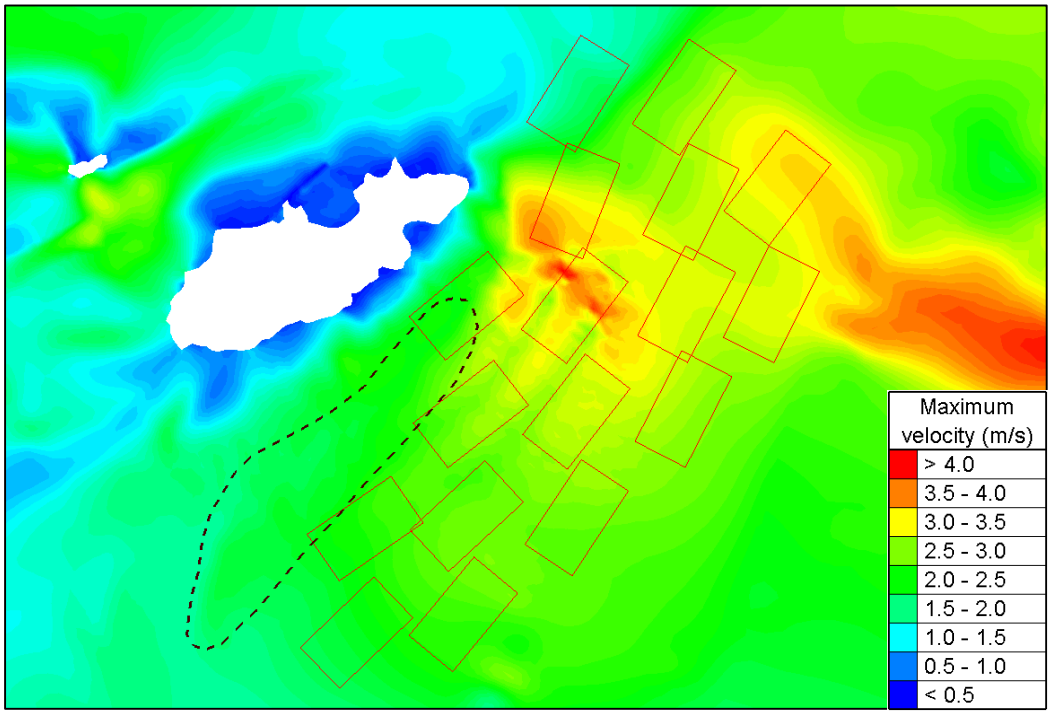

Figure 7.11 Baseline model outputs for the 14.8 day spring-neap model run. Array footprints included for reference (see Figure 8.3 for T-block numbers) and the South Banks limits marked by the dashed line.

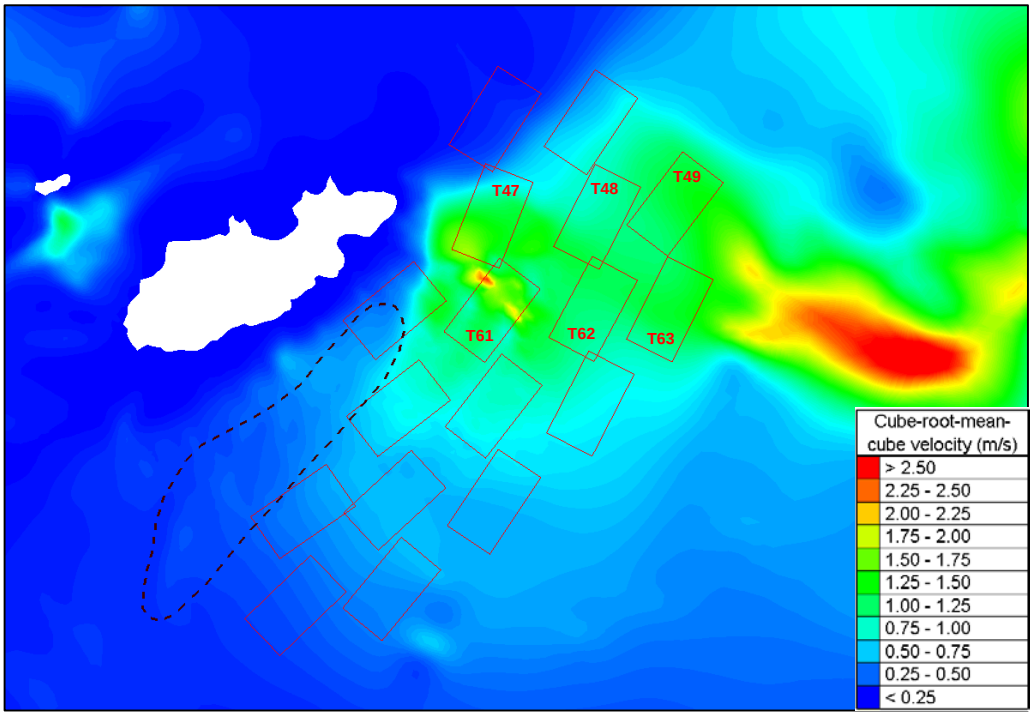

Figure 7.12 Cube-root-mean-cube speeds for the baseline model. Power is proportional to the flow speed cubed (U^3) and the cube-root-mean-cube speed ($\sqrt[3]{\langle \bar{U}^3 \rangle}$) has been proposed as a metric of the available power density at potential extraction sites (Blunden and Bahaj, 2006). Array footprints included for reference and the South Banks limits marked by the dashed line.

Figure 7.13 shows the residual current for the baseline model run. A large, clockwise eddy is apparent with its centre located around 1km South-East of the South Banks. This is the residual manifestation of the eddy shed from the headland tip that propagates across the North-Eastern portion of the sandbank (see section 5.1). In more complex tidal flows the residual current doesn't accurately reflect resultant sediment transport. Velocities beneath the critical velocity for sediment transport ($\bar{U}_{cr}$) will not contribute to the resultant rates. The non-linear relationship between current speed and transport rates also needs to be accounted for in the averaging process.

Figure 7.14 plots the *residual sediment transport* for the baseline case. Velocities at each time step are converted to transport rate values using the Soulsby-Van Rijn total-load formula (section 6.3) and then averaged across time to produce residual transport vectors. The impact of the propagating eddy is apparent with the 'centre' of the residual transport eddy located over the South-Eastern flank of the South Banks. Residual transport rates are very high in the region immediately West of the Race Rocks.

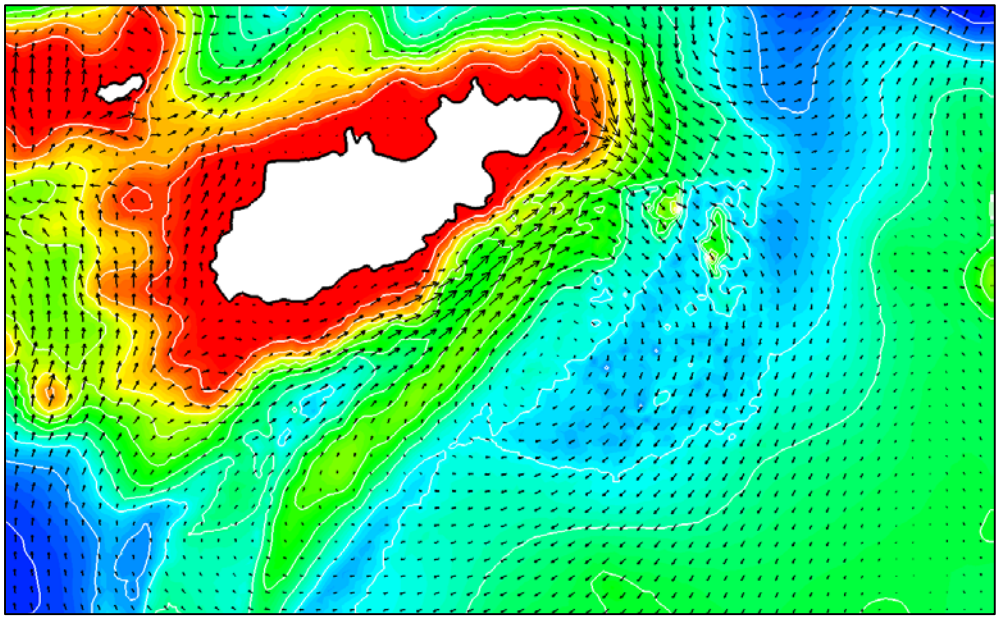

Figure 7.13 Residual current for the baseline model. Vector averages of model velocity outputs are mapped onto a rectilinear mesh (i.e. arrows do not imply mesh resolution). Water depth contours spaced at 5m intervals included for context.

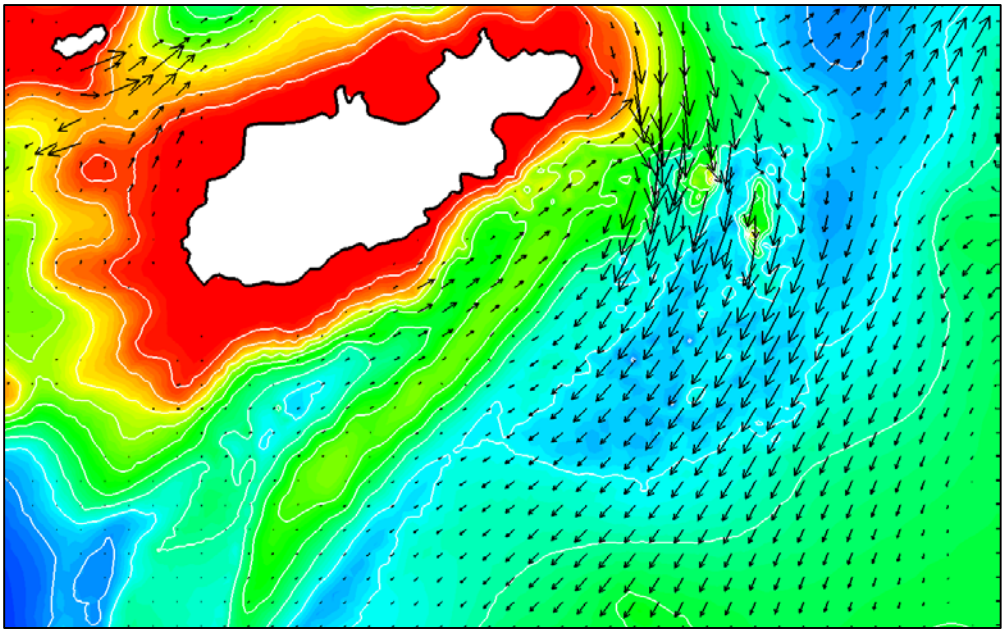

Figure 7.14 Residual sediment transport for the hydrodynamics-only baseline model. Velocity vectors were combined with the Soulsby-Van Rijn total-load transport formula (Soulsby; 1997) to produce instantaneous sediment transport rate vectors for each time-step. Rates were then vector-averaged across the 14.8 day run-period to produce the residual. Sediment parameters used for the calculation are the same as those used for the sediment model (see chapter 5.2). Values mapped onto a rectilinear mesh (i.e. arrows do not imply mesh resolution).

Bedload transport rates (q_b) calculated from the sandwave migrations in section 5.3 are compared against the averaged residual sediment transport vectors (q_t) from our model in Table 7.4. Comparisons were performed for four regions located on the ebb-dominant Southern flank of the South Banks for which repeated bathymetry data is available. Figure 7.15 shows the location, extent and orientation of these four regions. Bedload transport components from the sandwave migration analysis are extrapolated to calculate rough estimates for the equivalent total-load components. q_b values are assumed to be an underestimate by a factor of 1.5 (section 2.7.4) and it is also estimated that $q_s \approx 2.7 q_b$ (see sections 5.3 and 6.3.2) therefore $q_t = 5.6\ q_b$ is used to estimate total-load.

Table 7.4: Comparison of model output transport residuals with real-world values for bedload transport calculated from sandwave migrations. *qb* values from sandwave migration analysis are scaled to equivalent total transport rates to aid comparison.

Analysis region	Sandwave migration analysis						Sediment transport residual	
	Height	Migration		Direction	q_b	q_t	q_t	Direction
	(m)	m/50 days	m/day	(deg.)	m^2/day	(q_b * 5.6)	m^2/day	(deg.)
1	3.28	47.0	0.94	251.6	**0.99**	**5.49**	**3.22**	344.0
2	3.96	30.4	0.61	256.4	**0.77**	**4.28**	**2.97**	284.8
3	4.58	21.8	0.44	257.6	**0.64**	**3.55**	**4.00**	250.8
4	7.58	16.0	0.32	241.3	**0.78**	**4.32**	**4.15**	241.5

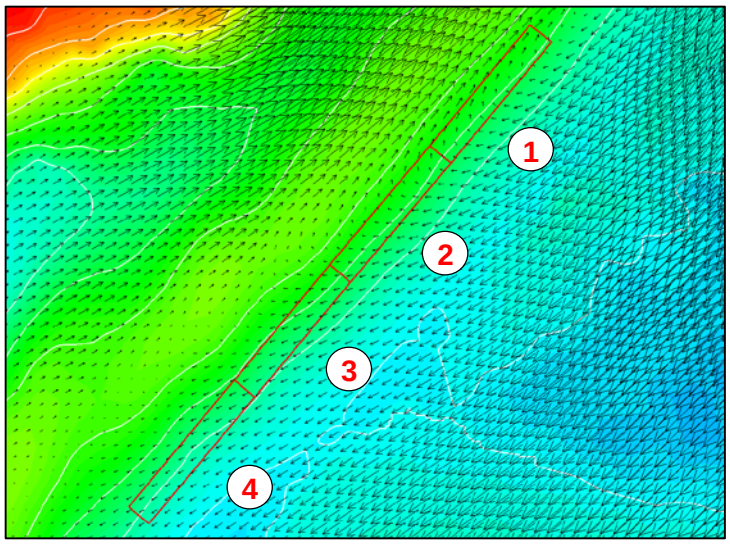

Figure 7.15 Limits of the four analysis regions across which bedload transport rates (from sandwave migrations) and total load transport rates (residual sediment transport calculated from model outputs) are compared using spatial averaging. Residual sediment transport for the model is included (vectors mapped onto a rectangular mesh).

Sediment transport rates for our model match those inferred from the sandwave migrations very well for analysis region number 4 with almost identical residual direction and very similar total-load values observed. Differences in region 3 are also fairly small. In analysis region 2 the directionality of the residual is wrong by around 30° and the magnitudes an under prediction by ~30%. Discrepancies are at a maximum in region 1 where the directionality is almost 100° out and the magnitudes an underestimate by ~40%. The increasing disparity towards the North-East of the bank appears to be due to the effects of the residual eddy and its specific location relative to the bank crest (see below). There are a number of problems with such a comparison (likely difference of directionality between q_b and q_s residuals, varying proportions of q_s and q_b) but we feel that the method represents the only means we have for checking the realism of the model transport rates. On these terms the model appears to perform very well for analysis regions 3 and 4, moderately for region 2 and badly for region 1.

Figure 7.16 (a-b) shows zoomed residual sediment transport plots for the South Banks (vector spacing is reduced to enhance spatial variations). A region of transition lies lengthwise along the South Banks with North-Easterly residuals between the bank and Alderney. To the South-East of the bank residuals are in the opposite direction (to the South-West) with increasing velocities towards the tip of the sandbank. This pattern supports the conclusions presented in chapter 5 relating to the South Banks morphology and further attests to the validity of the baseline model. Sand is circulated in a clockwise manner around the bank due to opposing transport residuals on opposite sides of the crest. A transport convergence zone lies along the centre of the bank. Of particular interest is the pattern of residuals at the South-Westerly end of the South Banks which appear to almost exactly reproduce the transport pathways suggested in chapter 5. The triangular tip of the bank is largely ebb-dominant with the transition to flood dominance occurring roughly 1.5km north of the sandbank tip. The region of bed-load convergence is not totally coincident with the sandbank crest for the North-Eastern portion of the South Banks (it is offset by up to 400m). This is not likely to be the case in reality and the discrepancy could be due to a number of factors. The two most likely causes are bathymetric inaccuracies at the headland (effecting flow around the headland and eddy propagation) and the simplicity of the sediment formula used to calculate the residual (secondary flows are not included, validity ranges of the transport formula, grain-size variation).

Bed-level evolution outputs for the 3 month baseline sediment model are superimposed on depth-contours in Figure 7.17. Significant bed level evolutions are observed with erosion occurring around the sandbank perimeter and deposition located in regions along the sandbank crest. Erosions depths are $\leq$ 1.25m for the majority of the sandbank but there are very large erosions of up to 2.8m along the perimeter of the North-Eastern third of the bank. Depositions are typically $\leq$ 0.75m for most of the sandbank and there is a large region where up to 1m of sand is deposited at the South-Western tip of the bank. A region of depositions of 5-39cm can be observed roughly 2km to the South-West of the sandbank. This shows that the sandbank is failing to retain some of the mobile sand within its limits (i.e. the rigid-bed region specified in section 6.3).

The most extreme bed-level changes observed suggest that our model is not adequately simulating the South Banks dynamics or any associated equilibrium states. One important factor could be the lack of sediment supply to the sandbank in our model (especially along the ebb-dominant region of the bank where the maximum erosions are observed). The rigid bed formulation stops erosion occurring beyond the bank limits therefore sediment supply to the bank is non-existent. Although potentially a factor, this doesn't explain the smaller but consistent erosions of up to 1.25m observed along the foot of both sides of the bank. The erosions suggest that the model is not accurately predicting sediment movement in these regions. Possible explanations include the limitations of using a 2-dimensional model, the depth-validity range of the Soulsby-Van Rijn formula (1-20m), the particular formulation used for defining skin friction values in SISYPHE and potential grain-size variation across the width of the bank. Having said this, the sediment model does simulate a number of realistic morphological behaviours: mobile sand collecting along the sandbank crest; sand accumulating at the South-Western end of the sandbank leading to sandbank extension; equalisation of bed levels lengthwise along the sandbank due to rhythmic features still present after spatial averaging of the sandwaves; sand lost from the sandbank to the South-West during the stronger ebb-tide, perhaps representing the transport of finer sediment away from the bank.

The key benefit of assessing array impacts by calculating the *difference* between baseline and energy-extraction cases lies in the cancellation of modelling errors. Although energy-extraction may cause the most un-realistic bed-level evolutions to be attenuated erroneously, we feel that the investigation of array impacts upon evolutions can still provide useful insights.

(a) North-East section of the bank

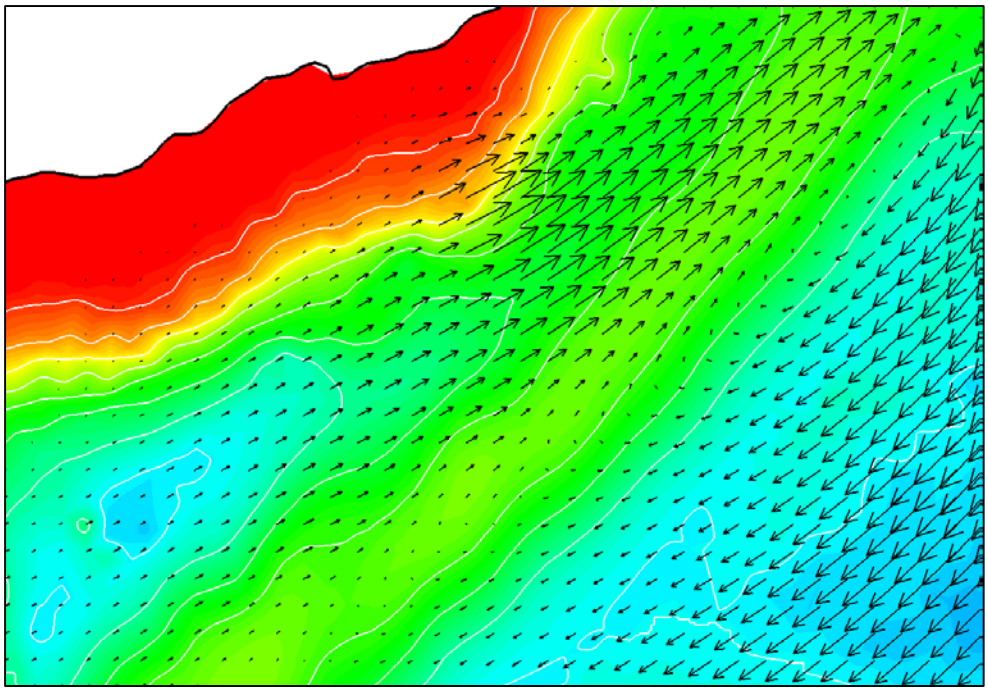

(b) South-West section of the bank

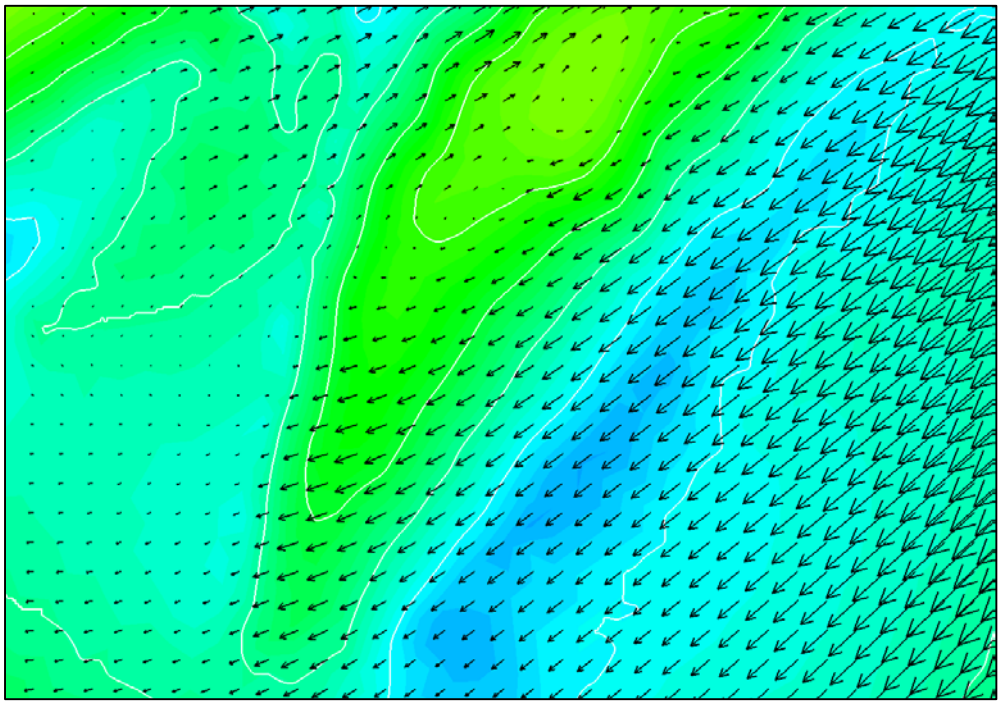

Figure 7.16 Residual sediment transport over the South Banks for the hydrodynamics-only baseline model (see Figure 7.13 for details). Values are the same as for Figure 7.12 but with more regularly spaced vectors.

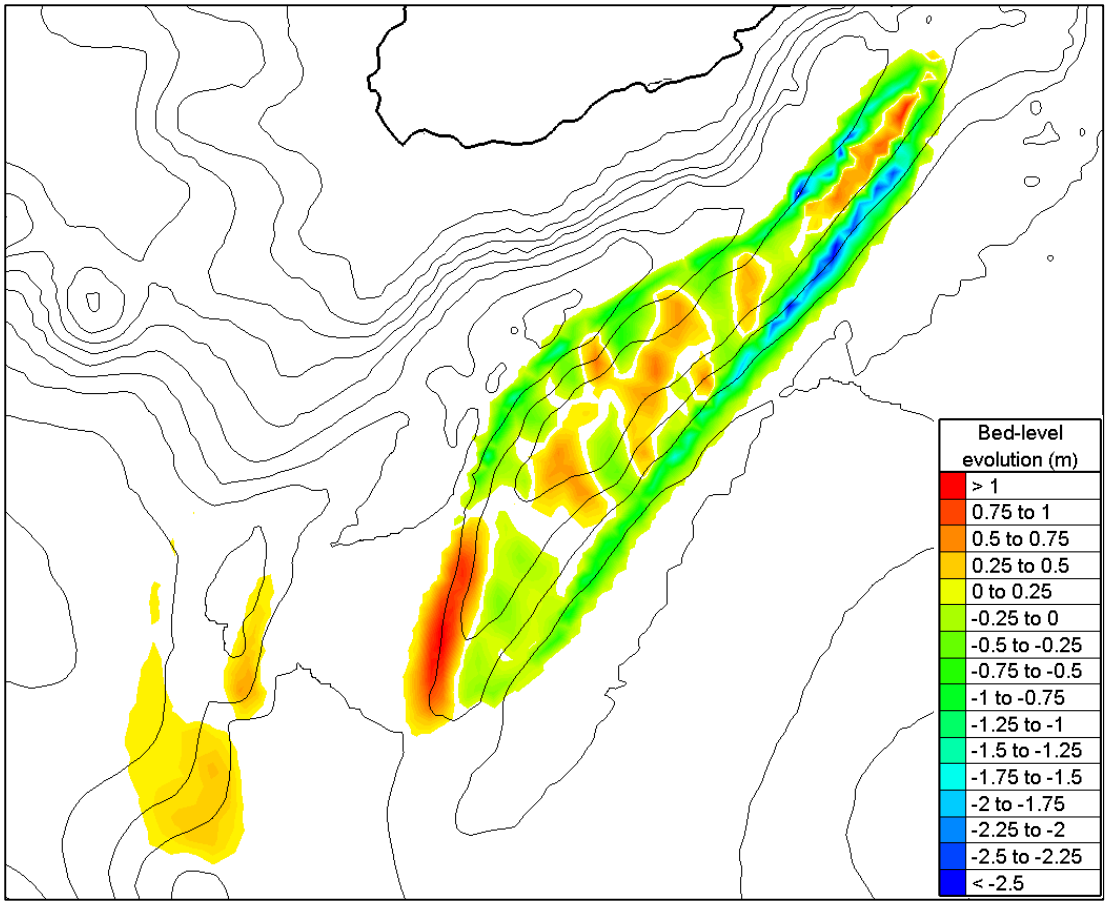

Figure 7.17 Bed-level evolutions output from the 90-day baseline sediment model (TELEMAC-2D coupled with SISYPHE). Evolutions < ±5cm are white. Bathymetric contours at 5m depth-intervals included for context.

7.3 Array impacts – currents

The extraction of energy from tidal flows causes progressive flow-deceleration across the length of a tidal-device array. Each row of turbines further reduces the kinetic energy of the flow, a process which is simulated in the model using an added drag force (section 2.4). Figure 7.18 plots baseline and T74 energy-extraction velocity vectors for the spring ebb-tide. Differences between the vectors represent the instantaneous impact of the array at this point in time. The velocity deficit decreases lengthwise along the array resulting in a difference of ~0.6m/s immediately downstream.

Flow accelerations of up to 0.3 m/s can also be observed to the North-West of the array (over the South Banks), with maximum accelerations of ~ 0.5m/s occurring close to the centre of the propagating eddy. Flow acceleration *around* arrays is typically of much smaller magnitude to the deceleration produced immediately *downstream* of an array. Figure 7.19 shows the *difference* in velocity magnitude between the baseline and T74 extraction scenario as a contour plot. Flow-increases to the North-West of the T74 array are particularly high (compared to typical accelerations of ~0.1 m/s around arrays in an unbounded flow). This is due to the way in which flows *reinforce* the clockwise circulation of the eddy to the South of the eddy centre. Above this region there is another region of flow deceleration where acceleration around the array *counteracts* the clockwise motion of the eddy.

Energy extraction in T74 can be seen to produce velocity deficits of >0.2 m/s up to 9km downstream from the array as seen in Figure 7.19. Equivalent plots using the same colour-scale as Figure 7.19 are presented for each 300MW extraction scenario in Figure 7.20 to allow inter-scenario comparison. The downstream profile of the velocity deficit behind the arrays appears to be consistently related to their lateral position relative to the South Banks. The deficit downstream from T47 is transported along a curved path passing over the middle of the South Banks. Deficits downstream from T48 follow a less curved path and those downstream from T49 curve a little in the opposite direction. The same pattern can be observed along rows T60-T63, T74-T76 and T85-87. This makes intuitive sense if the large ebb-flows in this region are understood as acceleration around a blockage in the flow in i.e. the island of Alderney.

The T35 and T36 arrays affect flow speeds less than many of the other arrays. This is because flow-velocities are smaller in this region resulting in decelerations and accelerations of < 0.2 m/s.

Lateral array location appears to significantly affect the magnitude of the downstream velocities in some cases. The T86 and T94 deficits are larger than the T85 and T93 values respectively. This is related to two factors. Velocities decrease with distance from the Race Rocks region so arrays situated further West are in fact located further downstream (i.e. T85 is further downstream than T86). Potentially more significant, ebb-tide velocity values increase with distance from the sandbank as can be deduced from Figure 7.11. T86 and T94 are therefore situated in a stream of higher ebb-tide velocities (than T85 and T93 respectively) resulting in larger downstream velocity deficits.

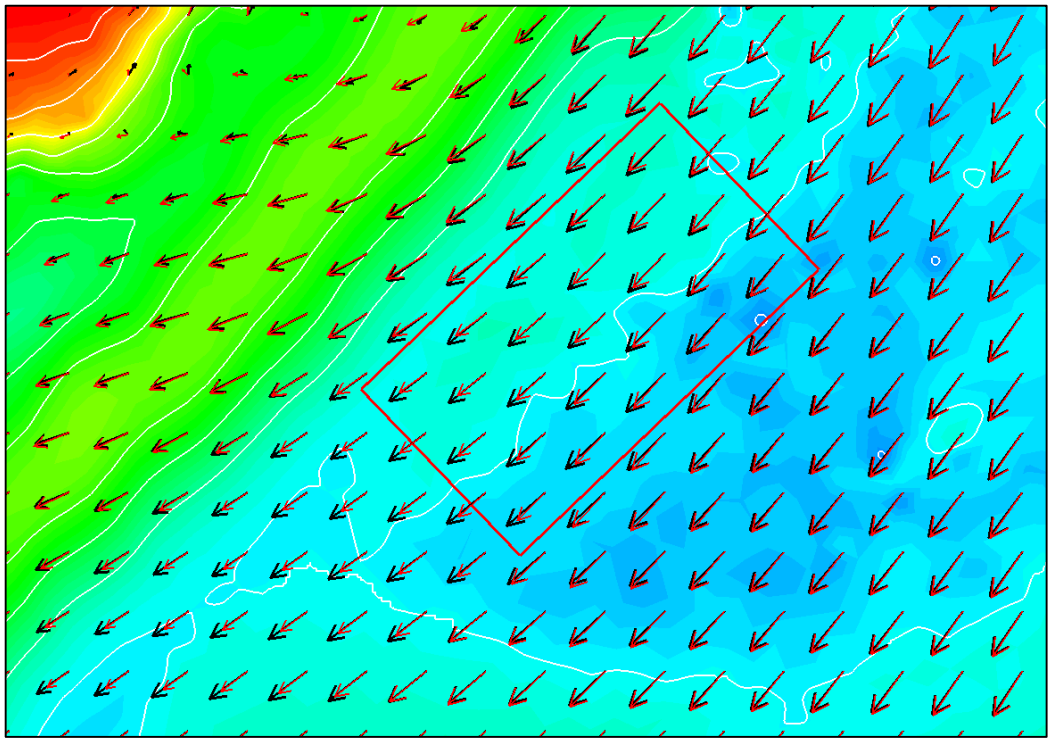

Figure 7.18 Velocity values during the spring ebb-tide for the baseline (black arrows) and T74 energy-extraction (red arrows) model-runs. T74 array footprint included.

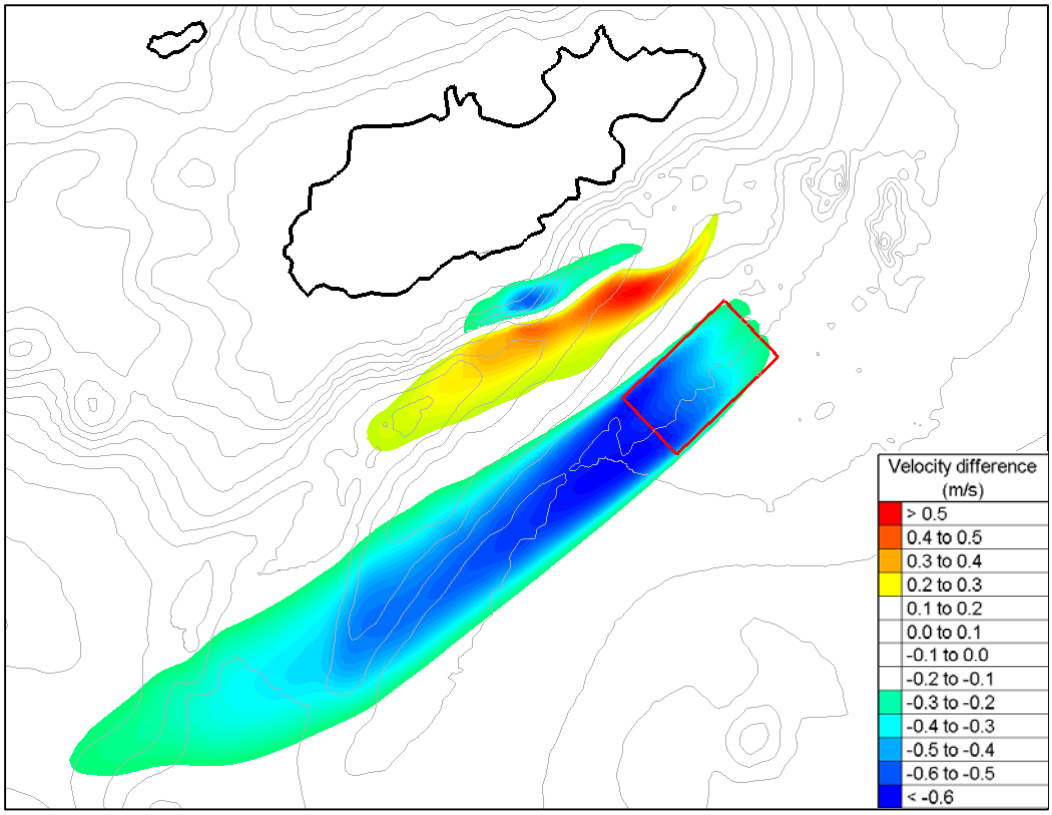

Figure 7.19 Impact upon velocity of energy extraction (300MW) in T74. Contours represent velocity magnitude differences between the baseline and T74 scenario at the peak flow of the spring ebb-tide. Values smaller than ±0.2 m/s are not included.

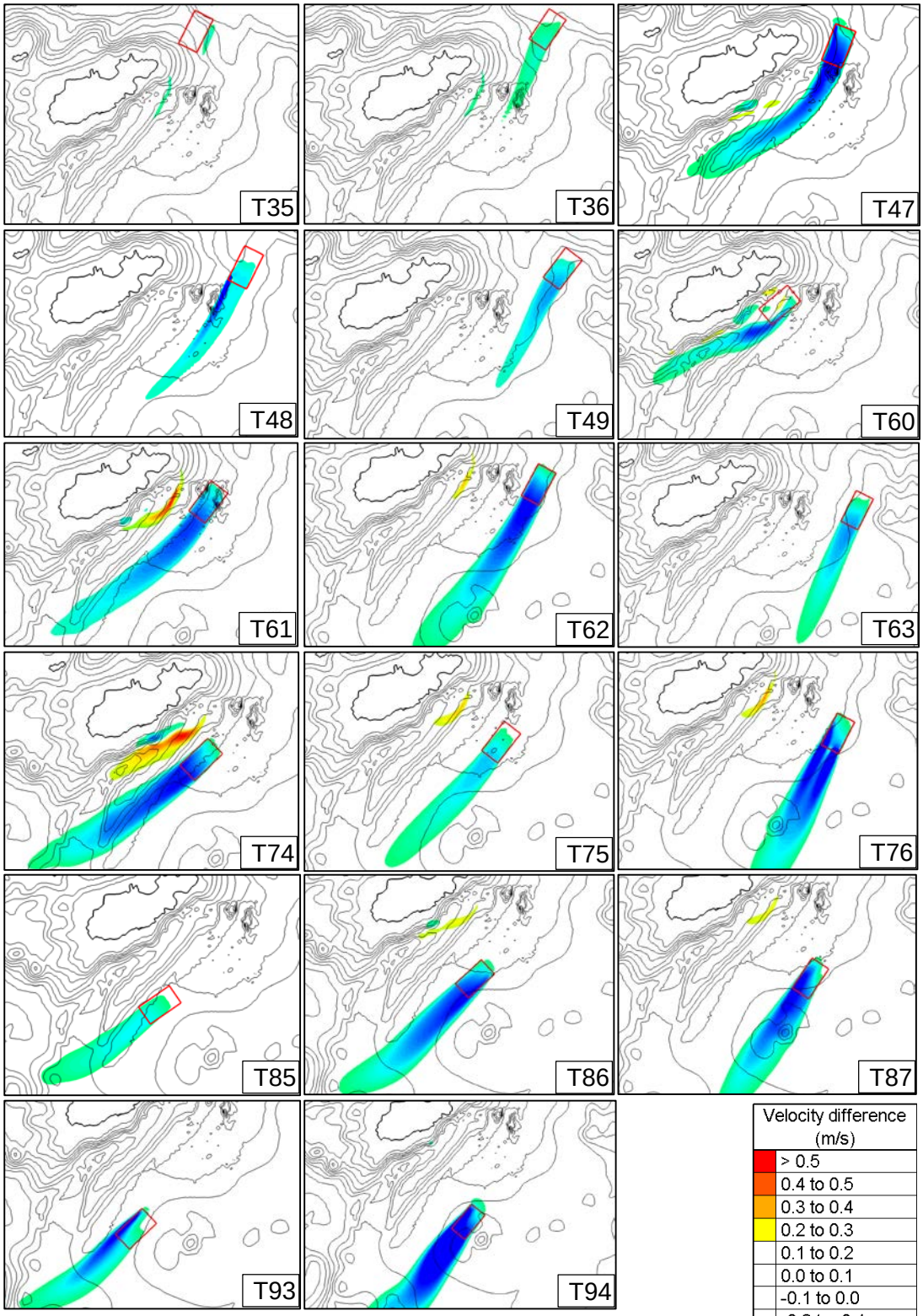

Figure 7.20 Velocity deficits for seventeen 300MW extraction scenarios. Identical colour scales are used to aid inter-scenario comparison. Outputs are all for the same equivalent model-time step and relate to the ebb-spring-tide (the largest tidal-cycle of the model run). Array footprints are hi-lighted in red. Differences < ± 20cm/s not included.

Residual currents for the baseline and T74 energy-extraction scenario are plotted in Figure 7.21. These values represent the average velocity at each node over the whole model run. Velocity decreases downstream of the array on the ebb-tide have changed the directionality such that the new residuals point *towards* the array (rather than following the clockwise eddy residual). A similar effect can be seen to the North-East of the array where decelerations on the flood-tide cause residuals to point towards the array. Cumulative accelerations to the North-West of the array on the ebb-tide (Figure 7.19) have reduced the magnitude of the large North-Easterly residuals in this region, once again counteracting the eddy-type pattern of the baseline residual. The *vector-difference* between the baseline and extraction case are plotted in Figure 7.22 (with magnitudes exaggerated for clarity). This type of plot emphasises the impact of the array on the residual current. The T74 extraction scenario can be seen to attenuate the cumulative impact of the eddy upon the residual current by reducing its rotational magnitude by speeds of up to 0.23 m/s (Figure 7.22).

7.4 Array impacts – residual sediment transport

The same vector-difference method employed for assessing array-impacts upon residual currents (Figure 7.22) can be used to assess impacts upon the residual sediment transport. The resultant transport difference-vectors allow us to interpret how energy-extraction will modify the existing sediment transport pathways.

The South Banks morphology has been described in chapter 5 and confirmed to a reasonable degree by our baseline-model outputs. We can interpret transport vector-differences (array minus baseline) as representing a modification of the real-world sediment transport residuals (as opposed to interpreting them relative to our *baseline* transport residuals). If the difference-vectors point along real-world sediment transport pathways (as determined from sandwave migrations) we can infer that residual sand transport will increase. If they point in the opposite direction it suggests that residual transport rates will decrease. If they veer off to either side we can interpret this as a modification in the direction of residual transport.

The strength of this method lies, again, in the subtraction of outputs from the baseline and energy extraction cases resulting in the reduction of model errors. Even when our baseline sediment transport residuals are not entirely accurate the *difference*

between model-runs allows us to make predictions about changes to the real-world morphology.

The difference in residual sediment transport between the baseline and T86 extraction scenario is plotted in Figure 7.23. The South Banks have been split into zones of ebb and flood dominance (section 5.1) to aid interpretation of the vector-differences. The difference vectors in Figure 7.23 point to the South-West along the ebb-dominant South-Eastern flank of the sandbank suggesting that residual transport rates will increase (also see Figure 5.1). Along the North-Western flood-dominant flank of the sandbank the vector-differences also point South-West away from the headland. This implies that the residual rates will decrease (as sediment transport is in the opposite direction). The magnitudes of difference on both sides of the bank are larger towards the North-East end of bank where the flow is more energetic and sediment transport rates are higher as indicated by Figure 5.1 and Figure 7.23.

For the T74 extraction scenario shown in Figure 7.24 the residual transport differences are significantly larger with a maximum difference of 10.0 m^2/day (occurring near to the sandbank crest adjacent to the array). This corresponds, at this location, to a residual transport rate reduction from 23.8 m^2/day to 16.1 m^2/day and to an anti-clockwise rotation from 53.9° to 44.9°. For this scenario extraction reduces transport rates on *both* sides of the sandbank (i.e. differences are in opposite direction to real-world sand movement) although the pattern is not symmetrical. Such modifications to the residual sediment transport would be likely to have significant impact upon the South Banks morphology and related equilibrium behaviours.

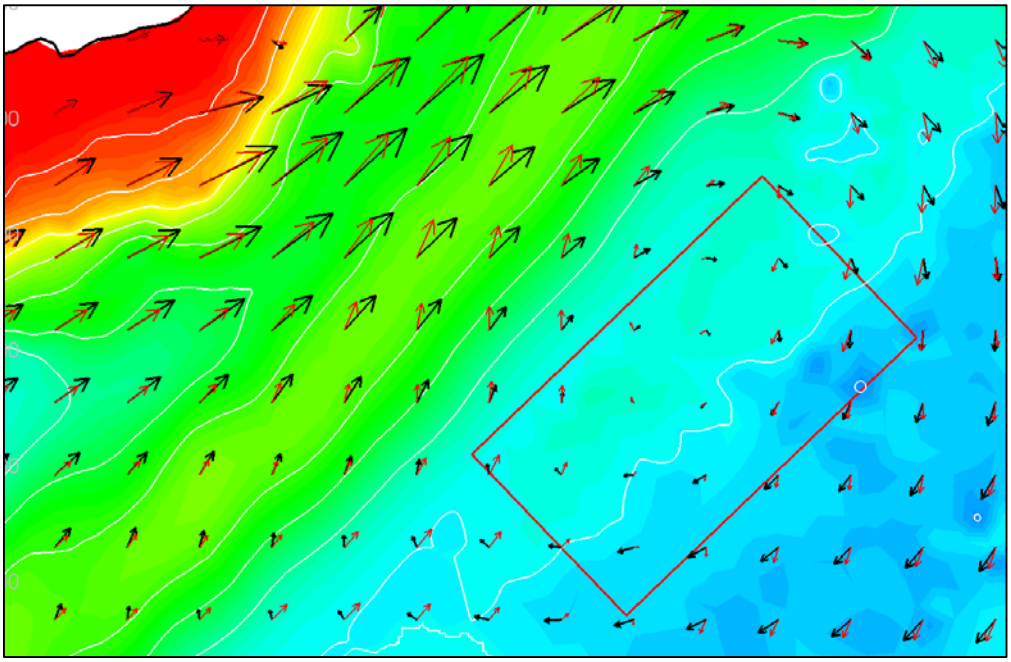

Figure 7.21 Residual current for the baseline model (black arrows) and T74 extraction scenario (red arrows). Velocity values vector-averaged at each node for the duration of the model-runs (14.8 days) and mapped onto a regular mesh. The largest baseline residual current magnitude is 0.91 m/s. Array footprint included.

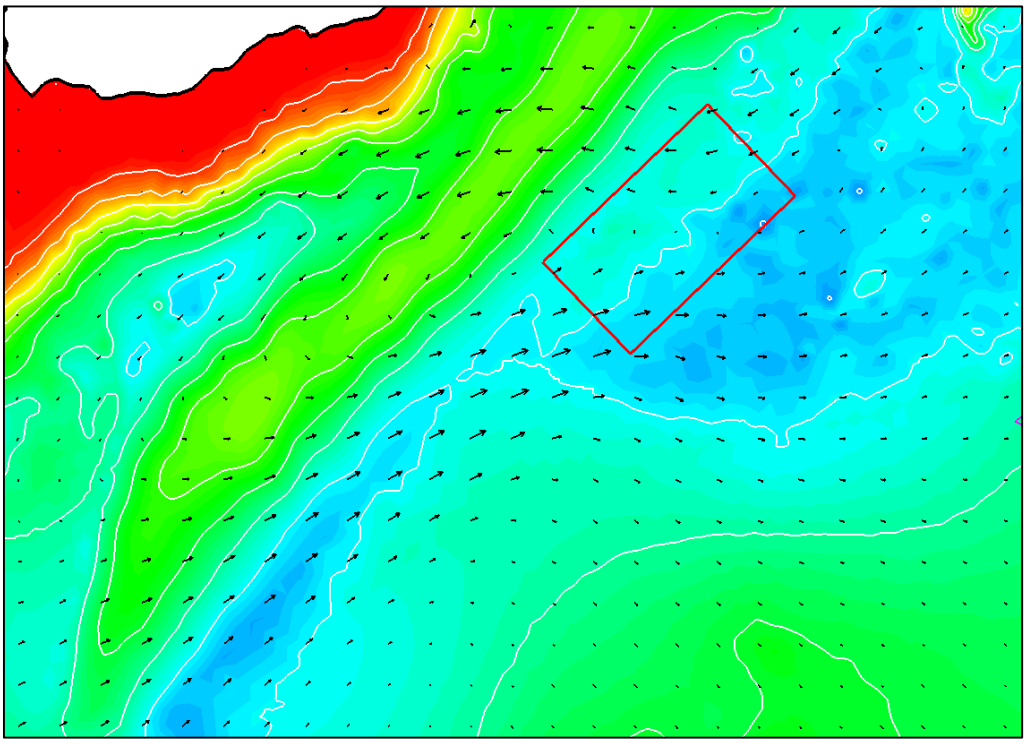

Figure 7.22 Vector-difference in residual current between the baseline and T74 extraction models. The maximum difference in residual magnitude was 0.23 m/s (i.e. the longest arrow).

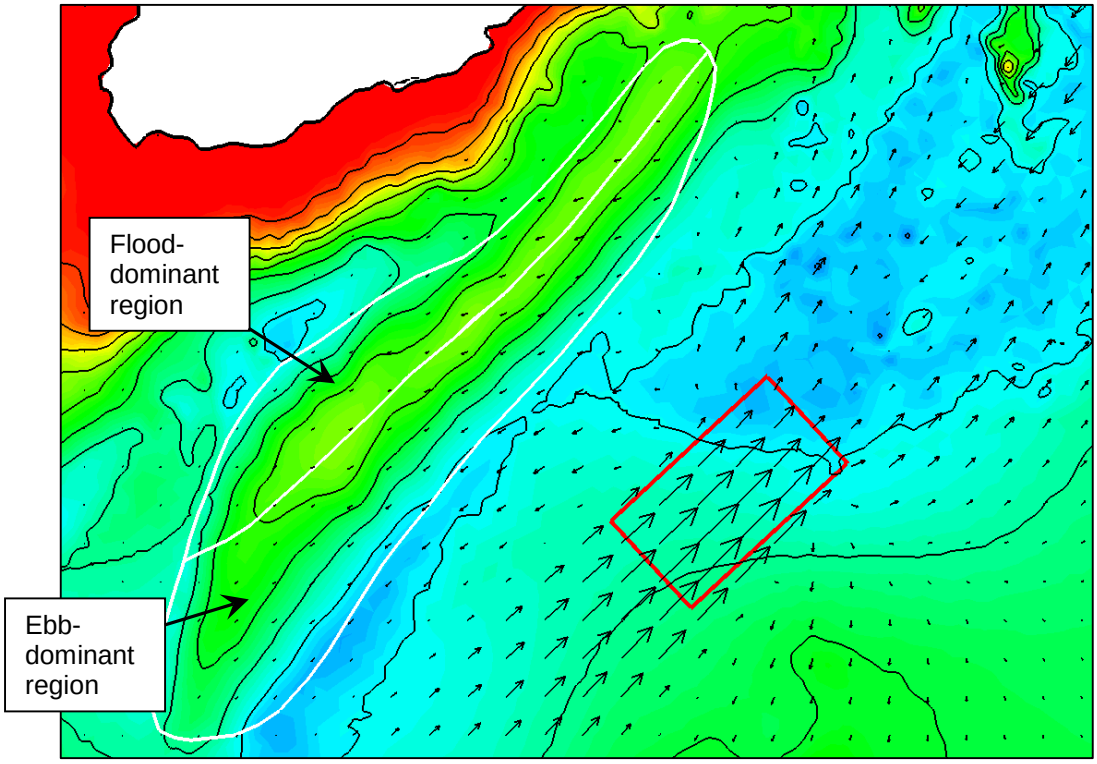

Figure 7.23 Vector-difference in residual sediment transport between the baseline and T86 extraction-scenario models. The regions of ebb and flood dominance over the South Banks are outlined and divided (white lines; see chapter 4). Maximum magnitude of residual difference within the banks region is 4.1 m^2/day. Array footprint highlighted.

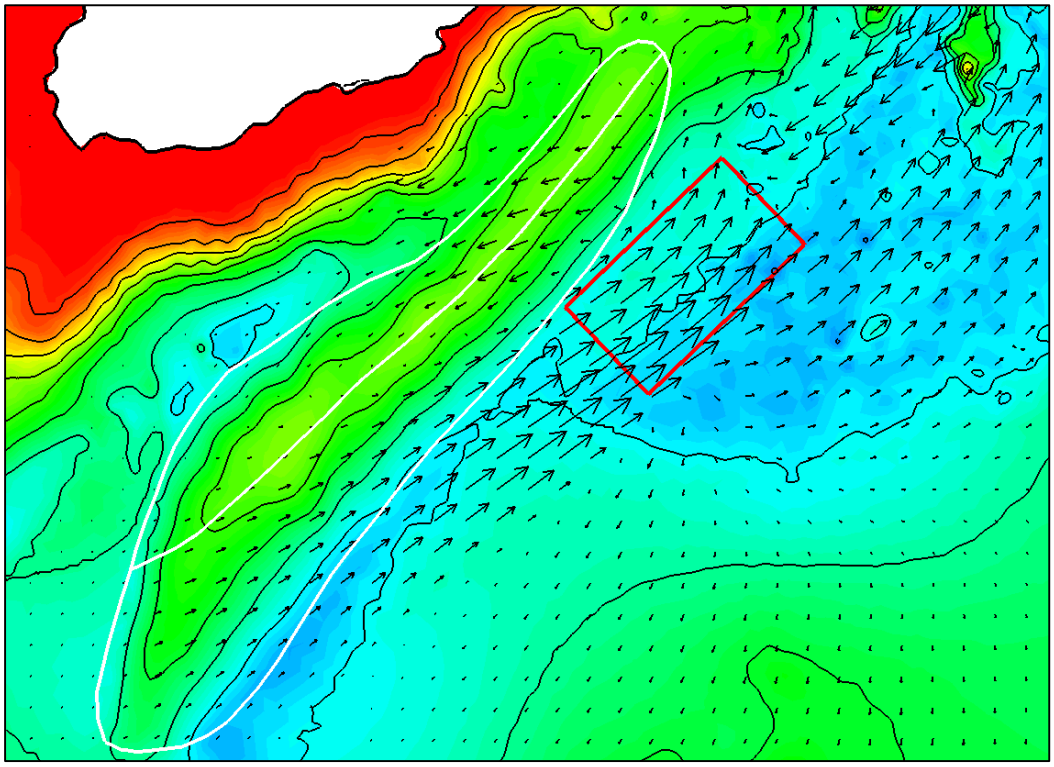

Figure 7.24 Vector-difference in residual sediment transport between the baseline and T74 extraction-scenario models. The regions of ebb and flood dominance over the South Banks are outlined and divided. Maximum magnitude of residual difference within the banks region is 10.0 m^2/day. Array footprint highlighted.

7.5 Array impacts – bed evolution

The difference in 90-day bed-level evolution between the residual and T86 energy-extraction scenario are plotted in Figure 7.25. The impact of the array upon the surrounding flow dynamics resulted in maximum relative depositions and erosions of 1.24m and -1.71m respectively. These values occur at the North-Eastern end of the South Banks and appear to be related to the regions of extreme bed-level change observed in the baseline sediment model in Figure 7.17. Two regions are apparent on opposite sides of the bank with relative erosions occurring on the South-East flank and a larger area of accretion on the North-West flank.

Interpreting the plot within the context of the baseline model a number of dynamics are suggested. The large region of deposition at the South-Western tip of the sandbank experiences additional depositions of ~15cm due to energy-extraction in T86. Erosions seen along the length of the flood-dominant North-Western flank of the sandbank are reduced by 10-40cm with a region of maximum values of 0.9-1.24m

occurring at the North-Eastern end. The consistent erosions along the foot of the South-Eastern flank of the bank are increased in magnitude due to energy-extraction.

The impact of the T86 array upon bed-levels can be explained as a function of the differences in residual sediment transport plotted in Figure 7.23. Increases in transport rates along the South-Eastern, ebb-dominant flank of the bank increase erosion and transport additional sand to the well-defined deposition zone at the sandbanks South-Western tip. Transport rates on the North-Western, flood-dominant flank of the bank are reduced because the residual transport difference-arrows point in the *opposite* direction to the baseline transport residuals. This leads to a reduction in erosion rates and an *increase* in bed-level relative to the baseline model.

Figure 7.26 shows how energy extraction in T74 leads to much larger bed-level differences relative to the baseline case than the T86 scenario. In contrast to the T86 scenario the large deposition zone at the South-West of the sandbank sees less deposition than baseline case. The region immediately downstream of the T74 array on the ebb-tide sees a reduction in erosion rates (due to flow deceleration) and a subsequent relative increase in bed-levels. Flow acceleration around the North-Western side of the array (ebb-tide) leads to increased erosion on the near-side of the bank and reduced erosion on the opposite side.

Reasons for these variations can be inferred by consulting the T74 residual transport vector-differences plot in Figure 7.24. It can be seen that erosion rates are decreased along the South-Eastern foot of the sandbank leading to relative increases in bed level and less sand being supplied to the deposition region at the tip of the South Banks. Increased residual transport rates immediately adjacent to the T74 array (due to flow accelerations on the ebb-tide) increase erosion rates significantly and deposition rates on the opposite side of the sandbank.

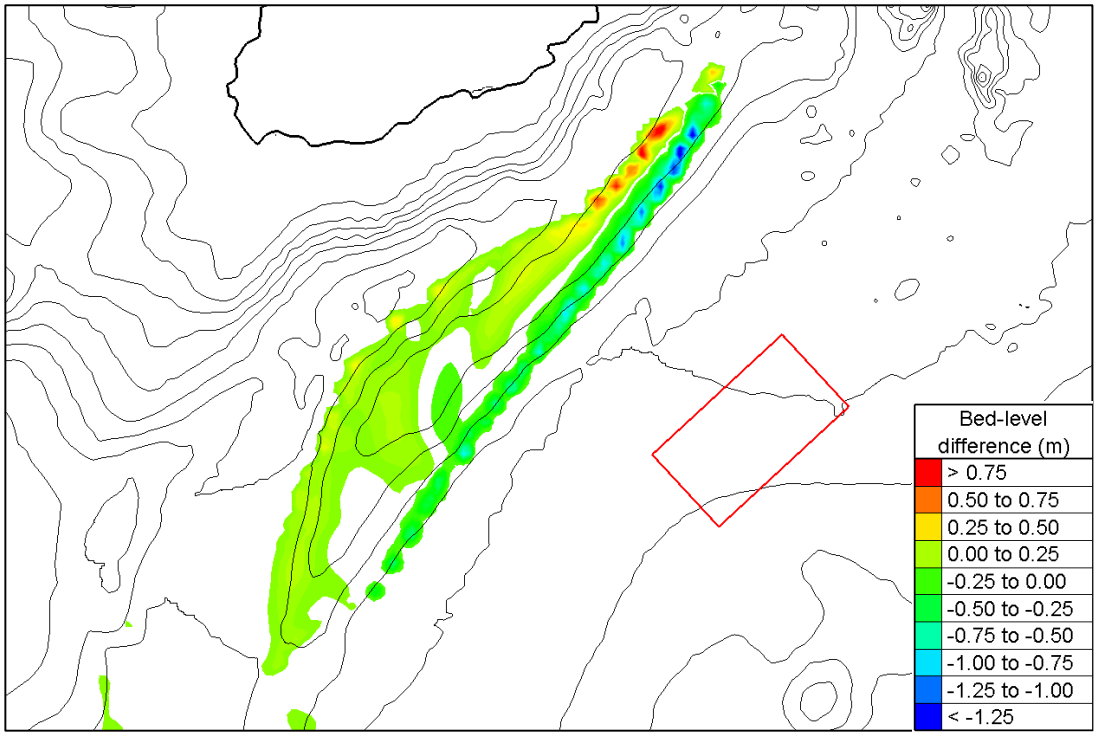

Figure 7.25 Difference in bed-levels between the baseline and T86 extraction scenario for the 90-day sediment model-run. Evolutions < ± 10cm not included. Array footprint included.

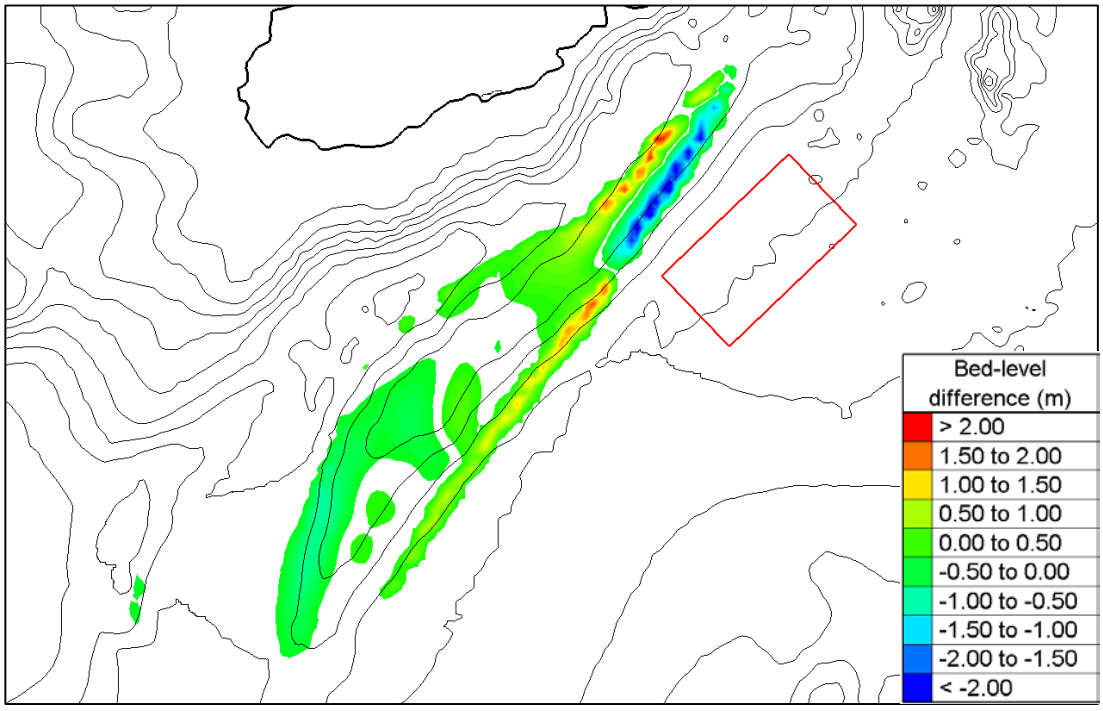

Figure 7.26 Difference in bed-levels between the baseline and T74 extraction scenario for the 90-day sediment model-run. Evolutions < ± 10cm not included. Array footprint included.

8 Discussion

8.1 South Banks zonation and processing of outputs

The modelling phase of this study has yielded a large amount of multi-dimensional data relating to multiple scenarios and two genres of model-run (hydrodynamic and coupled sediment transport). A method for processing, condensing and presenting the modelling data has been developed to aid inter-scenario comparisons. The South Banks have been divided into eight zones of equal area across which the 'model outputs' at each mesh node are spatially averaged. Figure 8.1 shows the specification of these eight zones. The 'model outputs' consist of three species of difference-data produced by subtracting baseline and energy-extraction data:

- The difference in **residual current** *(vector difference)*
- The difference in **residual sediment transport** *(vector difference)*
- The difference in **bed-level evolution** *(scalar difference)*

For each extraction scenario, and for each species of difference-data, a spatially-averaged value is calculated for each of the eight zones. This produces 24 values for each of the 17 extraction scenarios (i.e. 24 x 17 = 408 values in total). To make it explicit:

1. Values at each mesh-node are time-averaged for the whole model run
2. A subtraction is performed between the baseline-model outputs and the energy-extraction-model outputs
3. Difference values (see above) at each node are spatially averaged across each of the eight South Banks zones to produce 3 values per zone for each scenario.

The intention is to strike the right balance between generalising about impacts whilst retaining sufficient detail to allow a nuanced analysis.

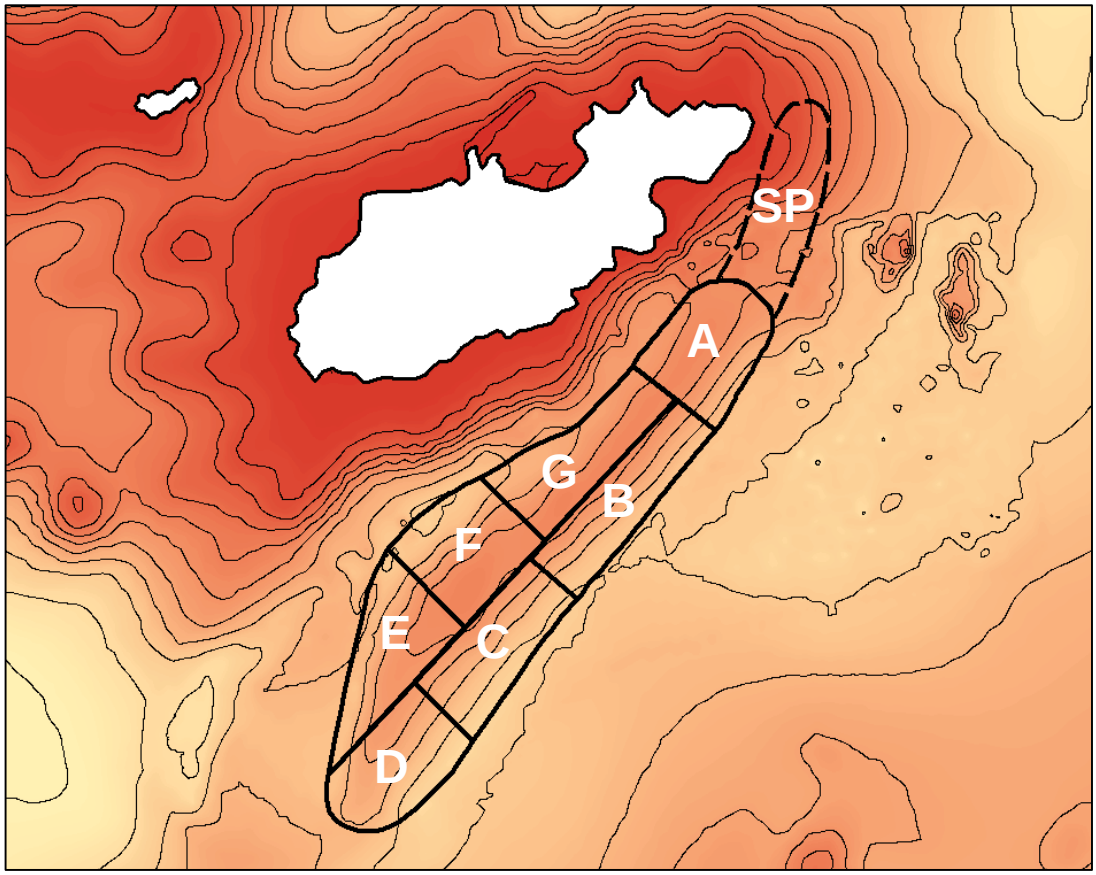

Figure 8.1 Division of the South Banks into seven Zones (A-G). An additional Zone (SP) represents a potential sediment supply pathway leading from the headland region of Alderney to Zone A. Model outputs are spatially averaged across each zone to condense the data and to help generalise about impacts.

Zones A-G are defined in a clockwise manner with Zone A covering the width of the South Banks at its North-Eastern end (Figure 8.1). Zones B-D encompass the ebb-dominant region (sandwaves migrate to SW) and Zones E-G the flood-dominant region (migration to NE). Sandwave asymmetry and observed migrations suggest that sand circulates around the North-Eastern tip of the sandbank in Zone A (Figure 5.1), transitioning from the flood-dominant to the ebb-dominant region. A similar process occurs in the opposite direction in Zone E with sand passing from the ebb-dominant to the flood-dominant region. The sandbank is at its greatest height in Zone F with maximum sandwave heights observed and a substantial crest volume. Potential extraction impacts upon sediment supply to the South Banks are considered using the additional Zone SP. This zone connects Zone A to the region immediately East of the Alderney headland via a curved pathway. The Zone SP limits are suggested by the defined mega-ripple field observed in the bathymetry (chapter 5) and the general morphology of the sandbank.

8.2 Scenario comparison table

Outputs from the sandbank zonation and data processing procedure described above are presented in Table 8.1. The three species of difference-data (residual current, sediment transport residual and evolution) are grouped together vertically with the difference values represented by colours (see the 'Zones key' to the right). Difference values across the eight zones are then *themselves* averaged to provide an average difference value for each of the three species of difference-data (i.e. 3 averaged difference values per scenario). These averages are also represented with colours and can be interpreted using the 'Average key' to the right of the 'Zones key'. In the case of the Bed-level evolution differences the 'Average' refers to the averaged *absolute value* in bed-level difference. This is because bed-level averages across the eight zones should roughly cancel out due to continuity of mass. Therefore evolution magnitudes, regardless of sign, are averaged to assess the scale of impacts upon both erosion and deposition combined.

The three averages for each scenario are normalised with respect to their maximum values (see statistics) and summed to produce a scenario total. These three normalised averages and the scenario total for each scenario are plotted together in Figure 8.2. These totals are then used to calculate an *Impact Ranking (IR)* for each scenario with *IR=1* denoting the highest impact scenario and *IR=17* the lowest impact scenario.

The final row of Table 8.1 relates to the sorting of the scenarios into 3 *Impact Categories, H*, *M* and *L*, indicating *High Impact*, *Medium Impact* and *Low Impact* extraction scenarios. These categories correspond to the *relative* impact of each scenario and are discussed further in the Conclusion (Chapter 9). The aim of categorisation here is to help provide a useable framework for guiding the process of tidal-energy exploitation within the Alderney Race. The scenarios were sorted into impact categories using their scenario totals with the range of possible values being split into three equal regions (i.e. High Impact Category scenarios have a scenario total between 2 and 3; see Figure 8.2).

The array footprints and the South Banks zones are superimposed upon the model bathymetry in Figure 8.3. The Impact Ranking for each of the 300MW array extraction scenarios are included in the graphic. When taken together, Table 8.1 and Figure 8.3 provide a visual summary of the study outputs.

Table 8.1: Impact comparison table for the 17 energy-extraction scenarios. See section 8.2 for details.

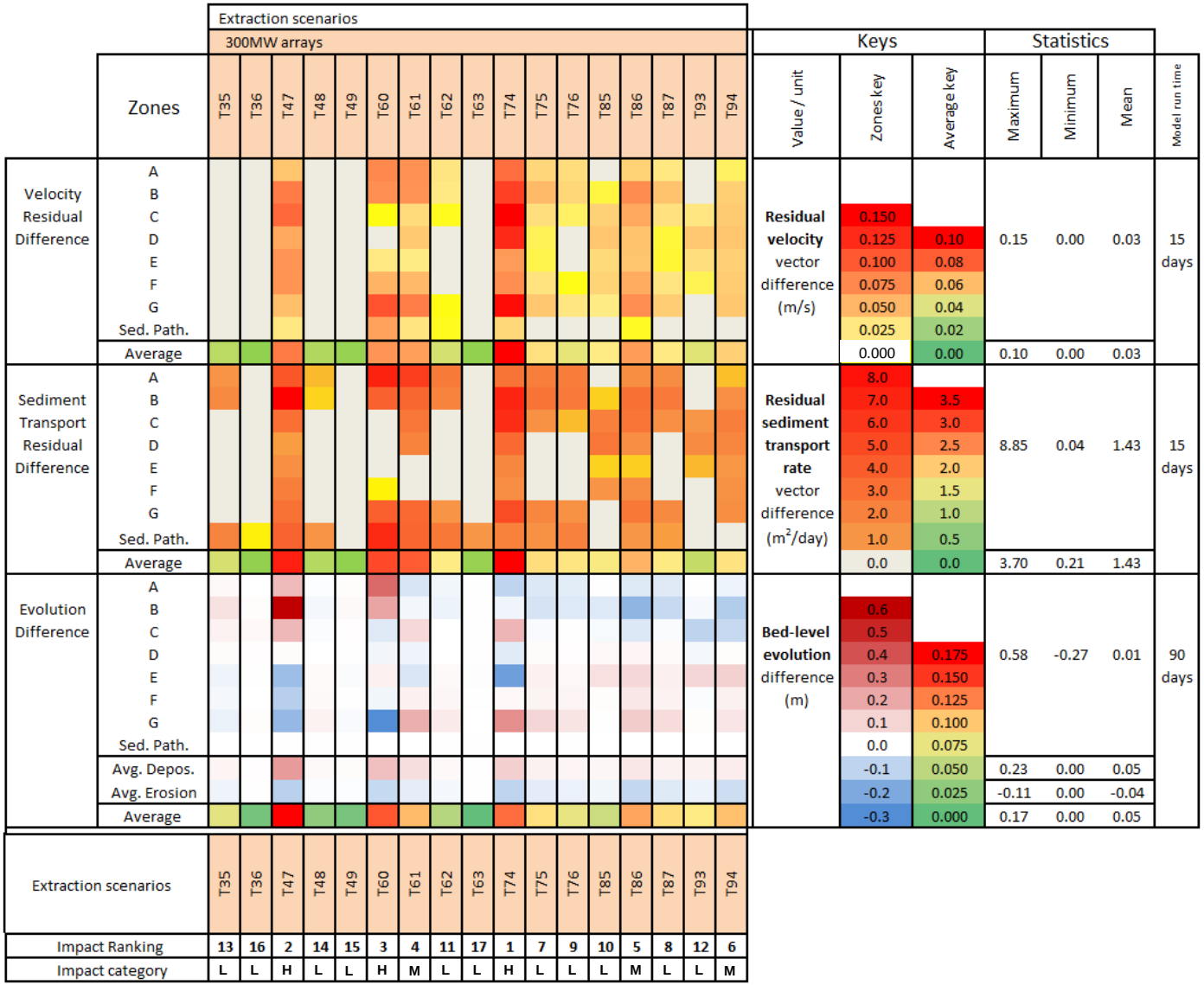

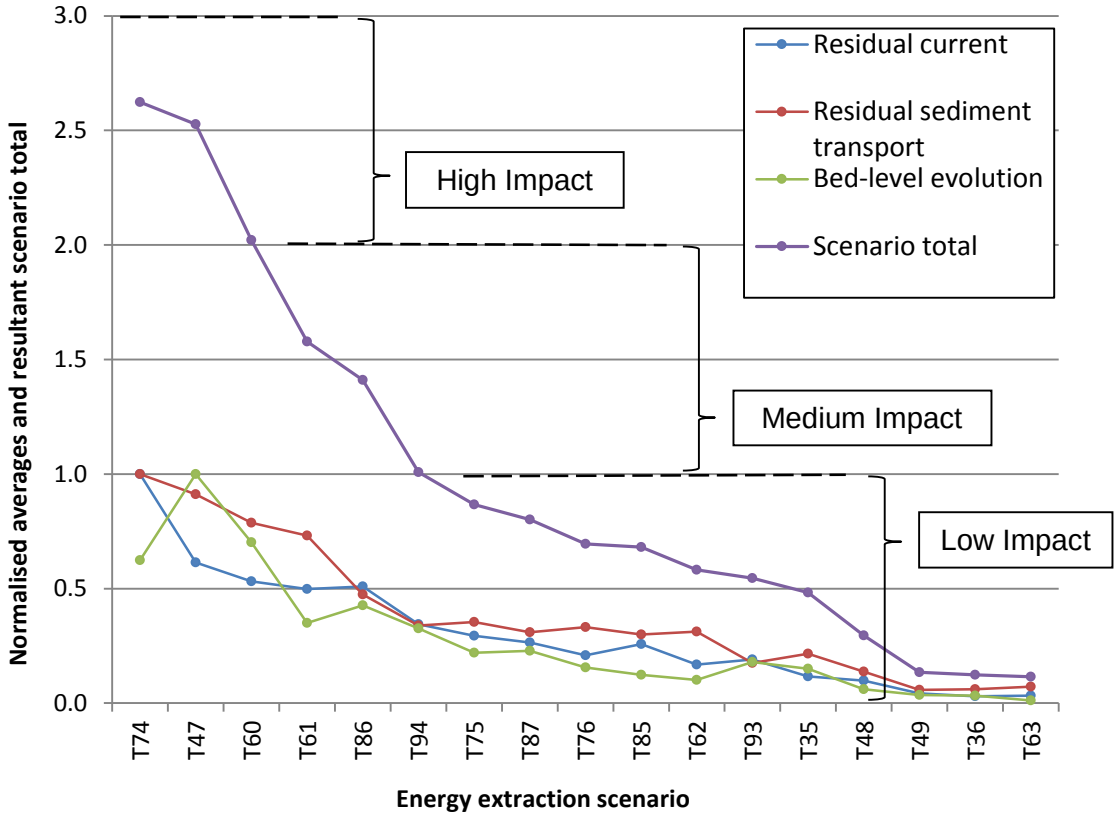

Figure 8.2 Scenario total for each of the 17 energy extraction scenarios. The scenarios are ordered along the x-axis from highest to lowest impact. The scenario total is the sum of the three different types of normalised average (residual current, residual sediment transport and bed-level evolution) for each of the 17 scenarios (i.e. maximum normalised average = 1 and maximum possible scenario total = 3). The region of scenario totals corresponding to High, Medium and Low Impact Categories are highlighted (see Table 8.1, Table 9.1 and section 9.3).

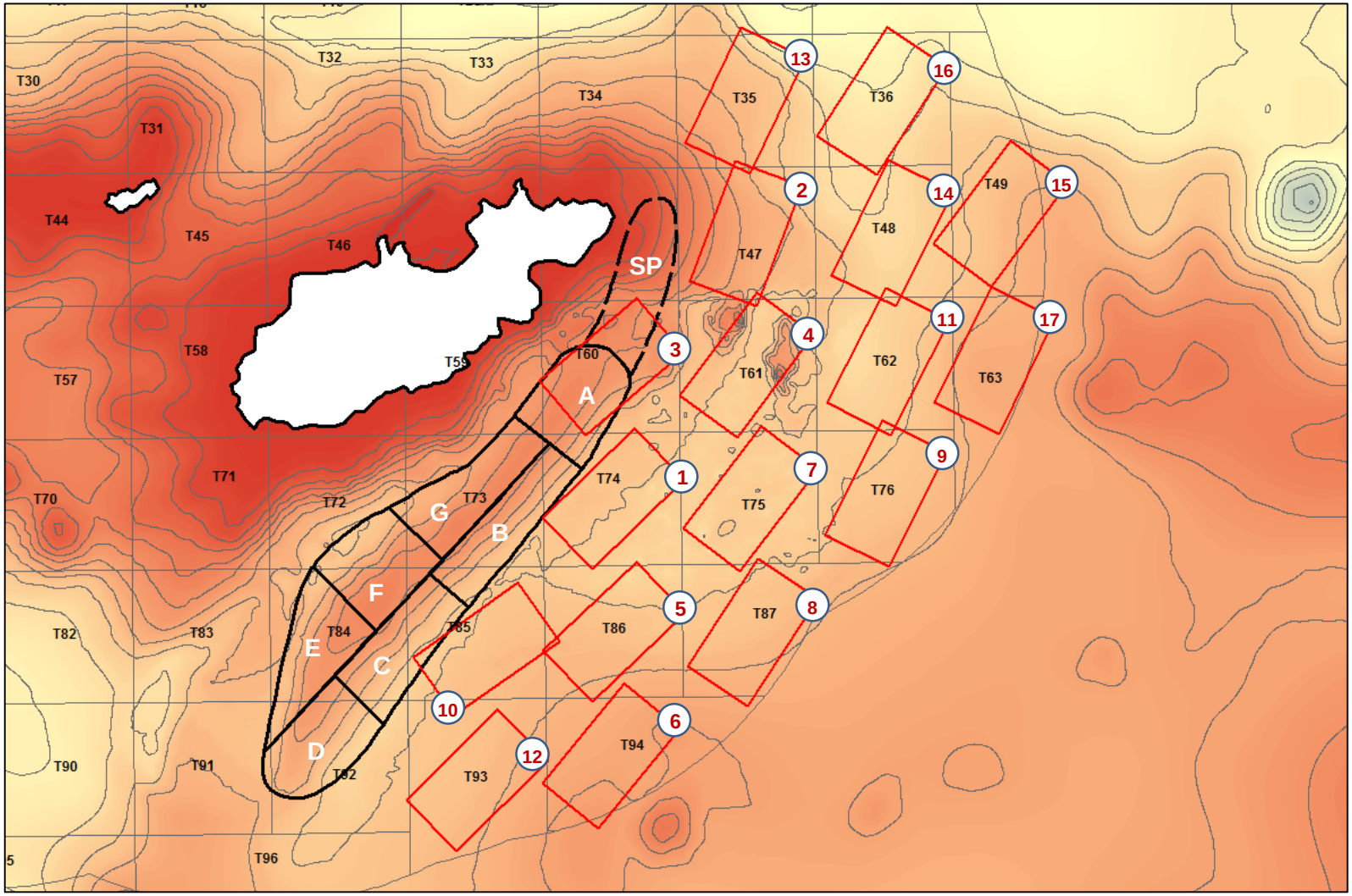

Figure 8.3 Array footprints for each development T-block (red lines, black lettering) and the South Banks Zone limits (black lines, white lettering). The Impact Ranking for each 300MW extraction scenario is included in the corner of the corresponding array footprint (Impact Ranking of 1 = largest impact).

8.3 Table interpretation and inter-scenario comparisons

8.3.1 General pattern of impacts

The impact of energy extraction appears to decrease with distance from the North-Eastern tip of the South Banks (Zone A). Arrays located in T-blocks T47, T60, T61 and T74 result in the largest modifications to the flow regime and, consequently, large alterations to sediment transport rates. This makes intuitive sense as these T-blocks experience the highest velocities on the Alderney side of the race as shown in Figure 7.11 (a). The propagating eddy shed from the headland is closely related to velocities in this region with energy-extraction decreasing the rotational velocity and life-time of the eddy (i.e. the eddy possesses less rotational momentum and dissipates sooner).

The arrays located the furthest East of the headland tip (T63, T49 and T36) have the smallest impact upon flows over the South Banks. Impacts along each of the four Northern T-Block rows can be seen to decrease with distance to the East (for T35-36: IR=13,16; for T47-T49: IR=2,14,15; for T60-T63: IR=3,4,11,17; for T74-T76: IR=1,7,9). This matches the variations in velocity deficit curvature observed downstream from arrays on the ebb-tide as seen in Figure 7.20.

8.3.2 Impacts causing modification to tidal eddy crossing the South Banks

Counter-intuitively, the pattern is not maintained for the bottom two T-block rows where arrays closest to the sandbank (T85 and T93) cause lower impacts than those immediately to the East (T86 and T94). Looking at the relevant impacts for the South Banks Zones in Table 8.1 it appears that the T86 scenario leads to larger changes to the flow in Zones A, B, G and SP. Observation of outputs reveals that this is caused by flow acceleration around the North of the T86 array on the ebb-tide resulting in larger velocities in the region between Zone F and Alderney (i.e. velocities are larger here than for both the baseline *and* the T85 model). The increase of these South-West-West velocities causes the tide to turn later in this region and appears to have a disproportionate impact upon the strength of the eddy shed from the tip of Alderney. The rotational velocity of the eddy is reduced and this has a consequent effect upon flows in Zones A, B, G and SP. The same mechanism is responsible for the increased

impact of T94 relative to T93. Ultimately, the larger accelerations resulting from extraction in T86 and T94 are due to the T-blocks being located in regions of higher ebb-tide velocity as discussed in section 7.3.

Figure 8.4 shows the path of the eddy-centre after it is induced at the North-Eastern tip of Alderney. It grows as it propagates 2km to the South-West whilst remaining 'attached' to the island. When the eddy centre reaches a position close to the North-Eastern end of the South Banks it detaches from the island and propagates first south and then increasingly towards the East. The eddy propagates, once detached, for approximately 3 hours before being dissipated by the increasingly strong and uniform flood-tide.

A number of the energy extraction scenarios significantly alter the directional propagation of the eddy in addition to the rotational velocity impacts discussed above (T86 and T94). Figure 8.5 plots simultaneous paths for eddy-centres relating to the baseline run (red line), the T74 300MW run (purple line) and the T60 300MW run (blue line). The paths relate to the same range of time-steps for each of the models and show how energy extraction can alter the eddy propagation in opposite ways. The eddy travels further to the East and covers less distance for the T74 run than for the baseline run. For the T60 run the opposite is the case with the eddy veering further south and covering a greater distance.

In the T74 scenario the array appears to significantly interfere with the rotation of the eddy, impeding the regions of the circulating flow orientated towards the South-West. Energy is taken out of the flow causing the eddy to weaken relative to the surrounding tidal flows. The eddy in the T60 scenario actually starts off weaker than the baseline case (further to the North-West) due to dissipation across the T60 array. Once the eddy begins to propagate away from Alderney however, flow acceleration around the South of the T60 array strengthens the eddy and provides an extra impetus pushing the eddy further to the West. The eddy covers more ground and is stronger throughout its propagation.

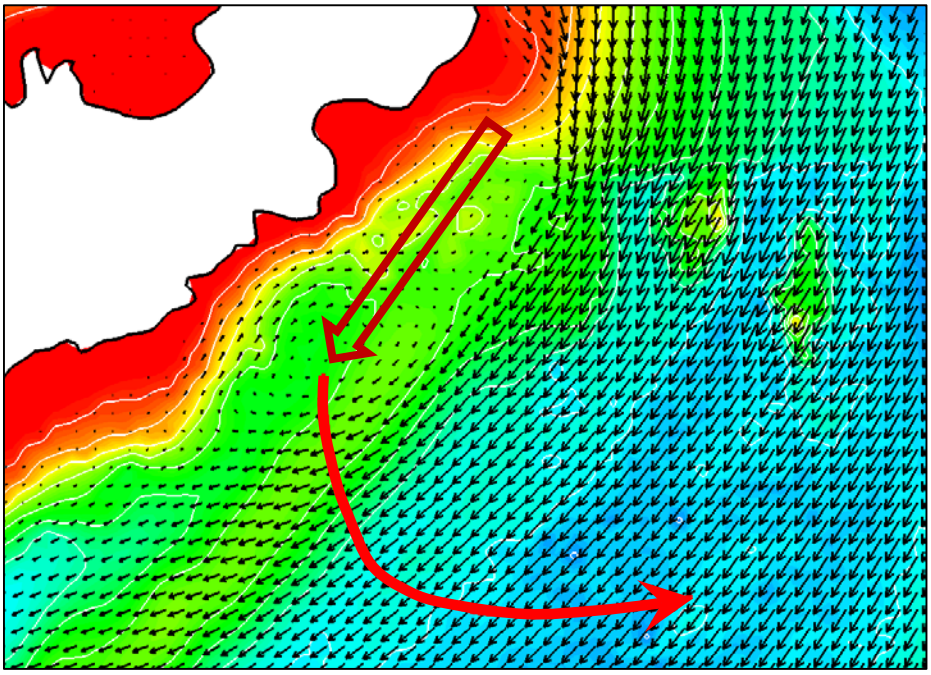

Figure 8.4 The path of the eddy formed close to the headland at the North-Eastern tip of Alderney. The eddy remains attached to the island for 2km, growing as it moves South-West before detaching from Alderney and propagating across the South Banks. It travels ~3.3km before dissipating into the strong North-Eastern flood-tide.

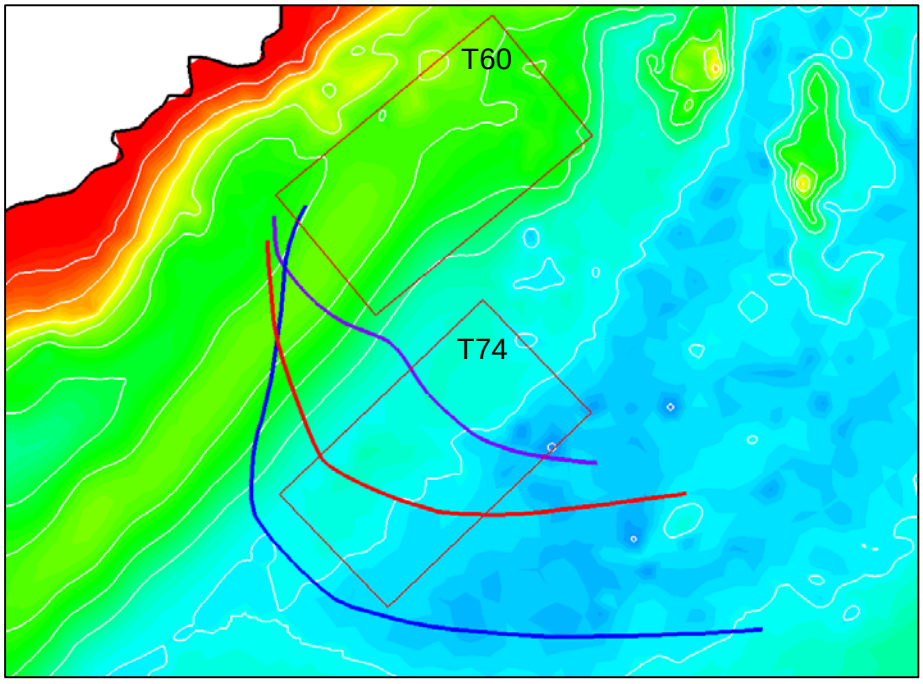

Figure 8.5 The path of the propagating eddy centre for the baseline (red line), T74 (purple line) and T60 (blue line) model runs. Array footprints included (1.0km by 1.8km). The lines start and finish on simultaneous time steps and cover a period of 3hrs 10mins.

The modification of eddy development due to energy-extraction represents a significant alteration to the flow regime surrounding the South Banks. Our difference-outputs for the residual sediment transport and for bed-level evolution show that the morphology of the South Banks would be altered as a result. Most of the extraction-scenarios do not change the *path* of the eddy as it propagates. The two scenarios which might also be expected to have an effect upon the eddy pathway (T35 and T47) don't have a noticeable effect upon the eddy development. The T61 scenario also changes the direction of propagation with the eddy following a path equidistant between the baseline and T74 equivalents.

8.3.3 Scenarios with relatively low impact

T35 and T36 have comparatively little effect on flows over the banks considering they are situated upstream on the ebb-tide. An analysis of the baseline outputs shows that velocities on the ebb-tide in these T-blocks are similar to the unbounded velocities 10km to the North-East. Flows start to accelerate around the headland downstream from these arrays and therefore their impact upon the downstream flow field is comparatively small.

8.3.4 Possible impacts to sediment transport pathway

All but 3 of the extraction scenarios result in sizeable impacts to sediment transport residuals along the suggested sediment pathway connecting the South Banks to the headland (Zone SP). For many of the scenarios velocities are *increased* for both the flood and ebb tides due to flow acceleration between the Northern part of Alderney and the array. This effect occurs even when the arrays are located far away from the zone (i.e. T87) with only T93, T94, T85 and T49 located far enough away to have little impact in this region. A lack of knowledge relating to bathymetry and sand movement close to the headland prevent us from speculating further as to the possible impacts of energy-extraction upon sandbank maintenance. Having said this, the high velocities that occur in this region and the apparent sensitivity to flow blockages located in the race suggest that sandbank maintenance could be modified by energy-extraction schemes.

9 Conclusions

9.1 Summary of numerical modelling work

The impacts of 17 energy-extraction scenarios within the Alderney Race have been investigated using a numerical modelling approach. The prime motivation has been to ascertain whether the installation of a tidal device array could significantly alter the tidal regime over the Alderney South Banks sandbank. The effects of changes in the flow field upon sandbank morphology and circulation of sand around the bank have also been explored using two different methods (sediment transport residuals and bed-level evolution outputs from a sedimentary model).

A wide variety of potential extraction schemes have been explored with arrays (300MW nominal rated power) simulated in 17 locations in the Western Race. It should be noted that the results presented apply to the particular configuration (total area, layout and number of turbines) of the array used in the model. It is possible that alternative configurations may result in more or less impact upon the flow and hence the South Banks.

The study outputs provide a useful and robust means for assessing the potential impacts of a wide variety of energy-extraction scenarios. Our hydrodynamic model has been validated relative to ADCP velocity data collected in the immediate vicinity of the sandbank. Real-world sand transport rates have been inferred from sand-wave migrations and agree favourably with sediment transport residuals calculated from our model outputs. Outputs from our sediment model reproduced realistic morphological behaviours over the bank although extremely high erosion rates were predicted by the model.

9.2 Impact rankings for energy extraction scenarios

The 17 extraction scenarios have each been assigned an *Impact Ranking (IR)* value with *IR=1* relating to the highest impact scenario. Rankings were determined by the equal consideration of three species of impact (quantified as *differences* between baseline and extraction model runs) listed in order of increasing complexity:

- **Residual current –** Variations in flow field over the sandbank were quantified and represent the most fundamental value for assessing impacts. It is the simplest measure to visualize, but least directly linked to sediment transport
- **Residual sediment transport –** The hydrodynamic outputs were converted to instantaneous sediment transport rates using sediment transport formulae. Averaged to produce residuals, these values interpret the model output velocities in terms of resultant sediment movement.
- **Bed-level evolution –** Evolutions of the seabed, simulated using a sediment transport model, convert variations in sediment transport rates to modifications in sand movement and, subsequently, changes to the bathymetry.

Arrays located close to the North-Eastern tip of the South Banks result in the highest impacts to the flow regime and, consequently, the largest impacts upon sandbank morphology. Development and lifetime of the large propagating eddy shed from the island is particularly sensitive to array installation in this area (Figure 8.5). Impacts decrease with distance from this region with arrays located the furthest East leading to the minimum variations over the banks (T63, T49 and T36). Arrays situated in these locations have a comparatively small effect on the banks during the ebb-tide due to their distance from the headland where the flow divides around Alderney. Crucially, these same arrays are also situated too far downstream from the sandbank (i.e. not adjacent to the South Banks) on the flood-tide and therefore have an almost negligible effect during this phase of the tide.

9.3 Impact categories

The 17 extraction scenarios have been further sorted into 3 Impact Categories, to provide a generalised framework for non-technical planners and policy makers and to help inform monitoring requirements post-installation. It should be emphasised that the labelling of these categories as high, medium and low impact indicates the *relative* impact of each extraction scenario within the context of the modelling outputs presented. Table 9.1 presents these three categories in which the impacts of energy extraction are broadly similar (also see Figure 8.2):

Table 9.1 17 energy extraction scenarios grouped into three impact categories relating to the broad effects of array installation.

Impact Category	**Array located in T-Block:**	**Description**
High Impact	T74, T60, T47	Significant impact on the eddy path and magnitude, large decelerations or accelerations occur directly over the South Banks
Medium Impact	T61, T86, T94	Some impact on the eddy path and magnitude across South Banks
Low Impact	T85, T87, T93, T62, T75, T76, T35, T48, T49, T36, T63	Impacts occur in some zones, flow differences occur over the banks but are not large. Impact upon eddy is relatively small and upon the flow in general is localized.

9.4 Coupled hydrodynamic sediment transport model

The coupled hydrodynamic sediment transport model has provided valuable insights into the short term effects of changes to flow patterns over the South Banks. The *rigid bed* method has been essential for realistic modelling in this region as discussed in section 6.3. However, the model did not accurately recreate the long-term equilibrium morphology of the South Banks (see section 7.5). This is not surprising given the typical accuracies of sediment-transport modelling in coastal environments due to limitations of the available sediment transport formulae; lack of sediment transport rate data with which to directly compare our sediment model; and the necessary limitations of the modelling approach (no wave model; 2D depth-averaged approach). For the results to be regarded as robust a sediment model must be able to demonstrate sandbank stability (i.e. equilibrium) over decadal time-scales before predictions of the future shape of the sandbank post-energy-extraction could be deemed reliable. Use of sediment modelling during this study has sought to

investigate the differential impact of energy-extraction upon bed-levels over a relatively short period as opposed to predicting the future development of the South Banks bathymetry over a long period of time.

9.5 Summary

The baseline morphological regime of the South Banks is extremely active, as demonstrated by the survey data and discussed in chapter 5. However in order for the South Banks to persist for as long as they have in such an active environment, a complex dynamic equilibrium must exist and a precautionary approach should be taken in regard to activities that might perturb the processes of sandbank maintenance. The validity of the research hypothesis proposed in section 1.2 is supported by the study outputs. The morphology of a large headland associated linear sandbank (the South Banks) does appear to be sensitive to the hydrodynamic impacts of large energy extraction schemes (see section 8.3). Significantly it is the particular sensitivity of the large, propagating eddy to hydrodynamic changes that translates to the wider morphological sensitivity of the sandbank.

The study outputs suggest that energy-extraction in the region of the South Banks could have a significant impact upon the sandbank morphology with the likely impacts varying widely with array location. The presence of such large sand-waves relative to the sandbank height implies that a large fraction of the sand in the sandbank is mobile over decadal timescales. Therefore, changes in the sandbank shape or footprint could definitely occur due to energy extraction.

Ultimately, questions relating to the consequences of a modified South Banks bathymetry or what might be considered acceptable limits of sandbank modification are beyond the scope of this study. Having said this we would urge particular caution when considering large energy-extraction proposals for the T74 development T-block. Large impacts upon the local sediment regime may also have unpredictable consequences for the energy yield at a particular point (i.e. the consideration of morphological impacts is not solely an environmental or coastal defence issue).

The study outputs can be considered within the context of the power density present in each development T-block as shown in Figure 7.12. On this basis, considering the model outputs, the best locations for maximising power output whilst minimising

impacts over the South Banks appears to be either T63 or T49. However in practice many other factors may significantly influence the choice of T-block, not least the cost of routing subsea power cables back to shore from the arrays.

9.6 Unique contribution of the research

The unique aspects of the research are as follows:

1. *Systematic approach to assessing effects of array location* – Such a comprehensive, localised investigation of 17 different spatial placements of an identical tidal array (see Figure 6.7) within a real-world scenario is unprecedented in the literature. Modelling studies that focus upon array impacts upon sediment movement and coastal morphology typically investigate a much smaller number of placement options (Neill et al., 2012) or investigate much larger-scale interactions between array affects and sediment movement (Robins et al., 2012). One novel element of this study is the application of a systematic, finely resolved grid approach to array placement within a high-resolution numerical model for the purposes of investigating morphological impacts.

2. *Analysis of impacts upon the propagating eddy* – The discussion and identification of the sometimes counterintuitive connection between array placement and the propagating eddy (see section 8.3.2) constitutes a novel aspect of the work. The systematic approach to array placement yielded insights into the way in which flow acceleration around an array occurring on one phase of the tidal cycle (i.e. the ebb) can significantly alter the dynamics of the following flood tide. In one scenario accelerations to the north of the T86 array delayed the turn of the tide (in the region between the South Banks and Alderney) thereby reducing the rotational velocity of the propagating eddy and impacting upon flow velocities over the South Banks.

3. *Sediment modelling utilising a hard bottom approach* – The application of a ‘hard bottom’ approach (see section 6.3) to sedimentary modelling of a headland associated linear sandbank is novel. As discussed in section 6.3, sedimentary models for regions with high tidal velocities and extensive areas of bedrock are liable to significantly overestimate sediment input. The use of

a ‘hard bottom’ to limit possible erosion depths within the model and represent a bedrock layer across the model domain deals with this problem of unrealistic sediment supply. The use of hard bottoms within coastal sediment models is rare due to the difficulty of obtaining accurate information relating to the bedrock layer. The availability of comprehensive, high-resolution bathymetry for the Alderney South Banks, the morphological interpretation of this data (chapter 5), and the subsequent spatial interpolation of bedrocks layers beneath sedimentary features (section 6.3) has enabled a hard bottom approach to be appropriately applied.

9.7 Further work

9.7.1 Expansion of the model to 3D

The use of a depth-averaged, 2D numerical modelling software program (TELEMAC-2D) lends itself well to coastal area modelling. Depth-averaged models have practical advantages in terms of how well a problem can be defined, they’re computationally in-expensive (compared to 3D models) and the outputs can be simply displayed and manipulated. The disadvantages of 2D models relate to their inability to simulate vertical variations in fluid velocity, their simplification of the bottom boundary layer and their inability to provide adequate inputs to coupled modules that would benefit from information regarding vertical velocity variations (e.g. sediment or wave modules).

The expansion of the existing model to 3D could be achieved using the TELEMAC-3D, multi-layered model. TELEMAC-2D and TELEMAC-3D use a similar approach and format therefore migration of the South Banks model would be possible. The use of a 3D model to simulate the hydrodynamic regime of the South Banks would be particularly advantageous for resolving secondary currents in the region of the sandbank (see section 3.1.4) and for providing inputs to the coupled sedimentary model (SISYPHE). Expansion of the model to 3D would require a new method for including the effects of energy extraction to be developed. The area-averaged array method developed by Blunden (2009) is not applicable to 3D models.

9.7.2 Inclusion of a wave model

The numerical model could be made more realistic by including the effect of waves using the TELEMAC module TOMAWAC. Wave action in the region of the South Banks is significant (see section 4.2) and is likely to contribute to the real world sediment transport rates. Existing wave data could be used to generate inputs for the model which would be coupled with TELEMAC-2D and the sedimentary model, SISYPHE. One alternative method would be to obtain wind data for the wider English Channel and to setup TOMAWAC to automatically generate the wave climate. Ideally both methods would be implemented and the resultant outputs used to corroborate the other approach and calibrate the simulated wave climate.

9.7.3 Improved sediment model

The sediment model could be setup to reflect the variation in sediment grain size across the South Banks as represented in Figure 5.2. Median grain sizes along the length of the bank vary from 0.98-2.39mm and are sorted with the largest sands occurring at the South-Western end of the sandbank. The pattern of sorting suggests that this variation may be an important spatial aspect when recreating the long-term sandbank equilibrium behaviour within the baseline model (see section 7.2).

Appendix A Sandbank Classification

A classification scheme based upon sandbank origin and development was proposed by Dyer and Huntley (1999) in an attempt to unify the diverging approaches to sandbank behaviour employed by marine geologists and physical oceanographers. An intuitive, generalised framework was presented which can be used to categorise real world sandbanks into a few basic archetypes based upon sandbank size, shape, location and local morphology. The various types and sub-types enable likely behaviours to be predicted and the potential effects of anthropogenic factors upon sandbank morphology/stability to be assessed.

Figure A1 shows the different types of sand bank and how they relate spatially to the coastline. The tidal stream directions are represented with arrows. The following descriptions of the various sandbank types are informed by Dyer and Huntley (1999) and HR Wallingford (2001).

Type 1 *– Open shelf linear sand banks*

Type 1 sandbanks can be up to 80km long, average 13km in width, tens of metres in height and come to within a few metres of the sea surface (Dyer and Huntley, 1999; HR Wallingford, 2001). They are usually located far from the coastline and orientated at small angles to the main tidal current. Type 1 banks are likely to be the final state towards which all banks will progress before they become inactive, independent of their origin, once coastal retreat has separated them from their source conditions (HR Wallingford, 2001).

Type 2 *– Estuary mouth*

Type 2 sandbanks occur in estuary mouths and naturally fall into 2 categories depending upon tidal range.

Type 2A sandbanks are found in the mouths of macro-tidal estuaries (tidal range > 4m) that are larger than 10km in width and are aligned with the flow.

Type 2B sandbanks are ebb tidal deltas, formed due to ebb dominance in narrower micro-tidal estuaries (tidal range < 2m) with mouths smaller than 10km in width. These are split into type 2Bi and 2Bii where:-

2Bi – The estuary mouth doesn't migrate resulting in a static sandbank

2Bii – The estuary mouth migrates either along-shore or/and across-shore (this is typical for barrier island inlets) leaving remnant banks at angles to the coast.

Type 3 *– Headland associated banks*

Type 3 sandbanks are formed at headlands where sediment transported by long-shore drift (from one or both sides of the headland) is swept offshore where it accumulates to form a long, linear sandbank. Tidal flows around the headland are a key factor in the formation of type 3 banks. Strong currents are required to move sediment far offshore (along the length of the bank) and to form large eddys in the lee of the headland that play an important role in helping form and maintain the sandbank.

Where a headland erodes very slowly and the sediment is supplied predominantly from one side, type 3A banks, or *banner banks*, may be formed. These extend, protruding from the headland, in a straight line and are typically 5-10km long and 1-2km wide (Berthot and Pattiraratchi, 2005). The formation and maintenance processes are well understood (compared to the other types of sandbank) allowing the semi-realistic modelling of 3A banks to take place. Banner banks appear to occur more frequently in regions where the water depth decreases rapidly away from the coast.

Where the headland is easily erodible, type 3B banks are formed. The mechanisms that form 3B banks are not well understood. It is thought that banks form alternately on opposite sides of the headland as the headland retreats due to variations in protection from wave attack (as the sandbank increases in size) and, consequently, reduced long-shore sand transport. As the headland and the related coastline retreat the sandbanks are left offshore, cut-off from their formative sediment supply where they are modified by the prevailing hydrodynamic environment (i.e. tidal flows and wave effects).

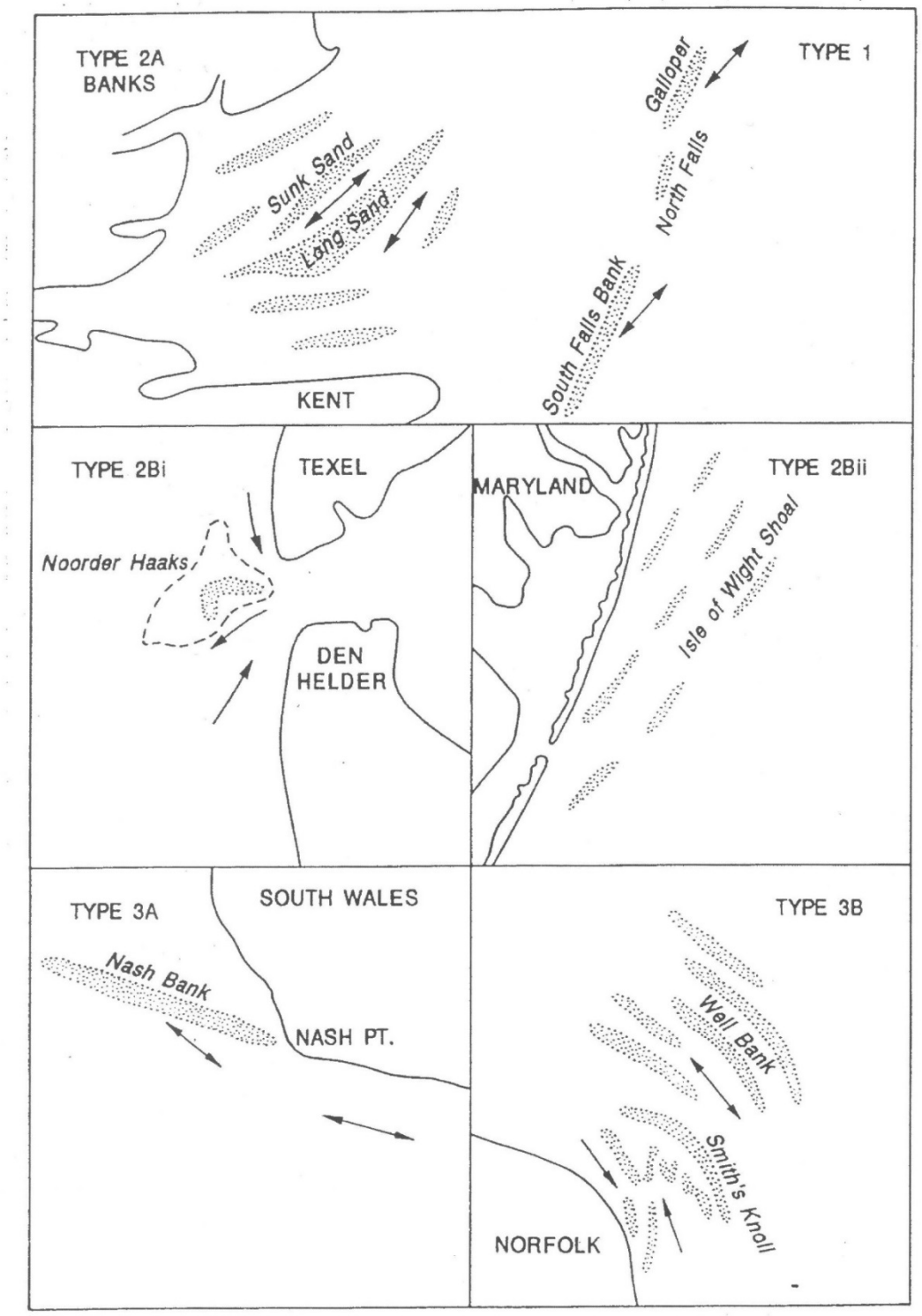

Figure A1 The different types of sand bank as described by Dyer and Huntley (1999). The tidal stream directions are shown with arrows (illustration from Dyer and Huntley, 1996).

Appendix B TELEMAC2D: Example Steering File

An example steering file used for running TELEMAC simulations upon the IRIDIS computing cluster is included below. TELEMAC options are specified using Keywords which are capitalised in the steering file. The simulation options used during the modelling phase are stated between forward slashes on the same line as each keyword. This steering file corresponds to the *baseline* hydrodynamic model run and lists the physical and numerical parameters used.

```
/ Model-run title
TITLE = 'Example_Steering_File'

/ File specification
GEOMETRY FILE = geo.slf                      /Model mesh input via the geometry file/
BOUNDARY CONDITIONS FILE = cli.txt    /Boundary nodes and boundary options specified/
RESULTS FILE = example.res                        /Binary results file/
FORTRAN FILE = princi.f                           /User-programmed subroutines/
PARALLEL PROCESSORS = 48             /Number of processors chosen for parallel runs/

/ Model time step and total run time
TIME STEP =75.                                              /Model time step/
NUMBER OF TIME STEPS = 18432  /Model run time specified as multiple of time step/

/ Model runs outputs
GRAPHIC PRINTOUT PERIOD = 8   /Regularity at which outputs are written to results file/
LISTING PRINTOUT PERIOD = 100                               /
NUMBER OF FIRST TIME STEP FOR GRAPHIC PRINTOUTS = 1152      /Model ‘spin-up’ period
VARIABLES FOR GRAPHIC PRINTOUTS = 'U,V'      /Output variables – U & V = velocity
components/
OUTPUT OF INITIAL CONDITIONS = NO      /Inclusion of initial model state in results
file/

/ Physical parameters
LAW OF BOTTOM FRICTION = 5                  /Nikuradse bottom friction/
FRICTION COEFFICIENT = 0.4                  /Default friction coefficient specified/
TURBULENCE MODEL = 1                        /Constant viscosity/
CORIOLIS = YES                              /Coriolis acceleration included/

/ Initial conditions
INITIAL CONDITIONS = 'CONSTANT ELEVATION'    /Initial free surface level at each mesh
node/
INITIAL ELEVATION = 0                                       /metres/

/ Boundary conditions
OPTION FOR LIQUID BOUNDARIES = 2     /Thompson boundary method used for liquid
boundaries/
TIDAL FLATS = YES                   /Element wetting and drying enabled/
```

```
/ Energy extraction
VERTICAL STRUCTURES = NO      /Calls DRAGFO subroutine to simulate energy extraction.
                              Keyword is changed to = YES for energy extraction runs/

/ Numerical parameters
TREATMENT OF THE LINEAR SYSTEM = 2    /Wave   equation   treatment   of   Saint-Venant
equations/
SPHERICAL COORDINATES = YES   /Variation  of  Coriolis  acceleration  with  latitude
enabled/
TYPE OF ADVECTION = 1;5       /Method of Characteristics used for velocity components
and PSI distributive scheme used for water depth (H)/
SUPG OPTION = 1;1                     /Classic SUPG method used for upwinding/
SOLVER = 1                    /Conjugate gradient method used for the propagation step/
SOLVER ACCURACY = 1.E-3       /Level of accuracy required for the propagation step/
DISCRETIZATIONS IN SPACE = 12; 11     /quasi-bubble for velocity and linear depth/
PRECONDITIONING = 2                                        /Diagonal
preconditioning/
INITIAL GUESS FOR H = 1       /Final value of depth (H) from previous time step used/
INITIAL GUESS FOR U = 2        /Extrapolated value of velocity from previous time step
used/
IMPLICITATION FOR DEPTH = 0.55        / Default values used for Depth and velocity/
IMPLICITATION FOR VELOCITY = 0.55             / 1 is fully explicit
MASS-LUMPING ON H = 1.                /Mass-lumping  option  specified  to  accelerate
                                      computation and improve stability/

&FIN
```

References

Ackers, P. and White, W.R., 1973. *Sediment transport: new approach and analysis*. Journal of the Hydraulics Division, ASCE, vol. 99, no. HY 11, proceeding paper 10167. 2041-2060.

Alonso, C.V., 1980. *Selecting formula to estimate sediment transport capacity in nonvegetated channels*. CREAMS, ed. Knisel, W.G., US Department of Agriculture, conservation research report no. 26, chapter 5, 426-439.

Alonso, C.V., Neibling, W.H. and Foster, G.R., 1982. *Estimating sediment transport capacity in watershed modelling*. Transactions of the ASAE, vol. 24, 5, 1211-1226.

Amoudry, L., 2008. *A review on coastal sediment transport modelling.* Proudman Oceanographic Laboratory, Internal document, 189. Available at: http://nora.nerc.ac.uk/8360/1/POL_ID_189.pdf.

Anderson, J.D., 1995. *Computational fluid dynamics: the basics with applications.* McGraw-Hill International Editions, chapter 3.

ASCE, 1982. *Relationships between morphology of small streams and sediment yields.* Journal of the Hydraulics Division, ASCE, vol. 108, no. HY 11, Proceeding paper 17450, 1328-1365.

Bagnold, R. A., 1963. *Mechanics of marine sedimentation.* The Sea: Ideas and Observations, 3, 507-528.

Bagnold, R.A., 1966. *An approach to the sediment transport problem from general physics*. US Geological Survey professional paper 422-J.

Bastos, A.C., Kenyon, N.H. and Collins, M., 2002. *Sedimentary processes, bedforms and facies, associated with a coastal headland: Portland Bill, southern UK.* Marine Geology, 187, 235-258.

Bastos, A.C., Collins, M. and Kenyon, N.H., 2003. *Water and sediment movement around a coastal headland: Portland Bill, southern UK.* Ocean Dynamics, 53, 309-321.

Bastos, A.C., Paphitis, D., Collins, M.B., 2004. *Short-term dynamics and maintenance processes of headland-associated sandbanks: Shambles Bank, English Channel, UK*. Estuarine, Coastal and Shelf Science, 59, 33–47.

Berthot, A. and Pattiaratchi, C., 2005. *Maintenance of headland-associated linear sandbanks: modelling the secondary flows and sediment transport.* Ocean Dynamics, 55, 526-540.

Bishop, A.A., Simons, D.B. and Richardson, E.V., 1965. *Total bed-material transport.* Journal of the Hydraulics Division, ASCE, vol. 91, no. HY 2, 175-191.

Blunden. L.S., Batten, W.M.J. and Bahaj, A.S., 2008. *Comparing energy yields from fixed and yawing horizontal axis marine current turbines in the English channel.* Proceedings 27th Conference on Offshore Mechanics and Arctic Engineering (OMAE 2008), Estoril, Portugal.

Blunden, L. S., 2009. *New approaches to tidal stream energy analysis at sites in the English Channel.* Thesis, Faculty of Engineering, Science and Mathematics, University of Southampton, UK.

Cengal, Y. A. and Cimbala, J. M., 2006. *Fluid mechanics: fundamentals and applications.* McGraw-Hill Higher Education, Chapters 5 and 15.

Charlier, R. H., 1997. *Re-invention or aggorniamento? Tidal power at 30 years.* Renewable and Sustainable Energy Review, 4, 271-289.

Colby, B.R., 1964. *Practical computations of bed-material discharge*. Journal of the Hydraulics Division, ASCE, vol. 90, no. HY2.

Crespo, A., Hernandez, J. and Frandsen, S., 1999. *Survey of modelling methods for wind turbines wakes and wind farms.* Wind Energy, 2, 1-24.

Davidson, P. A., 2004. *Turbulence: an introduction for scientists and engineers*. Oxford University Press, Chapter 2.

Davies, A.G., 1985. *Field observations of the threshold of sediment motion by wave action.* Sedimentology, 32, 685-704.

Dingler, J.R., 1975. *Wave-formed ripples in nearshore sands*. Thesis, Department of Oceanography, University of California, San Diego, USA.

Dyer, K.R., 1986. *Coastal and estuarine sediment dynamics.* Wiley, Chichester, 342.

Dyer, K.R. and Huntley, D.A., 1996. *Sand banks: origin, classification and modelling implications.* Report produced by Institute of Marine Studies, University of Plymouth for MAFF contract CSA3051. March 1996.

Dyer, K.R. and Huntley, D.A., 1999. *The origin, classification and modelling of sand banks and ridges.* Continental Shelf Research, 19, 1285-1330.

Einstein, H.A., 1950. *The bed-load function for sediment transportation in open channel flows*. Technical Bulletin 1026, US Dept. Agriculture.

Engelund, F., 1974. *Flow and Bed Topography in Channel Bends.* Journal of the Hydraulics Division, Vol. 100, No. 11, November 1974, pp. 1631-1648.

Engelund, F. and Hansen, E., 1972. *A monograph on sediment transport in alluvial streams*. 3rd ed. Technical Press, Copenhagen.

Frandsen, S., 1992. *On the wind speed reduction in the center of large clusters of wind trubines.* Journal of Wind Engineering and Industrial Aerodynamics, 39, 251-265.

Frandsen, S., Barthekmie, R., Pryor, S., Rathmann, O., Larsen, L., Hojstrup, J. and Thogersen, 2006. *Analytical modelling of wind speed deficit in large offshore wind farms.* Wind Energy, 9, 39-53.

Graebel, W., 2001. *Engineering Fluid Mechanics*. Taylor & Francis, chapter 8.

Great Britain. *Climate Change Act 2008. [Online].* Available at: http://www.legislation.gov.uk/ukpga/2008/27

Guy, H.P., Simons, D.B. and Richardson, E.V., 1966. *Summary of alluvial channel data from flume experiments*, *1956-1961*. US Geological Survey professional paper 462.

Hager, W.H., 2005. *Du Boys and sediment transport*. Journal of Hydraulic Research, 43(3), 227-233.

Heathersahw, H.D., 1981. *Comparisons of measured and predicted sediment transport rates in tidal currents.* Marine Geology, 42, 75-104

Hervout, J., 2007*. Hydrodynamics of free surface flows: modelling with the finite element method*. John Wiley & Sons Ltd., chapter 2.

Howarth, M. J. (1990). *Atlas of tidal elevations and currents around the British Isles*. Department of Energy, Offshore Technology Report, OTH 89 293, 16pp., appendix & charts.

HR Wallingford report, 2001. *Understanding the behaviour and engineering significance of offshore and coastal sand banks*. SR 512. HR Wallingford Ltd., Oxon.

IPCC, 2013: Summary for Policymakers. In: *Climate Change 2013: The Physical Science Basis. Contribution of Working Group I to the Fifth Assessment Report of the Intergovernmental Panel on Climate Change* [Stocker, T.F., D. Qin, G.-K. Plattner, M. Tignor, S. K. Allen, J. Boschung, A. Nauels, Y. Xia, V. Bex and P.M. Midgley (eds.)]. Cambridge University Press, Cambridge, United Kingdom and New York, NY, USA.

Kachel, N.B. and Sternberg, R.W., 1971. *Transport of bedload as ripples during an ebb current*. Marine Geology, 19. 229-244.

Katic, I., Højstrup, J. and Jensen, N. O., 1987. *A simple model for cluster efficiency*. European Wind Energy Association 1986 conference proceedings, 1, 407-410.

Knaapen, M.A.F., 2005. *Sandwave migration predictor based on shape information.* Journal of Geophysical Research, 110, F4, 1-9.

Langhorne, D.N., 1982. *A study of dynamics of a marine sandwave*. Sedimentology, 29, p. 571-594.

Laursen, E.M., 1958. *The total sediment load of streams*. Journal of the hydraulics division, ASCE, vol. 84, no. HY1.

Leopold, L.B. and Maddock, Jr., 1953. *The hydraulic geometry of stream channels and some physiographic implications.* US Geological Survey professional paper 252.

Lissman, P. B. S. and Radkey, R. L., 1979. *Coriolis Program: a review of the status of the ocean turbine energy system.* Oceans '79, 559-565.

Mahera, C. W. and Narsis, A. M., 2013. *Modelling of sediment transport in shallow waters by stochastic and partial differential equations.* Chapter 12 from *Sediment transport processes and their modelling applications* edited by Manning, A. J., InTeOpP.

Massey, B., 1084. *Mechanics of Fluids*. Taylor & Francis, chapter 7.

Meyer-Peter, E. and Müller, R., 1948. *Formulas for bed-load transport.* Proceedings 2nd Meeting of the International Association for Hydraulic and Structural Research, 39-64.

Middleton, G.V. and Southard, J.B., 1984. *Mechanics of sediment movement: Society of Economic Paleontologists and Mineralogists.* Short course 3.

Neill, S.P., 2008. *The role of Coriolis in sandbank formation due to a headland/island system.* Estuarine, Coastal and Shelf Science, 79, 419-428.

Neill, S.P., Litt, E.J., Couch, S.J. and Davies, A.G., 2009. *The impact of tidal stream turbines on large-scale sediment dynamics*. Renewable Energy 34, 2803-2812.

Neill, S.P., Jordan, J.R. and Couch, S.J., 2012. *Impact of tidal energy converter (TEC) arrays on the dynamics of headland sand banks.* Renewable Energy 37, 387-397.

Németh, A.A., Hulscher, S.J.M.H. and de Vriend, H.J., 2002. *Modelling sand wave migration in shallow shelf seas*. Department of Civil Engineering, University of Twente, The Netherlands.

OTPS. OSU Tidal Prediction Software.
http://volkov.oce.orst.edu/tides/otps.html, 2011.

Pingree, R.D., 1978. *The formation of the Shambles and other banks by tidal stirring of the seas.* Journal of the Marine Biological Association of the United Kingdom, 58, 211-226.

Robins, P.E., Neill, S.P. and Davies, A.G., 2012. *The impact of tidal energy extraction on the morphodynamics of the Irish Sea.* 4th International Conference on Ocean Energy proceedings, 17 October, Dublin.

Rottner, J., 1959. *A formula for bed material transport*. La Houille Blanche, no. 4.

Sakakiyama, T., Shimizu, T., Kajima, R., Saito, S. and Maruyama, K., 1985. *Sand ripples generated by prototype waves in a large wave flume*. Coastal Engineering in Japan, Vol. 28.

Schoklitsch, A., 1914. *Über schleppkraft und geschiebebewegung*. Engelmann, Leipzig.

Shaw, J., Duffy, G., Taylor, R.B., Chassé, J. and Frobel, D., 2008. *Role of a submarine bank in the long-term evolution of the northeast coast of Prince Edward Island, Canada.* Geological Survey of Canada Atlantic, Bedford Institute of Oceanography, Nova Scotia, Canada.

Shen, H.W. and Hung, C.S., 1972. *An engineering approach to total bed-material load by regression analysis*. Proceedings of the sedimentation symposium, chap. 14, 14.1-7.

Shields, A., 1936. Anwendung der aehnlichkeits-mechanik und der turbulenzforschung auf die geschiebebewegung. Preussische Versuchsanstalt fur Wasserbau und Schiffbau, 26, Berlin.

Signell, R.P. and Harris, C.K., 2000. *Modelling sand bank formation around tidal headlands*. Estuarine and Coastal Modelling, 6th Int. Conf., ASCE, New Orleans, LA, November 3-5, 1999. Editors: Malcolm L. Spaulding and Alan F. Blumberg.

Signell, R.P. and Geyer, W.R., 1991. *Transient eddy formation around headlands.* Journal of Geophysical Research, 96, 2561-2575.

Sleath, J.F.A., 1984. *Sea Bed Mechanics*. Wiley, New York.

Smith, J. D. and McLean, S. R., 1977. *Spatially averaged flow over a wavy surface*. Journal of Geophysical Research, 82, 1735-1746.

Soulsby, R.L., 1997. *Dynamics of marine sands*. HR Wallingford, Thomas Telford Publications, Chapters 1 and 7.

Squatriti, P., 2003. *Working with water in medieval europe: technology and resource-use.* Environment and History, 9, 110-112.

Sutherland, G., Foreman, M. and Garrett, C., 2007. *Tidal current energy assessment for Johnstone Strait, Vancouver Island.* Proceedings of the Institution of Mechanical Engineers, Part A: Journal of Power and Energy, 221, 147-157.

TELEMAC-2D User Manual. Version 6.0.
www.opentelemac.org/

Thompson, K.W., 1987. *Time Dependent Boundary Conditions for Hyperbolic Systems*. Journal of Computational Physics, 68, 1-24.

Thompson, K.W., 1990. *Time Dependent Boundary Conditions for Hyperbolic Systems, II*. Journal of Computational Physics, 89, 439-461.

Toffaleti, F.B., 1968. *A procedure for computation of the total river sand discharge and detailed distribution, bed to surface.* Technical report no. 5, Committee on channel stabilization, US Army Corps of Engineers Waterways Experiment Station, Vicksburg, Mississippi.

Van Rijn, L. C., 1984. *Sediment transport.* Journal of Hydraulic Engineering, 110, 1613-1641.

Van Rijn, L.C., 1993. *Principles of sediment transport in rivers, estuaries and coastal seas.* Aqua publications. The Netherlands, Chapter 5.

Versteeg, H. K. and Malalasekera, W., 1995. *An introduction to computational fluid dynamics: the finite volume method.* Longman Scientific and Technical, Chapter 2.

Voogt, L., Van Rijn, L.C. and Van Den Berg, J.H., 1991. *Sediment transport of fine sands at high velocities*. Journal of Hydraulic Engineering, 117(7), 869-890.

White. W. R., Milli, H., and Crabbe, A. D., 1975. *Sediment transport theories: a review.* Proceedings of Institute of Civil Engineers. 59 (2): 265-292.

White, W.R., Paris, E., and Bettess, R., 1980. *The frictional characteristics of alluvial streams: a new approach*. Proceedings of Institute Civil Engineers, part 2, 69. 737-50.

Wolanski, E., Imberger, J. and Heron, M., 1984. *Island wakes in coastal waters*. Journal of Geophysical Research, 89, 10553-10569.

Yalin, M.S., 1963. *An expression for bed load transportation*. Journal of Hydraulics Division, ASCE, vol. 89, no. HY3, 221-250.

Yalin, M.S., 1972. Mechanics of sediment transport. Pergamon Press, Oxford.

Yang, C.T., 1972. Unit stream power and sediment transport. Journal of the Hydraulics Division, ASCE, vol. 18, no. HY10, Proceeding paper 9295, 1805-1826.

Yang, C.T., 1973. *Incipient motion and sediment transport*. Journal of Hydraulics Division, ASCE, vol. 99, no. HY10, proceeding paper 10067, 1679-1704.

Yang, C.T., 1996. *Sediment transport: theory and practice.* McGraw-Hill, chapters 6-7.

Yang, C.T. and Molinas, A., 1982. *Sediment transport and unit stream power function*. Journal of the Hydraulics Division, ASCE, volume 108, no. HY6, Proceeding Paper 12 161, 776-793.

Yang, C.T. and Wan, S., 1991. *Comparisons of selected bed-material load formulas*. Journal of Hydraulic Engineering, 117 (8), 973-989.